3rd Generation Solar Cells for Green H_2 Production by Water Splitting

Inácio Durval Pinho
Master in Engineering Physics
Department of Physics and Astronomy
Faculty of Sciences of the University of Porto and Faculty of Engineering of the University of Porto
2025

3rd Generation Solar Cells for Green H_2 Production by Water Splitting

Inácio Durval Pinho

Dissertation carried out as part of the Master
in Engineering Physics

Department of Physics and Astronomy

2025

Supervisor
Dra. Arlete Apolinário, Assistant Researcher, Faculty of Sciences of the University of Porto

Co-supervisor
Dr. João Pedro Araújo, Associate Professor, Faculty of Sciences of the University of Porto



IFIMUP
Institute of Physics for Advanced Materials, Nanotechnology and Photonics
University of Porto

Institutions involved















Funding

This master thesis was supported by Fundação para a Ciência e a Tecnologia through the H2FlexiPEC project (ref. 2022.07332.PTDC), with DOI https://doi.org/10.54499/2022.07332.PTDC.

Additionally, acknowledgment is given to Fundação para a Ciência e Tecnologia and the Strategic Funding contract of the Institute of Physics for Advanced Materials, Nanotechnology and Photonics (IFIMUP), IFIMUP, UIDB/04968/2025 e UIDP/04968/2025, and the Laboratory of Physics for Materials and Emergent Technologies (LapMET), contract LA/P/0095/2020.

Arlete Apolinário acknowledges FCT – Fundação para a Ciência e a Tecnologia, under contract DL57/2016 (Ref. DL57/2016/CP1454/CT0017), with DOI https://doi.org/10.54499/DL57/2016/CP1454/CT0017, the H2FlexiPEC project (ref. 2022.07332.PTDC), with DOI https://doi.org/10.54499/2022.07332.PTDC,and the Laboratory of Physics for Materials and Emergent Technologies (LapMET), contract LA/P/0095/2020.





Dedicated to my family and Ni.

Acknowledgements

Gostaria de oferecer a minha profunda gratidão a toda a gente que de alguma forma me auxiliou no desenvolvimento deste trabalho.

Gostaria de deixar o meu profundo agradecimento à Dr. Arlete Apolinário pela sua paciência, tempo dedicado, pela orientação ao longo deste trabalho e pelas oportunidades para eu divulgar o meu trabalho. De igual forma, gostaria de deixar o meu agradecimento à Sofia Gonçalves pela sua orientação e colaboração em ambiente de laboratório, bem como à Sofia Caspani pela ajuda prestada em laboratório.

A todos os que passaram pela minha vida académica o longo destes anos, o meu obrigado.

Mas acima de tudo, o meu agradecimento à minha família e à Ni, sem os quais certamente nada disto seria possível.

Resumo

No atual panorama energético global, o crescimento de consumo energético continua a ser maioritariamente satisfeito por setores energéticos emissores de gases com efeito de estufa, contribuindo para o aumento da temperatura global. No presente ano de 2025, o aumento médio da temperatura global em relação à era pré-industrial já atingiu o limite de segurança estabelecido de 1,5 ºC. Neste momento crítico para a humanidade e para o planeta Terra, torna-se imperativa uma transição em larga escala para uma economia energética mais sustentável e ambientalmente responsável.

O hidrogénio verde surge como uma das soluções mais promissoras para esta crise energética, sendo um vetor energético limpo, neutro em CO_2 e abundante. As células foto eletroquímicas (PEC) aproveitam materiais semicondutores e um contra elétrodo metálico para converter diretamente a luz solar em energia química (sob a forma de H_2), através da eletrólise da água. Apesar de ser uma das tecnologias mais promissoras para a produção de hidrogénio verde, estes dispositivos enfrentam limitações impostas pelo hiato de energia dos semiconductores utilizado que restringem a absorção de luz e por sobretensões de ativação que geralmente resultam na necessidade de aplicação de uma polarização externa, comprometendo assim a eficiência destes dispositivos.

Em resposta a estas limitações, as células tandem PEC surgem como uma estratégia para ampliar a absorção luminosa e eliminar a necessidade de aplicação de uma fonte de tensão externa. Com o objetivo de identificar combinações de materiais adequadas para células tandem PEC, com base nos seus hiatos de energia, foram realizadas simulações numéricas utilizando uma versão adaptada do limite de Shockley–Queisser (S-Q), onde conseguimos implementar perdas na foto conversão através de fatores abstratos, rastreáveis a comportamentos físicos reais.

Os resultados das simulações permitiram identificar o óxido cúprico (CuO) como um material extremamente interessante para dispositivos tandem PEC, com eficiências teóricas máximas de conversão solar-para-hidrogénio de 16,7% quando emparelhado com a hematite e de 21% quando emparelhado com silício, em condições próximas das ideais e baseado nos hiatos de energia destes materiais. O modelo implementado foi também utilizado para avaliar uma configuração inédita de um dispositivo tandem com três materiais semicondutores. A configuração deste dispositivo permitiu transformar a geometria de emparelhamento ideal de hiatos de energia que maximizam a conversão

solar-para-hidrogénio de um ponto único (emparelhamento binário) para uma linha contínua (múltiplas combinações de hiatos). Adicionalmente, esta nova configuração permite aumentar as eficiências teóricas dadas pelo S-Q limit de materiais com hiatos de energia mais largos como WO_3 e TiO_2, para valores superiores a 18%, com uma taxa de produção de hidrogénio acima de 40% em relação à constante solar incidente (100 $mWcm^{-2}$). Motivados pelos resultados das simulações numéricas, foi introduzida pela primeira vez no instituto IFIMUP a investigação de foto cátodos de CuO, com o objetivo final de incorporar o CuO e a hematite num dispositivo tandem PEC.

Foram desenvolvidos dois protocolos para a síntese de CuO, que obtiveram resultados promissores tanto em estabilidade como em eficiência. O primeiro método de fabrico consiste na eletrodeposição de Cu, seguida de annealing térmico para conversão em CuO. Neste método, conseguimos melhorar significativamente a integridade estrutural (avaliada por espectroscopia Raman) dos fotocátodos, através da otimização das condições de eletrodeposição, não sendo detetada qualquer fase rastreável de Cu_2O após a caracterização foto-eletroquímica. Adicionalmente, o fotocátodo com melhor desempenho atingiu uma densidade de foto corrente de 1,44 $mA \cdot cm^{-2}$ a 0,5 V vs RHE, para espessura de filme e condições de deposição otimizadas, representando um aumento de ~85% na densidade de foto-corrente gerada em relação às condições de deposição não otimizadas.

Subsequentemente, foi implementado um segundo método que permitiu a eletrodeposição direta de CuO por variação do pH, utilizando os mesmos reagentes do eletrólito de eletrodeposição de cobre, usados no primeiro método. Neste caso, a agitação induziu uma microestrutura altamente porosa com uma morfologia semelhante a corais. Foi obtida uma densidade de foto corrente de 0,65 $mA \cdot cm^{-2}$ a 0,5 V vs RHE. Estes fotocátodos apresentaram uma integridade estrutural superior após caracterização foto eletroquímica, sem sinais de corrosão na estrutura micro-coral.

Com o método otimizado (primeiro método), foram fabricadas duas heterojunções de hematite–CuO. A heterojunção com melhor desempenho (FTO–CuO–α-Fe_2O_3: J_{photo} = 0,47 $mA \cdot cm^{-2}$ a 1,23 V vs RHE) apresentou um aumento de ~330% na densidade de foto corrente em relação à hematite isolada (FTO–α-Fe_2O_3: J_{photo} = 0,14 $mA \cdot cm^{-2}$), com uma redução adicional de ~115 mV vs RHE na tensão de iniciação da reação.

Palavras-chave: [Hidrogénio verde, Clivagem fotoeletroquímica da água, Células foto eletroquímicas tandem, CuO-Hematite, focátodos de CuO, foto conversão]

Abstract

In the current global energy landscape, the majority of global energy demand growth is still satisfied by greenhouse gas emitting energy sectors, further contributing to global temperature increase. In the present year of 2025, the global average temperature increase in relation to the pre-industrial era has already reached the established 1.5ºC safety threshold. In this critical moment for humanity and planet earth, a large-scale transition to a more environmentally friendly and sustainable energy economy is of the utmost importance. Green hydrogen emerges as one of the most promising solutions to this energy crisis as a clean, CO_2 neutral and abundant energy carrier. Photoelectrochemical (PEC) cells take advantage of semiconductor material and a metallic counter electrode to directly convert sunlight into chemical energy (in the form of H_2) by water electrolysis. Being one of the most promising technologies for producing green hydrogen, these devices suffer from bandgap restrictions and activation overpotentials that limit light absorption and usually require the use of an external bias, respectively, that limit these devices efficiency. Subsequently, tandem photoelectrochemical (PEC) cells emerge as a strategy to both broaden the light absorption of these devices and release the system from external bias source.

With the goal of finding suitable materials combinations for a tandem PEC cell based on their bandgap, numerical simulations were conducted using an adapted version of S-Q (Shockley-Queisser) limit where we were able to successfully implement loss in photoconversion through abstract factors, that are traceable to real physical behaviours. The simulations results allowed us to identify cupric oxide (CuO) as an amazingly interesting material for tandem PEC devices, with maximum theoretical solar-to-hydrogen efficiencies of 16.7% if paired with hematite and 21% if paired with silicon, when approaching ideal conditions. The implemented model was further expanded to evaluate an unreported tandem device configuration with 3 semiconductor materials in which one of them is connected in parallel. This modification allows the transformation of the maximum solar-to-hydrogen bandgap pairing geometry from a single point (single bandgap pairing) into a line (many bandgap combinations). Additionally, this new configuration would also allow to boost S-Q limit efficiencies of wider bandgap materials like WO_3 and TiO_2 above 18% with an associated hydrogen yield rate above 40% in relation to the incident solar constant.

Motivated by the numerical simulation results, CuO photocathodes research was introduced in the IFIMUP institute for the first time with the final goal of incorporating CuO and hematite in a tandem PEC device.

We were able to develop two fabrication protocols of CuO synthesis, with promising results in both stability and efficiency, which have long term chemical stability issues as CuO can undergo photo-reduction into Cu_2O or Cu during photoelectrochemical operation.

The first fabrication method consists in electrodeposition of Cu followed by a thermal annealing for CuO conversion. In this method, we were able to significantly improve the structural integrity (assessed via Raman spectroscopy) of the photocathodes by optimizing the electrodeposition conditions, where no traceable Cu_2O phase was detected after photoelectrochemical performance. Additionally, the best performing photocathode achieved a remarkable photo current density of 1.44 $mA.cm^{-2}$ @ 0.5 V vs RHE, for optimized film thickness and deposition conditions, corresponding to an ~85% increment in relation to raw deposition conditions.

Subsequently, a second method was implemented that allowed the direct electrodeposition of CuO by a pH variation using the same reagents for copper electrodeposition electrolyte, used in the first method for Cu deposition. In this method, steering induced micro structuring resulted in a highly porous micro-coral like morphology. A photocurrent density of 0.65 $mAcm^{-2}$ @ 0.5 V vs RHE was obtained, but with enhanced structural integrity after PEC characterization. On the other hand, these photocathodes resulted in an improved structural integrity after photoelectrochemical characterization, where no corrosion is perceived in the micro-coral like structure.

With the first optimized method for CuO photocathodes synthesis, two hematite-CuO heterojunctions were fabricated. The best performing heterojunction (FTO-CuO-α-Fe_2O_3: J_{photo} = 0.47 $mAcm^{-2}$ @ 1.23 V vs RHE) resulted in a ~330% increase in the generated photocurrent density in relation to bare hematite (FTO-α-Fe_2O_3: J_{photo} = 0.14 $mAcm^{-2}$), with an additional lowering of ~115 mV vs RHE in the onset potential.

Keywords: [Green hydrogen, Photoelectrochemical water splitting, CuO-Hematite, Photoelectrochemical tandem cells, CuO Photocathodes, Photoconversion]

Table of Contents

List of Tables ix
List of Figures x
Glossary xiv
1. Introduction 1
1.1. Green Hydrogen and its Applications 2
1.2. Photoelectrochemical Cells 3
1.2.1. Tandem Photoelectrochemical (PEC) Cells 5
1.2.2. Materials for Tandem Photoelectrochemical (PEC) cells 7
1.2.3. Strategies for Enhancing Photoelectrochemical Performance 8
1.3. Cupric Oxide (CuO) Properties 11
1.3.1. Structural Properties of Cupric Oxide 11
1.3.2. Optoelectronic Properties 12
1.3.3. Photoelectrochemical Properties 14
2. Numerical Modelling of Photoconversion for Solar-to-Hydrogen Efficiency 15
2.1. Shockley-Queisser (S-Q) limit formalism 15
2.1.1. S-Q limit for Single p-n Junctions 16
2.1.2. S-Q limit for Multi-junction (Tandem) Cells 17
2.1.3. Photoconversion Losses Implementation 18
2.2. Numerical Methods 19
2.2.1. Trapezoidal Rule 20
2.2.2. Gauss-Legendre Quadrature 20
2.2.3. Numerical Maximum Search 21
2.3. Model Implementation and Results 22
2.3.1. Single Junction limit and Loss Factors Implementation 22
2.3.2. Double Junction S-Q limit for STH conversion 22
2.3.3. Breaking the S-Q limit for in series 3-junctions Cells 30

2.4. Conclusions 33
3. Experimental Methods and Characterization Techniques 34
3.1. Materials 34
3.2. Fabrication Techniques and Synthesis Procedures of the Photoelectrodes 34
3.2.1. Substrate Preparation 35
3.2.1.1. Magnetron Sputtering 35
3.2.2. Fabrication Techniques and Synthesis Procedures of the CuO Photocathodes 36
3.2.2.1. Electrodeposition 37
3.2.2.2. Thermal Annealing 39
3.2.3. Fabrication Techniques and Synthesis Procedures of the Hematite-CuO tandem heterojunctions 40
3.2.3.1. Ion Beam Deposition (IBD) 41
3.3. Characterization Techniques 42
3.3.1. Structural Characterizations 42
3.3.2. Morphological Characterizations 43
3.3.3. Electrochemical Characterizations 44
3.3.4. Optical Characterization 44
3.3.5. Photoelectrochemical Performance 45
4. CuO Photocathodes: Electrodeposition of Copper followed by Annealing 46
4.1. Applied Potential Optimization of Copper Electrodeposition 46
4.1.1. Electrolyte Characteristics and Substrate-Electrolyte Electrochemical Dynamics 46
4.1.2. Copper (Cu) Electrodeposition 48
4.1.3. Photoelectrochemical Characterization 50
4.1.4. Morphological Characterization 52
4.1.5. Structural Characterization 52
4.2. Optimization of Film Thickness 53
4.2.1 Electrochemical Cell Geometry 54

4.2.2. Copper (Cu) Electrodeposition 54
4.2.3. Photoelectrochemical Characterization 56
4.2.4. Morphological Characterization 58
4.2.5 Structural characterization 59
4.2.6. Optical Characterization 61
4.3. Conclusions 62
5. CuO Photocathodes: Electrodeposition of Cupric Oxide (CuO) followed by annealing 63
5.1. The effect varying pH 63
5.2. The Effect of Adding Steering during Electrodeposition 65
5.2.1. Direct CuO Electrodeposition 66
5.2.2. Photoelectrochemical characterization 67
5.2.3. Morphological Characterization 68
5.2.4. Structural Characterization 71
5.2.5. Optical Characterization 72
5.3. Conclusions 73
6. Hematite-CuO Tandem Heterojunctions 74
6.1. Copper (Cu) Electrodeposition 74
6.2. Photoelectrochemical Characterization 75
6.3. Morphological Characterization 77
6.4. Structural Characterization 78
6.5. Conclusions 79
7. Conclusions and Future Work 80
7.1 Future Work 81
8. References 83
A – Supplementary Information of Chapter 2 92
B – Supplementary Information of Chapter 3 102

List of Tables

TABLE 1.1: SUMMARY OF LITERATURE RESULTS OF TANDEM PHOTOELECTROCHEMICAL (PEC) CELLS FOR WATER SPLITTING....7
TABLE 1.2: SUMMARY OF SOME LITERATURE RESULTS FOR PHOTOELECTRODES IN PEC WATER SPLITTING. 10
TABLE 1.3: CRYSTALLOGRAPHIC PROPERTIES OF CUPPER AND ITS OXIDE PHASES....11
TABLE 1.4: TIME DURATION TO ACHIEVE PURE PHASE STATE AT DIFFERENT TEMPERATURES. DATA FROM [65]. 12
TABLE 1.5: OPTOELECTRONIC PROPERTIES FOR CUO AND Cu_2O FOUND IN LITERATURE. 13
TABLE 2.1: RESULTS AND LITERATURE COMPARISON FOR MAXIMUM STH CONVERSION USING S-Q LIMIT MODEL.....27
TABLE 2.2: RESULTS FOR THE HEMATITE-CUO PAIRING. **I.** APPROACHING S-Q LIMIT CONDITIONS; **II.** $x10^3$ MORE RECOMBINATION WITH QE PLATEAU AT 0.8. **III.** A MILLION-FOLD MORE RECOMBINATION, WITH QE PLATEAU AT 0.5. 28
TABLE 2.3: RESULTS FOR CUO-SI PAIRING. ALL MINIMUM STH ARE FOR $E_{G,1}$ = 1.3 EV. 29
TABLE 3.1: LIST OF EMPLOYED REAGENTS AND CHEMICALS. 34
TABLE 3.2: ION BEAM DEPOSITION PARAMETERS.....42
TABLE 4.1: ELECTROLYTE COMPOSITION FOR COPPER ELECTRODEPOSITION. 46
TABLE 4.2: BATCH DEPOSITION PARAMETERS.....48
TABLE 4.3: PARAMETERS OF THE VARIOUS $\sigma_{DEP}(t)$ REGRESSIONS. 50
TABLE 4.4: SUMMARY RESULTS FOR THE POTENTIAL STUDY: ABSOLUTE PHOTO-CURRENT DENSITY J_{PHOTO} @ 0.5 V AND V_{ONSET} VS RHE.....51
TABLE 4.5: BATCH DEPOSITION TIMES AND THEORETICALLY EXPECTED THICKNESS.....55
TABLE 4.6: PHOTOELECTROCHEMICAL RESULTS OF THE THICKNESS STUDY SAMPLE BATCH. 57
TABLE 4.7: SUMMARY OF LINEAR REGRESSION AND BANDGAP CALCULATION RESULTS. NOTE: $Egap$ UNCERTAINTY ($\mu(Egap)$) IS CALCULATED USING ERROR PROPAGATION FORMULA CONSIDERING THE LINEAR REGRESSION SLOPE AND INTERCEPT STANDARD DEVIATION.....62
TABLE 5.1: DEPOSITION CONDITIONS FOR BATCH FABRICATION. 66
TABLE 5.2: SUMMARY RESULTS FOR F1 & F2 PHOTO-RESPONSE RESULTS. 68
TABLE 5.3: FIT RESULTS SUMMARY AND RESPECTIVE CALCULATED INDIRECT AND DIRECT BANDGAPS. 72
TABLE 5.4: ESTIMATED BANDGAPS AND UNCERTAINTIES CONSIDERING ALL SAMPLES FROM CHAPTER 4 AND 5. 73
TABLE 6.1: SUMMARY RESULTS FOR THE HETEROJUNCTIONS PHOTOELECTROCHEMICAL CHARACTERIZATION.....76

List of Figures

FIGURE 1.1: **I.** GLOBAL AVERAGE LAND-SEA SURFACE TEMPERATURE LEVEL IN RELATION TO PRE-INDUSTRIAL LEVELS. ADAPTED FROM [110]. **II.** GLOBAL ENERGY DEMAND GROWTH IN 2024 BY ENERGY SECTOR. 54% OR ENERGY DEMAND GROWTH IS STILL SATISFIED WITH GREENHOUSE GAS EMITTING ENERGY SECTORS. REPRESENTED WITH DATA FROM [1]. 1

FIGURE 1.2: TYPES OF HYDROGEN ACCORDING TO CURRENT EU DIRECTORY AND DIAGRAM OF A GREEN HYDROGEN BASED ECONOMY. BASED ON [4,5,11,12]..... 2

FIGURE 1.3: **I.** ILLUSTRATION OF A PHOTOCATHODE (P-TYPE SEMICONDUCTOR) PEC CELL. **II.** ILLUSTRATION OF THE ENERGY DIAGRAM OF PHOTOCATHODE PEC CELL. εf − FERMI LEVEL. BASED ON [3]. 3

FIGURE 1.4: **I.** ILLUSTRATION OF A HYPOTHETICAL TANDEM PEC DEVICE. INSPIRED IN [3,17]. **II.** ILLUSTRATION OF TANDEM PEC CELL ENERGY DIAGRAM. INSPIRED IN [3,17]. 6

FIGURE 1.5: ILLUSTRATION OF THE ABSORPTION PROCESS OF 2-JUNCTION TANDEM CELL. 6

FIGURE 1.6: GENERAL REQUIREMENTS FOR A SUSTAINABLE PHOTOELECTRODE. INSPIRED IN [100]..... 7

FIGURE 1.7: SOME OF THE ADEQUATE MATERIALS FOR PEC CELL INCORPORATION. REPRODUCED FROM [111]. 8

FIGURE 1.8: ILLUSTRATION OF VARIOUS REPORTED TECHNIQUES FOR PEC IMPROVEMENT. **I. DOPING. II. CO-CATALYST** NiP_2 DEPOSITED ON A PHOTOELECTRODE SURFACE, ABOVE A TI PASSIVATION LAYER. ADAPTED FROM [30]. **III. NANOSTRUCTURING** EXAMPLE: NANOWIRES. ADAPTED FROM [3]. **IV. PASSIVATION LAYER. V. P-N JUNCTION** PHOTOCATHODE WITH ADEQUATE BAND STRUCTURE FOR WATER SPLITTING..... 9

FIGURE 1.9: **I.** PHASE TRANSITION DIAGRAM FOR CU-O BINARY SYSTEM AS FUNCTION OF O2 PRESSURE AND TEMPERATURE. REPRODUCED FROM [66] **II.** RESUME FOR X-RAY SPECTRUM FOR THIN FILMS CU-O BINARY SYSTEM, FOR VARIOUS TEMPERATURES AT 3H TIMESTAMP. REPRODUCED FROM [65]. 12

FIGURE 1.10: **I.** ILLUSTRATION OF DIFFERENT TYPES OF SPATIAL CONFINEMENT IN K-SPACE. ADAPTED FROM [112]. **II.** ILLUSTRATION ON BANDGAP WIDENING EFFECT WITH PARTICLE SIZE REDUCTION. ADAPTED FROM [112]..... 13

FIGURE 1.11: **I.** (A) J-V CURVES WITH CHOPPED ILLUMINATION FOR CUO NANOWIRES WITH PT CO-CATALYST (B) J-t UNDER ILLUMINATION FOR 10 MIN. REPRODUCED FROM [115] **II.** A. J-V CURVES WITH CHOPPED ILLUMINATION. B. J-t FOR CHOPPED ILLUMINATION DURING 8MIN @ 0.3 V VS RHE. REPRODUCED FROM [116]. 14

FIGURE 2.1: **I.** GRAPHICAL REPRESENTATION OF THE QE ASSUMED IN S-Q LIMIT VS THE SIMULATED PROFILE BY EXPRESSION 2.17, FOR $A \epsilon [0.2,1]$, $B = 5$ AND $Egap = 1.1\ eV$. **II.** GRAPHICAL REPRESENTATION OF SIMULATED QE BY EXPRESSION 2.15 AS FUNCTION OF BANDGAP, FOR $A = 0.8$ AND $B = 3$..... 19

FIGURE 2.2: **I.** LOGARITHM VALUE OF THE NUMERICAL INTEGRATION VALUE, AS A FUNCTION OF THE SAMPLE POINTS. **II.** LOGARITHM OF PERCENTUAL ERROR DIFFERENCE BETWEEN SUCCESSIVE INTEGRALS FOR VARIOUS BANDGAPS FOR $EG \in 0.4{,}3$ EV. FORMULA: $\Delta E = In - In - 1In - 1 \times 100$. 23

FIGURE 2.3: **I.** S-Q LIMIT AS A FUNCTION OF BANDGAP FOR: $fc = 1$ (ONLY RADIATIVE RECOMBINATION) AND $fc = 10 - 3, 10 - 6$ (A THOUSAND AND MILLION-FOLD MORE RECOMBINATION THAN RADIATIVE). **II.** J-V PROFILES FOR 1.1 EV SI CONSIDERING THE SAME fc FACTORS AS IN (I). 23

FIGURE 2.4: **I.** IMPLEMENTED MODEL WITH SIMULATED QE LOSSES, FOR $B = 5$ ACCORDING TO EXPRESSION 2.13. **II.** VISUALIZATION OF THE LOSSES IMPACT ON J-V BEHAVIOR FOR 1.1 EV SI..... 24

FIGURE 2.5: **I.** JPHOTO-V CHARACTERISTICS WITH VARYING LOSS FACTOR: $A \in 1,0.7,0.5,\ fc \in 1,10-3,10-6$. **II.** LOSS FACTORS IMPACT IN ENERGY CONVERSION. 25

FIGURE 2.6: EQUIVALENT CIRCUIT OF A 2-JUNCTION TANDEM PEC. 26

FIGURE 2.7: **I.** LITERATURE REPRODUCTION CONSIDERING $\Delta U = 3.23\ eV$ [17]. **II.** S-Q FOR STH EFFICIENCY CONSIDERING $\Delta V_{ACT} = 2V$ 27

FIGURE 2.8: STH EFFICIENCY SIMULATIONS FOR HEMATITE-CUO BANDGAP PAIRING. I. $fc = 1, A = 1\ \&\ B = 5$. II. $fc = 10-3,\ A = 0.8\ \&\ B = 5$. III. $fc = 10-6, A = 0.5\ , B = 5$. 28

FIGURE 2.9: GRAPHICAL REPRESENTATION OF STH AS FUNCTION OF WIDE BANDGAP VALUE FOR 1.1 EV SI. 29

FIGURE 2.10: **I.** MAXIMUM STH EFFICIENCY AS A FUNCTION OF THE BOTTOM JUNCTION BANDGAP VALUE. **II.** MAXIMUM STH EFFICIENCY FOR WIDE AND MID BANDGAP PAIRINGS, FOR A FIXED 1.1 EV NARROW BANDGAP 30

FIGURE 2.11: **I.** ILLUSTRATION OF HYPOTHETICAL TANDEM PEC-PV-EC DEVICE. **II.** EQUIVALENT CIRCUIT OF THE DESIGNED HYBRID SYSTEM. 31

FIGURE 2.12: **I.** STH EFFICIENCY OF THE SYSTEM FOR $Eg3 = 1.1$ EV. **II.** H_2 PRODUCTION RATE AS A FUNCTION OF BANDGAP PAIRING FOR 1.1 EV NARROW BANDGAP: OUTPUT ENERGY IN HYDROGEN NORMALIZED TO INCIDENT SOLAR ENERGY. ..32

FIGURE 3.1: ILLUSTRATION OF THE SUBSTRATE PREPARATION PROCEDURE. 35

FIGURE 3.2: **I.** PICTURE OF THE UTILIZED MAGNETRON SPUTTERING DURING DEPOSITION. **II.** ILLUSTRATION OF A MAGNETRON SYSTEM WORKING PRINCIPLES. REPRODUCED FROM [84] 36

FIGURE 3.3: ILLUSTRATION OF THE DEVELOPED SYNTHESIS ROUTES PROCEDURES. 37

FIGURE 3.4: **I.** PICTURE OF THE ELECTRODEPOSITION WORKING STATION, WITH ILLUSTRATION OF THE CONNECTION WITH THE AUTOLAB STATION AND COMPUTER. **II.** ILLUSTRATION OF A 3-ELECTRODE ELECTROCHEMICAL CELL CIRCUIT. V – VOLTMETER, A- AMMETER. 38

FIGURE 3.5: **I.** PHOTOGRAPH OF THE ANNEALING FURNACE IN THE HEATING PROCESS. **II.** ILLUSTRATION OF THE QUARTZ TUBE, WITH ILLUSTRATION OF THE HOMOGENEOUS TEMPERATURE ZONE WHERE THE SAMPLES ARE PLACED. 39

FIGURE 3.6: PROCEDURE ILLUSTRATION OF ROUTE'S A1 AND A2 FOR HEMATITE-CUO HETEROJUNCTION SYNTHESIS. 41

FIGURE 3.7: **I.** PHOTOGRAPH OF IBD SYSTEM FROM COMMONWEALTH SCIENTIFIC AT CEMUP CLEAN-ROOM FACILITY. REPRODUCED FOM [95]. **II.** ILLUSTRATION OF THE INSIDE CHAMBER OF A IBD SYSTEM AND ITS OPERATING COMPONENTS. ADAPTED FROM [93]. 41

FIGURE 3.8: **I.** RAMAN MICROSCOPY STATION AT IFIMUP. **II.** ILLUSTRATION OF RAMAN SCATTERING (INELASTIC) AND RAYLEIGH SCATTERING (ELASTIC) EFFECT ON THE SCATTERED PHOTON'S WAVELENGTH – OR EQUIVALENTLY: ENERGY. REPRODUCED FROM [103] 42

FIGURE 3.9:: ILLUSTRATION OF THE PHOTOELECTROCHEMICAL CHARACTERIZATION STATION. ALL PEC CHARACTERIZATIONS ARE PERFORMED AT LEPABE, FEUP. 45

FIGURE 4.1: CYCLIC VOLTAMMETRY'S (CV) FOR THE REPRESENTED SOLUTION IN TABLE 4.1, FOR THE PHOTOELECTRODES SUBSTRATES: FTO-AU. **I.** VARYING SWEEP RATE FOR THE SAME SUBSTRATE. **II.** 10 MV/S CV FOR CATHODIC CURRENT DENSITY J. 47

FIGURE 4.2: SELECTED DEPOSITION POTENTIALS FOR SAMPLE FABRICATION 48

FIGURE 4.3: **I.** ELECTRODEPOSITION $J(t)$ CHARACTERISTICS. **II.** DEPOSITED CHARGE DENSITY OVER TIME (σDEP(t)) 49

FIGURE 4.4: DEPOSITION RATES FOR CHARGE DENSITY AND CU. 50
FIGURE 4.5: PHOTOELECTROCHEMICAL PERFORMANCE OF THE FABRICATED PHOTOELECTRODES. THE SAMPLES ARE REPRESENTED IN DIFFERENT PLOTS WITH IBD REFERENCE FOR EASE IN THE CURVE'S VISUALIZATION. **I.** A1 AND A2 SAMPLES PHOTO RESPONSE. RED POINT: CU (II) TO CU POTENTIAL, EQUATION 4.6. **II.** A3 TO A5 SAMPLES PHOTO RESPONSE 51
FIGURE 4.6: SEM MICROGRAPHS OF THE CUO PHOTOCATHODES POSTERIOR TO PHOTOELECTROCHEMICAL CHARACTERIZATION. 52
FIGURE 4.7: RAMAN SPECTRUM OF SAMPLES A2 TO A5 WITH Cu_2O AND CUO LITERATURE RAMAN SHIFT PEAKS. CUO MODES: [85]; Cu_2O MODES: [86]. 53
FIGURE 4.8: **A**: PREVIOUS SET-UP CONFIGURATION. **B**: EMPLOYED SET-UP CONFIGURATION IN THIS SECTION. 54
FIGURE 4.9: ELECTRODEPOSITION J-t AND σ-t CHARACTERISTICS FOR THE DEPOSITED CU THIN FILMS. 55
FIGURE 4.10: COMPARISON OF FINAL DEPOSITED CHARGE DENSITY WITH PRIOR CALIBRATION FROM SECTION 4.1. 55
FIGURE 4.11: AS DEPOSITED AND AS ANNEALED PHOTOGRAPHS OF THE SAMPLES. 56
FIGURE 4.12: PHOTOELECTROCHEMICAL RESULTS. **I.** J_{PHOTO}-V PERFORMANCE. **II.** J @ 0.5 V VS RHE AS FUNCTION OF SAMPLE THICKNESS/DEPOSITION TIME. 57
FIGURE 4.13: AS ANNEALED AND POST SOLAR PHOTOGRAPHS OF SAMPLES B1 TO B4. 58
FIGURE 4.14: SEM MICROGRAPHS OF SAMPLES B1-B5 AT THE 20µM AND 1µM RANGE. 58
FIGURE 4.15: PROBABILITY DENSITY HISTOGRAMS FOR: I. SAMPLE B1; II. SAMPLE B2; III. SAMPLE B3. FITTED NORMAL DISTRIBUTIONS. 59
FIGURE 4.16: BATCH RAMAN SPECTRA. 59
FIGURE 4.17: COMPARISON BETWEEN THE STRUCTURE OF THE PHOTOCATHODES AFTER PHOTO-PERFORMANCE CHARACTERIZATION, BETWEEN EQUIVALENT SAMPLES FABRICATED IN DIFFERENT ELECTROCHEMICAL SET-UPS 60
FIGURE 4.18: STRAIN AS FUNCTION OF THICKNESS, VISUALIZED THROUGH $\Delta\Omega_{\mathrm{VIB}}$ VS DEPOSITION TIME RELATION. 61
FIGURE 4.19: FIT VISUALIZATION ON KUBELKA-MUNK FUNCTIONS TRANSITION SLOPE FOR: **I.** INDIRECT ALLOWED TRANSITIONS. **II.** DIRECT ALLOWED TRANSITIONS. 61
FIGURE 5.1: SOLUTION PHOTOGRAPHS OF THE SOLUTION AS A FUNCTION OF PH, DURING STEERING. 64
FIGURE 5.2: **I.** CYCLIC VOLTAMMETRY WITH 20 MV/S SCAN RATE AS A FUNCTION OF PH, AT 400 RPM. **II.** ZOOM IN ANODIC REGION FOR PH 13 CYCLIC VOLTAMMETRY. 65
FIGURE 5.3: AFTER CV SAMPLES, SHOWING CLEAR DEPOSITION ABOVE PH 10.8. 65
FIGURE 5.4: STEERING EFFECT ON THE SOLUTION STATE. I. NO STEERING EFFECT, PHOTOGRAPH DURING DEPOSITION. II. STEERING RATE: 400 RPM. 66
FIGURE 5.5: **I.** ZOOM IN $t \in [0,5]$MIN WINDOW FOR ELECTRODEPOSITION $J(t)$ CHARACTERISTICS. **II.** $\sigma_{\mathrm{DEP}}(t)$ CHARACTERISTICS FOR $t \in [0,10]$ MIN. 66
FIGURE 5.6: I. PHOTOELECTROCHEMICAL J-V FOR $V \in 0.2,0.8$ V VS RHE. **II.** MORE STABLE CHEMICAL WINDOW $V \in 0.4,0.8$ V VS RHE. 67
FIGURE 5.7: BEFORE AND AFTER PHOTOELECTROCHEMICAL CHARACTERIZATION PHOTOGRAPHS OF SAMPLES F1 AND F2. 68
FIGURE 5.8: SEM MICROGRAPHS OF SAMPLE F1. 69

FIGURE 5.9: SEM MICROGRAPHS OF SAMPLE F2 (NO STEERING). 69
FIGURE 5.10: AS ANNEALED AND POST SOLAR MEASUREMENTS SEM IMAGES OF SAMPLES F1 AND F2. MARO IMAGES: X10^3 MAGNIFICATION – 100 µM; MICRO IMAGES: X10^5 MAGNIFICATION – 1 µM. 70
FIGURE 5.11: EDS SPECTRUM FOR SAMPLES OF DIFFERENT ZONE TYPES. BLACK BOX: SN CONTAINING ENERGY PEAKS; GREEN BOX: O AND CU CONTAINING ENERGY PEAKS. 70
FIGURE 5.12: RAMAN SPECTRUMS FOR F SAMPLES. **I.** POST SOLAR MEASUREMENTS F1 AND F2 SPECTRUMS; **II.** AS ANNEALED AND POST SOLAR SPECTRUM OF F2 SAMPLE. 71
FIGURE 5.13: TAUC PLOTS USING KUBELKA-MUNK FUNCTIONS FOR INDIRECT ($n = 1/2$) AND DIRECT ($n = 2$) TRANSITIONS. 72
FIGURE 6.1: **I.** ELECTRODEPOSITIONS $J(t)$ CHARACTERISTICS FOR BOTH SUBSTRATES. **II.** DEPOSITED CHARGE DENSITY $\sigma\mathrm{DETP}(t)$ CHARACTERISTICS 74
FIGURE 6.2: PICTURES OF THE FABRICATED SAMPLES BEFORE AND AFTER ANNEALING. 75
FIGURE 6.3: **I.** CATHODIC ELECTROCHEMICAL WINDOW FOR THE FABRICATED HETEROJUNCTIONS. **II.** ANODIC ELECTROCHEMICAL WINDOW OF THE FABRICATED JUNCTIONS. 76
FIGURE 6.4: SAMPLE PHOTOGRAPHS AFTER PHOTOELECTROCHEMICAL CHARACTERIZATION. 77
FIGURE 6.5: SEM MICROGRAPHS OF THE FABRICATED HETEROJUNCTIONS, AFTER PHOTOELECTROCHEMICAL CHARACTERIZATION. MICROGRAPHS FOR SAMPLE B2 (5MIN) FROM SECTION 4.2 ARE INCLUDED FOR CUO MORPHOLOGY COMPARISON. 77
FIGURE 6.6: ACQUIRED RAMAN SPECTRUMS OF SAMPLES J1 AND J2, AT DIFFERENT REGIONS FOR LAYER COMPOSITION ASSESSMENT. 78

Glossary

PEC	Photoelectrochemical
HER	Hydrogen Evolution Reaction
OER	Oxygen Evolution Reaction
STH	Solar to Hydrogen
PCE	Power Conversion Efficiency
RHE	Reversible Hydrogen Electrode
WE	Working Electrode
RE	Reference Electrode
CE	Counter Electrode
PV	Photovoltaic
SEM	Scanning Electron Microscopy
UV-VIS-NIR	Ultra Violet – Visible – Near Infrared
CBM	Conduction Band Minimum
VBM	Conduction Band Maximum
VB	Valence Band
CB	Conduction Band
FTO	Fluorine-doped Tin Oxide
E_g	Band Gap
η_{HER}	Hydrogen Evolution Overpotential
η_{OER}	Oxygen Evolution Overpotential
TCO	Transparent Conductive Oxyde
IBD	Ion Beam Deposition

IFIMUP	Institute of Physics for Advanced Materials, Nanotechnology and Photonics at the University of Porto
LEPABE	Laboratory for Process Engineering, Environment, Biotechnology and Energy at the Faculty of Engineering of the University of Porto

1. Introduction

Energy is a primary and fundamental resource in our daily lives, a structural pillar of civilization as we know it, as it was and as it will be. Over the last two centuries, the use of fossil fuels has been contributing to global warming and climate changes that we experience daily, where emission of CO_2 and other greenhouse gases leads to a rise in atmospheric concentrations of these gases, resulting in an increase of the global average temperature.

Under the Paris agreement, the global average temperature rise should be kept well below 2ºC in relation to pre-industrial levels, with efforts pursued to limit the warming to 1.5ºC [109]. According to these established thresholds, keeping the temperature increase bellow 1.5ºC would significantly reduce the risk of increasingly frequent and severe weather events such as heat waves, wildfires, heavy precipitation and other extreme weather phenomena [109].

The most recent data shows we have already reached a 1.5ºC increase in sea-land surface level average temperature in relation to pre-industrial period, as figure 1.1 (i) details [110]. This increase in temperature is of course related to an increase in greenhouse gases emissions. This increment in emissions is, in its place, related with global energy demand growth, that in its vast majority (around 54%) is still satisfied by greenhouse gases emitting energy sectors [1], as illustrated in figure 1.1 (ii). Because of the outlined reasons, a rapid transition to a cleaner, sustainable and environmentally friendly energy economy is not only urgent but imperative. In this transition, green hydrogen (H_2) may play a central and indispensable role.

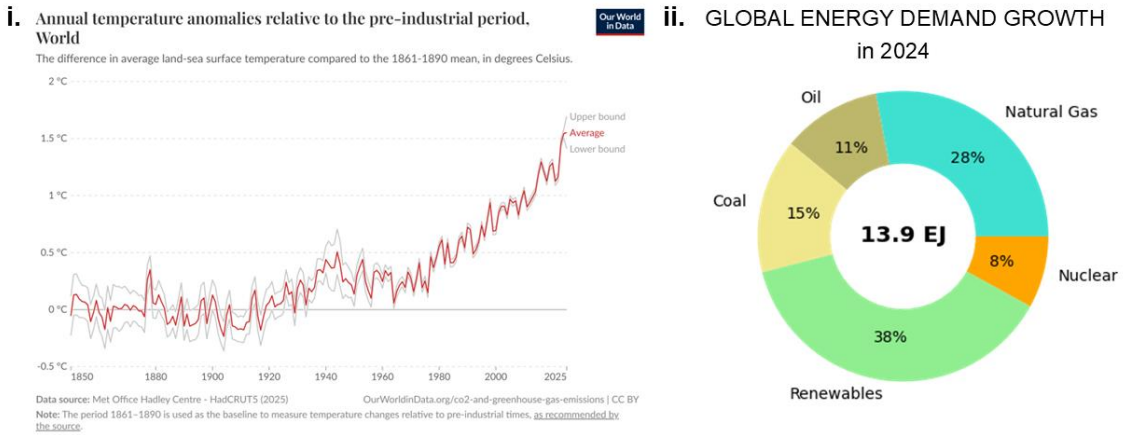


Figure 1.1: **i.** Global average land-sea surface temperature level in relation to pre-industrial levels. Adapted from [110]. **ii.** Global Energy Demand Growth in 2024 by energy sector. 54% of energy demand growth is still satisfied with greenhouse gas emitting energy sectors. Represented with data from [1].

1.1. Green Hydrogen and its Applications

Green Hydrogen emerges as a clean, non-toxic, abundant and renewable energy carrier: an alternative for energy storage. Hydrogen can be obtained from many sources and according to the current EU directory, hydrogen is categorized by colors and labels depending on its environmental impact, as outlined in figure 1.2 [11,20].

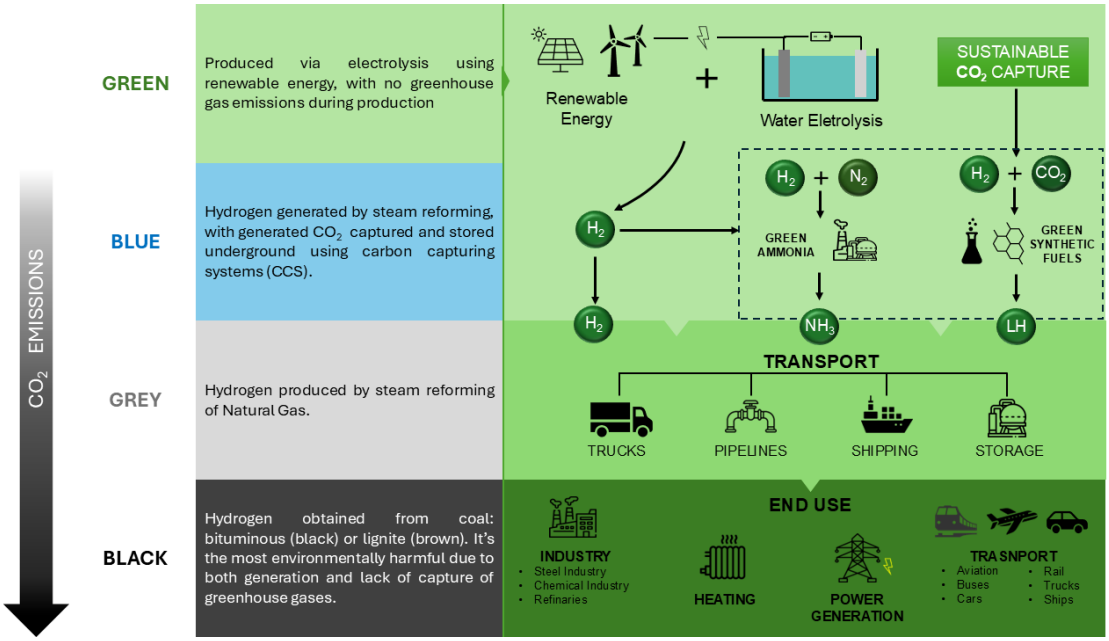


Figure 1.2: Types of Hydrogen according to current EU directory and Diagram of a Green Hydrogen based economy. Based on [4,5,11,12].

Green hydrogen is obtained from renewable energy powered electrolysis, being CO_2 neutral by default. Hydrogen has a remarkably high gravimetric energy density ($33.3\ \mathrm{kW \cdot h/kg}$ [5]), but a very low specific density, which results in a low volumetric energy density ($\sim 3\mathrm{W \cdot h/L}$ [6]). Because storing size also matters, hydrogen may be compressed and stored for later use [6,7,9], increasing the overall volumetric energy density. Devices like fuel cells can take advantage of the stored hydrogen, where H_2 molecules react with the cell's catalyst and ambient O_2 to produce electricity and water vapor (H_2O).

As detailed in figure 1.2, green H2 can also be processed with other chemicals like nitrogen (N_2) or atmospheric CO_2 to produce green synthetic fuels like ammonia (NH_3) or liquid hydrocarbons (LH) [4,5,9]. These are also carbon neutral alternatives, that promote lower gravimetric energy densities but higher volumetric energy densities. At the end, either hydrogen or its derivatives (NH_3, LH), may be used in industry, power generation applications or transport, as detailed in figure 1.2.

Although the enormous potential of a hydrogen-based economy, green hydrogen is still too expensive to be economically competitive (green H_2 costs more than twice the price of grey hydrogen [11]). Consequently, around 96% of the consumed hydrogen in Europe is still obtained from methane reforming (Grey hydrogen), which releases considerable amounts of CO_2 (around 7.3 Mt) [11].

1.2. Photoelectrochemical Cells

As outlined in section 1.1, green hydrogen should be economically competitive for a viable hydrogen-based economy. The device's fabrication cost, efficiency and lifetime greatly influence the overall green hydrogen cost. Photoelectrochemical Cells (PEC cells) are one of the most promising, sustainable and environmentally friendly technologies for green hydrogen production [3,15,16]. These devices directly convert sunlight & water into chemical energy using a semiconductor material to directly promote the electrolysis of water, separating H_2O molecules into H_2 and O_2 molecules [3,13,14,15,16]. A general accepted threshold for solar-to-hydrogen (STH) efficiency for commercial viability of PEC cells is 10% [3].

A traditional PEC cell consists of a single semiconductor material that either acts as a photoanode or photocathode (n-type or p-type, respectively), and a metallic counter electrode (CE), both submerged in an aqueous based electrolyte [3,13,14,15,16]. Figure 1.3 shows an illustration of a photocathode PEC cell (i) and its energy diagram (ii).

When the semiconductor material absorbs an incident photon with energy above its bandgap, an electron-hole pair is generated:

$$\text{semiconductor} + h\nu \rightarrow \mathrm{e}^- + \mathrm{h}^+, \qquad \text{for } h\nu > E_g \tag{1.1}$$

Where E_g is the bandgap of the semiconductor and $h\nu$ is the photon's energy.

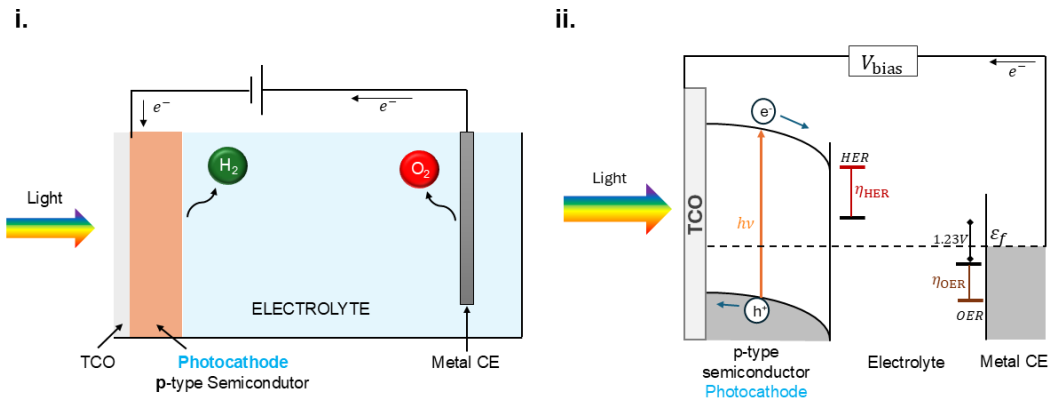


Figure 1.3: **i.** Illustration of a photocathode (p-type semiconductor) PEC cell. **ii.** Illustration of the Energy Diagram of photocathode PEC cell. ε_f – Fermi Level. Based on [3].

If the semiconductor has conduction band maximum (CBM) above hydrogen evolution reaction potential (HER), and valence band minimum (VBM) below oxygen evolution reaction potential (OER), it has suitable band edges for water splitting and can exchange charge with the electrolyte. The electrolyte-semiconductor interface has a built-in electric field, associated with the band pinning illustrated in figure 1.3 (ii). In the case of p-type semiconductors (photocathodes), this field drives photogenerated holes towards the counter electrode (CE) and photogenerated electrons towards the semiconductor-electrolyte interface where they reduce water to produce hydrogen.

Following charge generation (equation 1.1), electrochemical water electrolysis takes place. For acidic electrolysis [3]:

$$\text{HER:} \quad 4\text{H}^+ + 4\text{e}^- \rightarrow 2\text{H}_2 \qquad E^0_{\text{red}} = 0.0 \text{ V vs NHE} \qquad (1.2)$$

$$\text{OER:} \quad 2\text{H}_2\text{O} + 4\text{h}^+ \rightarrow 4\text{H}^+ + \text{O}_2 \qquad E^0_{\text{ox}} = -1.299 \text{ V vs NHE} \qquad (1.3)$$

For alkaline electrolysis:

$$\text{HER:} \quad 4\text{H}_2\text{O} + 4\text{e}^- \rightarrow 2\text{H}_2 + 4\text{HO}^- \qquad E^0_{\text{red}} = -0.828 \text{ V vs NHE} \qquad (1.4)$$

$$\text{OER:} \quad 4\text{HO}^- + 4\text{h}^+ \rightarrow 2\text{H}_2\text{O} + \text{O}_2 \qquad E^0_{\text{ox}} = -0.401 \text{ V vs NHE} \qquad (1.5)$$

The red/ox potentials of HER and OER reactions enable the calculation of the variation in Gibbs free energy (ΔG^0) [3]:

$$\Delta E^0_{redox} = E^0_{red} + E^0_{ox} = -1.299 \text{ V vs NHE} \qquad (1.6)$$

$$\Delta G^0 = -nF\Delta E^0_{redox} = 237 \text{ kJ/mol} \qquad (1.7)$$

Where $n = 2$ is the number of electrons involved in the reaction and $F = 96485 \text{ C/mol}$ is Faraday's constant. The solar-to-hydrogen (STH) efficiency of the system can be calculated by the ratio of the generated power density, by the incident light intensity:

$$\text{STH}(\%) = \frac{\phi_{\text{H}_2} \cdot \Delta G^0}{\text{Solar}_\text{c}} \qquad (1.8)$$

Where Solar_c (solar constant in $\text{kW} \cdot \text{cm}^{-2}$) is the incident light intensity and ϕ_{H_2} is the generated hydrogen flux ($\text{mol} \cdot \text{s}^{-1}\text{cm}^{-2}$).

Under ideal conditions, the later requirements impose a minimum bandgap of 1.5 eV for water splitting [3]. However, outside ideal conditions there are activation overpotentials for driving both HER and OER reactions. These overpotentials, illustrated in figure 1.3 (ii) as η_{HER} and η_{OER}, arise because of deviations from ideal conditions, and individual characteristics of semiconductors. For instance, in the case of hematite (α-Fe_2O_3), that does not have a suitable CVM to drive HER reaction, an intrinsic overpotential emerges due to this band edge mismatch.

Consequently, a practical and generally accepted minimum bandgap of $2\ \mathrm{eV}$ is required to drive water splitting [3], which limits the absorption of the solar spectrum to the visible-UV regions. Even so, many times these systems still require an external bias to promote the reaction, which decreases the overall efficiency of the device. In an equivalent way to relation 1.8, STH efficiency can also be written as:

$$\mathrm{STH}(\%) = \eta_{\mathrm{F}} \cdot \frac{J_{\mathrm{photo}} \cdot (1.23 - V_{\mathrm{bias}})}{\mathrm{Solar}_{\mathrm{c}}} \qquad (1.9)$$

For biased operation of the device [3]. Where η_{F} is the faradaic efficiency, J_{photo} is the generated photocurrent and V_{bias} is the applied bias. According to expression 1.9, applying a bias reduces the overall STH efficiency and for $V_{\mathrm{bias}} \geq 1.23\ \mathrm{V}$ the efficiency is zero. Due to the mentioned limitations, a cost-effective, stable and sustainable PEC cell that meets the commercial efficiency threshold has not yet been reported.

1.2.1. Tandem Photoelectrochemical (PEC) Cells

Tandem Photoelectrochemical cells emerge as way to release a traditional single photoelectrode PEC cell from the need of an external bias. These cells, also known as tandem or "3rd Generation Solar Cells" in the photovoltaics field, take advantage of more than one semiconductor material to conduct a broader absorption and more efficient energy conversion of the solar spectrum.

Unlike traditional PEC's, these devices possess more than one semiconductor material. This extra semiconductor material can replace the metallic CE, resulting in a device with both a photocathode and photoanode, as illustrated in figure 1.4. As a result, the photocathode only needs a suitable conduction band edge to drive HER and equivalently, the photoanode only requires a suitable valence band edge to drive OER. The ohmic contact represented in figure 1.4 (ii) acts as a hole recombination layer and isolates the photoelectrodes from each other. The series connection promotes higher operational voltages for the tandem cell, in relation to the isolated photoelectrodes, potentially releasing the system from external bias.

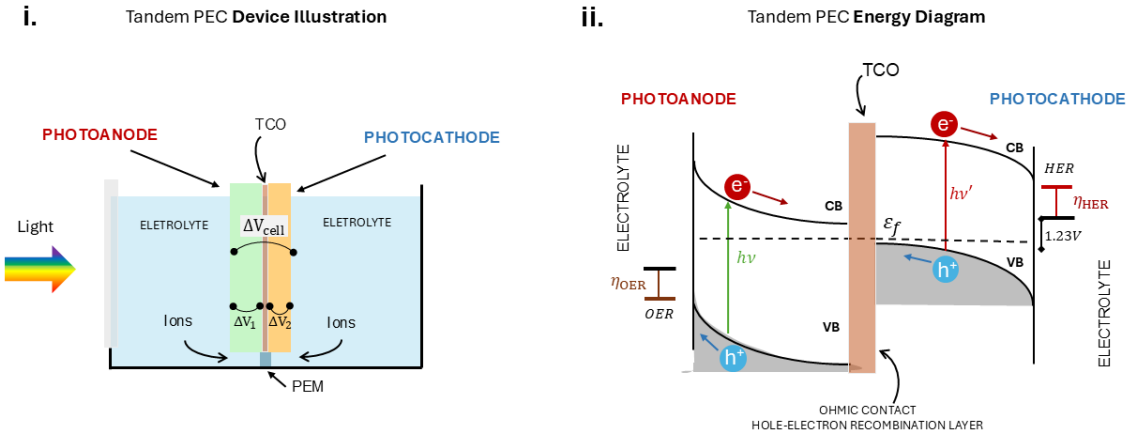


Figure 1.4: **i.** illustration of a hypothetical tandem PEC device. Inspired in [3,17]. **ii.** Illustration of tandem PEC cell energy diagram. Inspired in [3,17].

Additionally, as the photoelectrodes voltages add, it is possible to choose lower bandgap semiconductors than the $2\ \mathrm{eV}$ threshold mentioned in section 1.2. Consequently, the narrower bandgap of the second semiconductor promotes a broader absorption of the solar spectrum, as illustrated in figure 1.5.

First, photons with energy above $E_{g,1}$ are absorbed in the 1st "wide" bandgap material. Posteriorly, the remaining photons with energies lying between $E_{g,2}$ and $E_{g,1}$ are absorbed in the 2nd "narrow" bandgap material. Consequently, light should pass through wider bandgap materials first, so the narrower gap semiconductors still have photons to generate current. The later property already suggests that the bandgaps of each semiconductor, as well as their positioning, is a very important property of these systems: as the photoelectrodes are connected in series, the one with shortest generated current density limits the current density of the system.

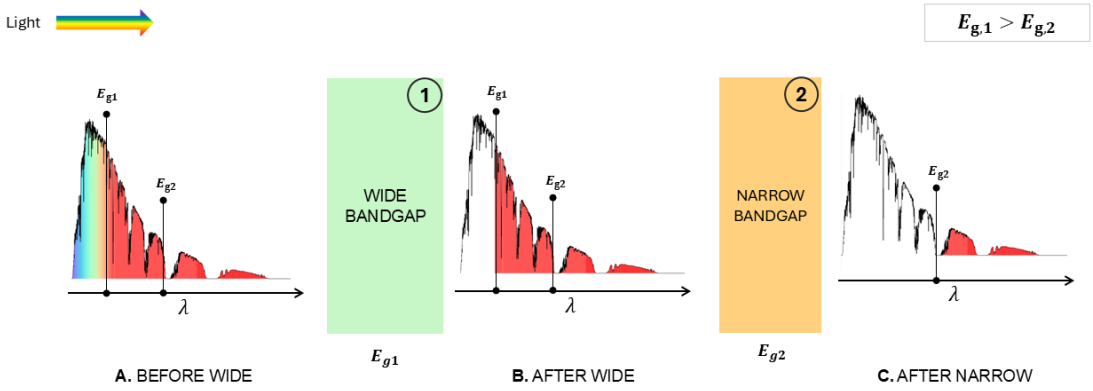


Figure 1.5: Illustration of the absorption process of 2-junction tandem cell.

Therefore, adequate bandgap pairing of the semiconductors band gaps is a crucial factor in designing such systems. Remarkably, even for losses as big as $1\,\mathrm{eV}$ per semiconductor, maximum theoretical STH efficiencies as high as 21.6% for an adequate bandgap pairing of $1.89\,\mathrm{eV}$ and $1.34\,\mathrm{eV}$ are reported in literature [17]. Efficiencies as high as 19.9% have already been achieved with these devices, but in this case only 30min of stability was achieved [56], as listed in table 1.1.

Photoanode	Photocathode	J_{photo} / (mA/cm^2)	STH / (%)	Stability	Year	Source
W:$BiVO_4$/Co-Pi	Cu_2O/RuO_x	0.71	0.87	-	2014	[50]
$BiVO_4$/$NiFeO_x$-Bi	$(ZnSe)_{0.85}(CIGS)_{0.15}$CdS/Ti/Mo/Pt	0.89	0.91	30 min	2016	[51]
$BiVO_4$	CZTS/CdS/HfO_2/Pt	0.85	1.05	10h	2018	[52]
Mo:$BiVO_4$/$NiFeO_x$	$Cu_2O/Ga_2O_3/TiO_2/RuO_x$	2.5	3	12h	2018	[53]
$BiVO_4$	Si-I MIS	1.55	1.9	15 min	2020	[54]
CZTS-$BiVO_4$	CZTS/HfO_2/CdS/HfO_2	14.6	3.17	60 h	2021	[55]
GaInAs / GaAs	AlInPOx/AlInP/GaIn P	15.7	19	30 min	2022	[56]
$BiVO_4$	TD-Cu_2ZnSnS_4	6.5	8	168 h	2023	[57]

Table 1.1: Summary of literature results of tandem photoelectrochemical (PEC) cells for water splitting.

1.2.2. Materials for Tandem Photoelectrochemical (PEC) cells

Throughout sections 1.2 and 1.2.1, several working principles of PEC cells have been aborded. Alongside the mentioned efficiency requirements, the sustainability and environmental impact of these devices are of the utmost importance. The ideal synergy between different aspects of these devices is illustrated in figure 1.6.

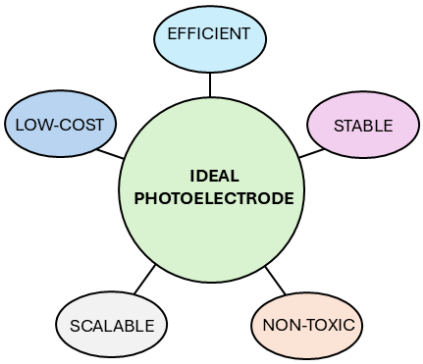


Figure 1.6: General requirements for a sustainable photoelectrode. Inspired in [100].

As detailed in figure 1.6, an ideal photoelectrode should be efficient, low-cost, non-toxic, scalable an possess long term stability in aqueous environments. In addition to the

physical requirements for driving water splitting, the previous properties restrict the materials choice for these devices.

There are some materials that satisfy the listed conditions, figure 1.7 outlines some of these materials. This figure also outlines the band edge of both conduction and valence band as well as the bandgap of these materials, in relation HER and OER potentials.

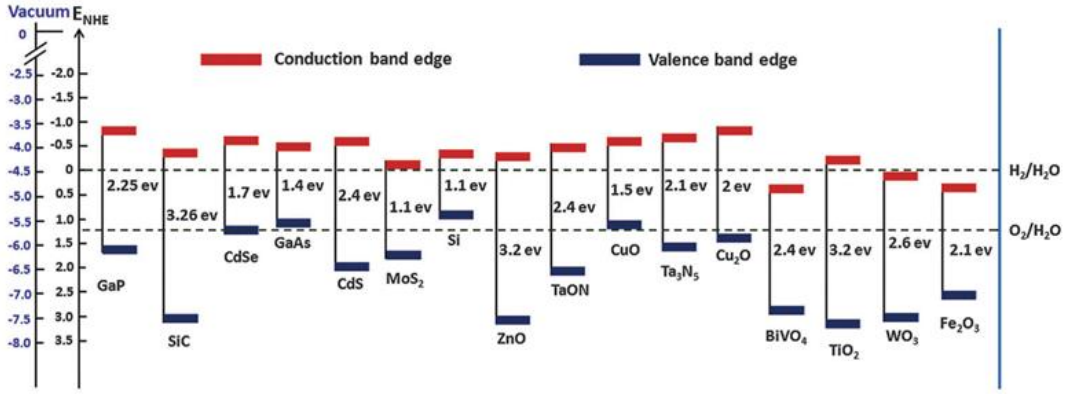


Figure 1.7: Some of the adequate materials for PEC cell incorporation. Reproduced from [111].

Analyzing figure 1.7, hematite (Fe_2O_3) does not have a suitable conduction band edge for driving hydrogen reduction but has a quite suitable conduction band (CB) edge for driving OER. As in hematite, according to this data, CuO does not have suitable valence band (VB) edge for driving OER but is suitable for driving HER. Furthermore, its low bandgap of $1.5\ \mathrm{eV}$ makes it unsuitable for water splitting in a traditional PEC cell, as outlined in section 1.2.

As a result, both hematite and CuO come with clear efficiency disadvantages for incorporation in a traditional PEC cell. However, for a tandem PEC cell, the lower bandgap of CuO makes it a very interesting material. Furthermore, both Hematite and CuO have suitable VB edge and CB edge, respectively, for driving water splitting in a tandem system like the one represented in figure 1.4.

1.2.3. Strategies for Enhancing Photoelectrochemical Performance

Over the years, many different photoelectrodes have been developed. Some of the most researched are α-Fe_2O_3, TiO_2, WO_3 [14,15,16,22] as photoanodes and, for instance, Cu_2O and CuO as photocathodes [22,24,25,26,33].

Some of this excellent photoelectrodes like TiO_2 or WO_3 have very wide bandgaps, imposing limitations on STH due to short absorption of the solar spectrum range – having low S-Q limits for STH conversion, ~1-2% and ~5-6% respectively [3,34]. Cuprous oxide

(Cu_2O) has achieved amazing results but is highly unstable in electrolytic environments and even at ambient air there are reports of degradation [27]. In the case of hematite (α-Fe_2O_3), it's very stable in alkaline environments and allows for a considerable theoretical STH efficiency of 16.8%, depending on its bandgap value which has been reported to be in the range 1.9-2.2 eV [14]. A problem with hematite, is that it has low mobilities for both electrons and holes ($\sim 10^{-2}\ \mathrm{cm^2 V^{-1} \cdot s^{-1}}$), or in equivalent ways: short mean free paths (2-4 nm for holes) or high effective masses [3,14,28]. This means that the generated charges are likely to recombine before getting to the surfaces where they should be collected. In summary, it is difficult to obtain a material that has adequate bandgap and electronic structure to promote water electrolysis, and that fulfils section 1.2.2 requirements. To improve overall PEC performance, many techniques can be employed:

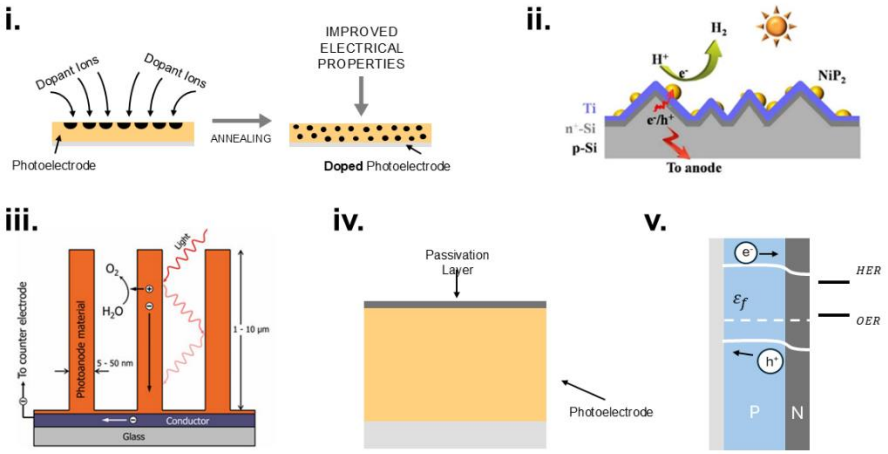


Figure 1.8: Illustration of various reported techniques for PEC improvement. **i. Doping. ii. Co-catalyst** NiP_2 deposited on a photoelectrode surface, above a Ti passivation layer. Adapted from [30]. **iii. Nanostructuring** example: nanowires. Adapted from [3]. **iv. Passivation Layer. v. p-n junction** photocathode with adequate band structure for water splitting.

i. **Doping**: doping can improve both the electronic transport properties and absorption of the material. Dopants can be donors (donate electrons, increase n carrier density) or acceptors (accept electrons, increase p carriers' density), providing a way to improve the electronic mobilities of the charge carries in the material [3,14,29]. Excess doping can lead to excess defects in the material that introduce the opposite effect, for which there is an optimal value for dopant concentrations [29].

ii. **Co-catalyst deposition**: photoelectrodes surfaces can be functionalized with co-catalysts such as Pt, TiO_2 or RuO_2 (either Hydrogen Evolution Catalysts HEC or Oxygen Evolution Catalysts OEC) to help create HER or OER active reaction sites, lower activation potentials, improving charge transfer between the electrode and electrolyte – It can also help with stability and faradaic efficiency

by enhancing selectivity [3,30]. They do not help with photoconversion, only with the reaction kinetics.

iii. **Nanostructuring**: Semiconductors can be nano-structured to help tune or improve their properties. For instance, nanotubes and nanowires offer wider surface area, and therefore wider active area for reactions to take place/charge to be collected and can offer shorter paths for charge carriers to reach the surface. Furthermore, the anisotropy introduced by the shapes and spatial confinement can further improve charge separation or even help tune the materials bandgap [3,14,28].

iv. **Passivation layers**: thin layers of materials like TiO_2, Al_2O_3 or ZrO_2 can help stabilize the photoelectrodes by improving better charge transport to the electrolyte and preventing the material from being in contact with the electrolyte itself [31].

v. **P-N junctions**: adding n-type layer to a photocathode or a p-type layer to a photoanode can further help charge separation because of the built-in electric field of these junctions, they can be achieved by doping the semiconductor material or by adding a different material, forming a heterojunction [32,]. The resulting electronic structure of the junction must still be capable of performing water electrolysis, which requires careful band matching of the materials and their fermi levels.

Table 1.2 summarizes results of some photoelectrodes, providing specifications of the techniques used as well.

Photoanodes	Employed Techniques	J @ V vs RHE	Source
α-Fe_2O_3	i. Sn Doped iii. Nanowires	$0.52\ \mathrm{mA \cdot cm^{-2}}$ @ $1.2\ \mathrm{V_{RHE}}$	[14]
α-Fe_2O_3	i. Mn Doped iii. Nanorods	$2.3\ \mathrm{mA \cdot cm^{-2}}$ @ $1.23\ \mathrm{V_{RHE}}$	[35]
WO_3	iii. Nanoplatelets	$1\ \mathrm{mA \cdot cm^{-2}}$ @ $1.23\ \mathrm{V_{RHE}}$	[15]
TiO_2	ii. NiOOH HEC iv. Al_2O_3	$1.42\ \mathrm{mA \cdot cm^{-2}}$ @ $1.23\ \mathrm{V_{RHE}}$	[37]
$BiVO_4$	ii. Ni-Co-LDH OEC	$3.4\ \mathrm{mA \cdot cm^{-2}}$ @ $1.23\ \mathrm{V_{RHE}}$	[36]
$BiVO_4$	ii. NiFe OER catalyst	$6.73\ \mathrm{mA \cdot cm^{-2}}$ @ $1.23\ \mathrm{V_{RHE}}$	[36]
Photocathodes			
Cu_2O	ii. RuO_2 HEC iv. TiO_2 passivation	$5.5\ \mathrm{mA \cdot cm^{-2}}$ @ $0\ \mathrm{V_{RHE}}$	[23]
Cu_2O	ii. Pt HEC	$3.55\ \mathrm{mA \cdot cm^{-2}}$ @ $0\ \mathrm{V_{RHE}}$	[41]
$CuBi_2O_2$	iii. Nanoclusters	$1.1\ \mathrm{mA \cdot cm^{-2}}$ @ $0\ \mathrm{V_{RHE}}$	[38]
CuO/ZnO	iii. Nanowires v. p-n heterojunction	$8.1\ \mathrm{mA \cdot cm^{-2}}$ @ $0\ \mathrm{V_{RHE}}$	[39]

Table 1.2: Summary of some literature results for photoelectrodes in PEC water splitting.

1.3. Cupric Oxide (CuO) Properties

Cupric Oxide (CuO) is one of three oxide phases of copper, the other two are Cu_2O and Cu_4O_3. During the beginning of this thesis development, numerical simulations (chapter 2) were conducted that motivated us to research CuO photocathodes for pairing with hematite. The key properties of this material relevant for its synthesis and photoelectrochemical splitting of the water molecule are presented throughout this chapter.

1.3.1. Structural Properties of Cupric Oxide

CuO is a ceramic material, with crystalline monoclinic structure belonging to the C2/c spatial group. Table 6 summarizes some of the structural properties of Cupper and its oxide phases.

Material	**Crystal System**	**Spatial Group**	$a = b = c$ (Å)			$\alpha = \beta = \gamma$ (º)	**Unit cell Volume** ($Å^3$)	**Density** g/cm^3	**Source**
Cu	Cubic	Fm-3m	3.615			90	47.2	8.96	[62]
Cu_2O	Cubic	Pn-3m	4.27			90	77.8	6.00	[63,64]
			$a = b$ (Å)		c (Å)				
Cu_4O_3	Tetragonal	I41/amd	5.837		9.932	90	338.4	6.47	[61,63]
			a	b	c	β			
CuO	Monoclinic	C2/c	4.68	3.42	5.13	99.3	81.3	6.31	[61,63]

Table 1.3: Crystallographic properties of Cupper and its oxide phases.

From all the oxide phases of the Cu-O binary system, CuO is the most stable, even more stable than copper (Cu) in oxygen environments at ambient conditions, as shown in the phase diagram of figure 1.9 (i).

These phase diagrams are exact in terms of phase stability, but other factors like the diffusion coefficient also play a role in the phase transition. Subsequently, at room temperature and ambient O_2 pressure, the ambient thermal energy is not enough to drive oxygen through the surface oxide layers. Consequently, copper oxides only form at higher temperatures, although they are more stable.

It is reported with aid of synchrotron x-ray analysis, that at 150ºC thermal energy is sufficient to overcome the native oxide layer on copper and further oxidize a batch of Cu films ranging from 100 to 1000 nm into Cu_2O [65].

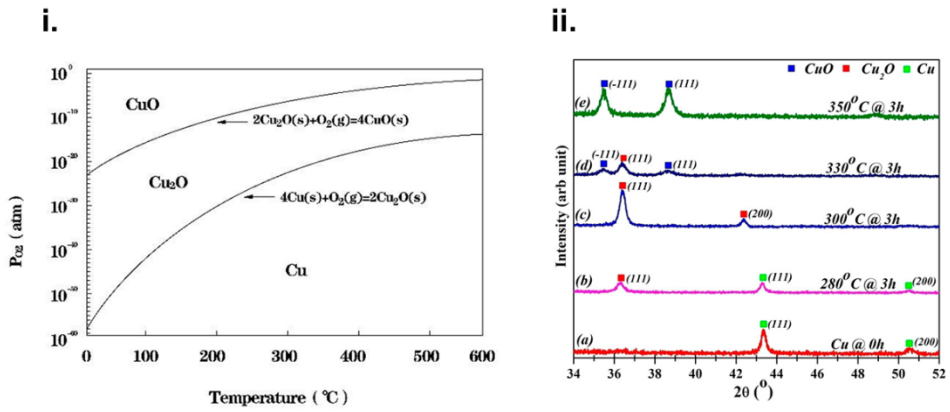


Figure 1.9: **i.** Phase Transition diagram for Cu-O binary system as function of O2 pressure and Temperature. Reproduced from [66] **ii.** Resume for x-ray spectrum for thin films Cu-O binary system, for various temperatures at 3h timestamp. Reproduced from [65].

Below 320ºC, the thermal energy is still not enough for enabling CuO phase transition, which is only detected above this temperature, as illustrated in figure 1.9 (ii). Table 1.4 summarizes some of the reported information, outlining the need time to achieve 100% oxide phase at different temperatures, which can be very helpful for synthesis purposes.

Phase / 100%	**Temperature (ºC)**				
	150	260	300	330	350
Cu_2O	unknown	18h	120min	-	-
CuO	-	-	-	20h	120min

Table 1.4: Time duration to achieve pure phase state at different temperatures. Data from [65].

This truly insightful work from Sumita Choudhary *et al*, shows that annealing the copper films in atmospheric air at 350ºC for 2h is enough to achieve pure CuO phase, as outlined in table 1.4. Another observed behavior during literature review is that the $Cu_2O \rightarrow CuO$ phase transition, is that the resulting CuO usually exhibits crystalline orientation in both Cu_2O's existing crystalline orientations, and their symmetric counterparts. In other words, if Cu_2O exhibits (111) crystalline orientation, CuO will exhibit both (111) and (-111). This is not observed in the Cu to Cu_2O phase transition and is most likely related with cubic symmetry conservation in the $Cu \rightarrow Cu_2O$ transition and a break in cubic to monoclinic symmetry in $Cu \rightarrow CuO$ transition. This tendency is visual in figure 1.9 (ii).

1.3.2. Optoelectronic Properties

The optoelectronic properties of a material are of the utmost importance in photoelectrochemical cells and photovoltaic devices in general. Cupric oxide, usually exhibiting p-type conductivity, although n-type has also been reported, has a reported tunable bandgap in the range 1.2-2.3 eV [70]. Although this bandgap malleability is

reported for CuO, some authors claim that it simply has an indirect bandgap of $1.23\ \mathrm{eV}$ and direct bandgap of $1.7\ \mathrm{eV}$ [3]. Some of the general optoelectronic properties of CuO are listed in table 1.5, as well for the well-known cuprous oxide (Cu_2O).

	CuO	**Cu_2O**	**Source**
Bandgap (eV)	1.2-2.3	2-2.27	[70]
Refractive index	1.4	2.28-2.14	[68][70]
Hole effective mass / m_e	0.24	0.4-5.6	[68][71]
Hole mobility / $\mathbf{cm^2V^{-1}}$	0.1-10	0.2-256	[68][69]
Maximum theoretical J_{photo} / $\mathbf{mA \cdot cm^{-2}}$	35	14.7	[68]

Table 1.5: Optoelectronic properties for CuO and Cu_2O found in literature.

The tunable property of cupric oxide (CuO) bandgap is attributed to quantum effects that rise when its electrons are spatially confined to nanometric dimensions lower than their de Broglie wavelength, as illustrated in figure 1.10. This confinement can be imposed by the crystallites, for which a clear inversely proportional relationship between nanoparticle/crystallite size and this material's bandgap has already been reported [72]. This inverse proportion relation is typical of these effects, as illustrated in figure 1.10 (ii).

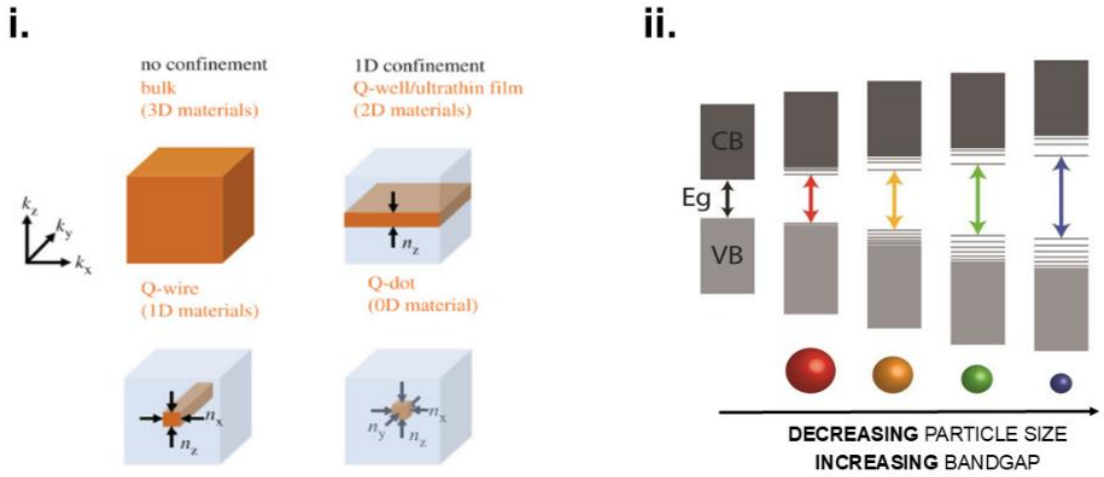


Figure 1.10: **i.** Illustration of different types of spatial confinement in k-space. Adapted from [112]. **ii.** Illustration on bandgap widening effect with particle size reduction. Adapted from [112].

Protocols and precursors utilized in synthesis, as well as oxygen flow rate during annealing have also been reported to influence bandgap value [76].

1.3.3. Photoelectrochemical Properties

This material has a monoclinic structure, as outlined in section 1.3.1, which is a highly anisotropic symmetry. This anisotropy affects several properties of CuO, also having an impact on its photoelectrochemical properties [113]. In a performed DFT study, in which bandgap center determination is exact, CuO is found to have different bandgap centers for different crystalline orientations [113]. Considering a bandgap of $1.5\ \mathrm{eV}$, this study shows that the (111) direction and (011) are the most suitable for water splitting because they result in suitable band edges [113].

Usually exhibiting onset potentials between 0.7 and 0.8, some excellent CuO photocathodes have been reported [39], already reaching amazing photocurrent densities of 8.1 $\mathrm{mA \cdot cm^{-2}}$, as listed for the ZnO passivated CuO photocathode in table 1.2. Figure 1.11 showcases reported j-V characteristics.

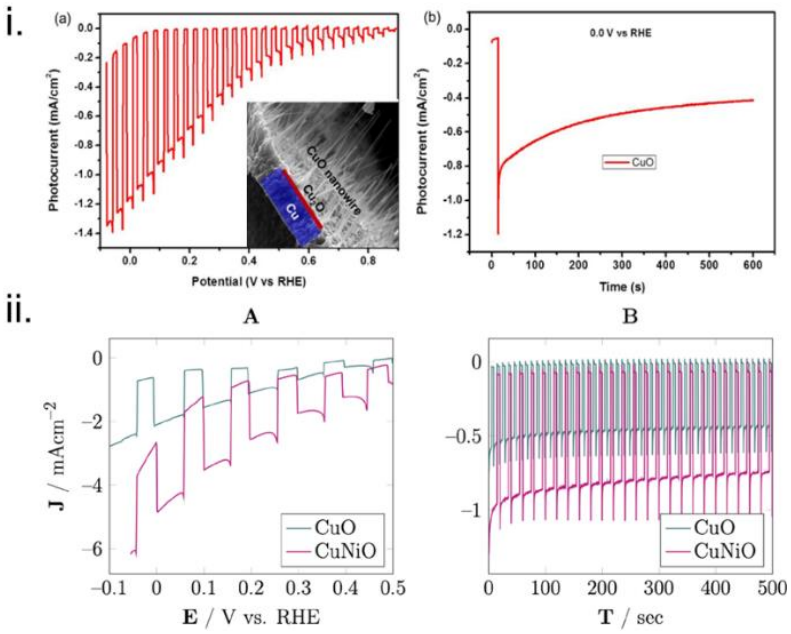


Figure 1.11: **i.** (a) J-V curves with chopped illumination for CuO nanowires with Pt co-catalyst (b) J-t under illumination for 10 min. Reproduced from [115] **ii.** A. J-V curves with chopped illumination. B. J-t for chopped illumination during 8min @ 0.3 V vs RHE. Reproduced from [116].

Perhaps one of the most concerning photoelectrochemical characteristics of CuO is that it can go through self-induced reduction, making long-term stability a challenge and topic of active research [40]. Strategies like increasing the surface area and other techniques, that protect the surface and enhance charge transfer dynamics with the electrolyte (approaches ii, iii, and iv from section 1.2.3), are suitable routes for both stabilizing this material during PEC operation and performance enhancement purposes [40].

2. Numerical Modelling of Photoconversion for Solar-to-Hydrogen Efficiency

In tandem photovoltaic devices, bandgap pairing is one of the most important properties and has a great impact on the converted solar energy, as outlined in section 1.2.1. As such, having the capability to calculate theoretical maximum efficiencies based on bandgap pairing emerges as a highly useful tool when constructing a tandem PEC cell, enabling the selection of key material combinations based on their bandgap. An algorithm capable of doing this calculation could also be used for comparing expected efficiencies with real efficiencies in tandem devices: so, if a synthesis does not output the expected bandgap, the amount of loss because of bandgap mismatch may be estimated.

With the goal to study and identify suitable bandgap pairings that maximize STH efficiency for existing photoanodes but also to investigate unreported material combinations and devices configurations, numerical simulations were conducted. These simulations were conducted using the Detailed Balance Limit model (also known as Shockley-Queisser (S-Q) limit), explained throughout sections 2.1.1 and 2.1.2. To account for losses in photoconversion, abstract factors and functions are introduced in section 2.1.3, as a way of simulating deficits in open circuit voltage (V_{OC}) and short circuit current (J_{SC}). The implemented numerical methods for solving critical equations of the model are detailed in section 2.2. Subsequentially, model implementation and respective results are outlined in section 2.3. All functions and methods are implemented in python and can be consulted in appendix.

2.1. Shockley-Queisser (S-Q) limit formalism

Firstly proposed by William Shokley and Hans-Joacquin Queisser in 1961, the S-Q limit is the maximum theoretical efficiency for a p-n junction solar cell under ideal conditions. This model has four fundamental assumptions [74]:

1. The only recombination mechanism is radiative recombination.
2. The absorption and emission are in thermodynamic equilibrium, so emission is given by black body emission derived from Bose-Einstein statistics.
3. Every photon above the bandgap is absorbed and contributes to current, translating into a quantum efficiency (QE) of 100% for photons above the bandgap.
4. Excess energy from the photons is lost as heat.

Because of these ideal assumptions the S-Q limit is actually a physical limit that you may approach, but never actually achieve, outputting a maximum efficiency of around 32% for 1.1 eV bandgap, while commercial 1.1 eV silicon cells efficiency is around 24% due to reflection losses and other non-ideal scenarios [105]. Sections 2.1.1 and 2.1.2 introduce the model for single and multi-junction cells, while section 2.1.3 introduces the implemented factors for loss incorporation in the calculation.

2.1.1. S-Q limit for Single p-n Junctions

The previously listed assumptions enable the derivation of suitable relationships for calculation of maximum theoretical efficiency for a given incident light spectrum in a p-n junction. Because of assumption (3), the number of generated charge carriers' density per unit time (G) is given by [74]:

$$G = \int_{E_g}^{\infty} \phi(E)\, dE \tag{2.1}$$

Where $\phi(E)$ is the incident photon spectral flux ($\#\text{photons} \cdot \text{m}^{-2} \cdot \text{eV}^{-1} \cdot \text{s}^{-1}$), which may be obtained by dividing the incident irradiance ($\text{W} \cdot \text{m}^{-2} \cdot \text{eV}^{-1}$) by the photon's energy $E = \frac{hc}{\lambda}$. The bandgap is denoted by the symbol E_g. In other words, $\phi(E)dE$ represents the number of photons with energies lying between E and $E + dE$.

Because of assumptions (1) and (2), the number of photons emitted by the junction is given by integrating Bose-Einstein black-body emission statistics for $V = 0$ [74]:

$$Q_c = \frac{2\pi}{c^2 h^3} \int_{E_g}^{\infty} \frac{E^2}{\exp\left(\frac{E - qV}{V_T}\right) - 1} dE \tag{2.2}$$

Where q is the electric charge, V is the potential difference across the junction and $V_T = \frac{k_B T}{q}$ is the thermal voltage. This expression has no analytical solution, so numerical methods must be employed. In this way, the short current density may be calculated by expression 2.3:

$$J_{SC} = q(G - Q_c) \tag{2.3}$$

The total photocurrent density (J_{photo}) is calculated by subtracting the dark diode current density (J_{rec}), to the generated short current density:

$$J_{photo} = J_{SC} - J_{rec}$$
$$J_{photo} = J_{SC} - J_0 \cdot e^{\frac{V}{V_T}} \tag{2.4}$$

Where $J_0 = qQ_c$ is the recombination amplitude of the junction, V is the junction's potential difference and $V_T = \frac{k_B T}{q}$ is the thermal voltage [74]. Equation 2.4 allows for determining the J_{photo}-V charactheristics of a p-n junction with bandgap E_g at a temperature T.

The open circuit voltage may be determined by setting $J_{photo} = 0$:

$$V_{OC} = V_T \cdot \ln\left(\frac{J_{SC}}{J_0}\right) \quad (2.5)$$

Knowing the open circuit voltage of the system, the voltage range is determined ($V \in [0, V_{OC}]$), and the maximum power point (MPP) of the device may be determined numerically [74]:

$$MPP = Max(J_{photo} \cdot V) \quad (2.6)$$

2.1.2. S-Q limit for Multi-junction (Tandem) Cells

In the case of a n-junction cell, the process is very similar. Through this analysis it is consider that the junctions positioning is in decreasing bandgap order in relation to light incision direction. The generated charge carrier's density on the i^{th} absorber is:

$$G_1 = \int_{E_{g,1}}^{\infty} \phi(E)\, dE \quad (2.7) \qquad G_i = \int_{E_{g,i}}^{E_{g,i-1}} \phi(E)\, dE \quad (2.8)$$

With $i \in \{2, .., n\}$. In the case of two junctions:

$$G_2 = \int_{E_{g,2}}^{E_{g,1}} \phi(E)\, dE \quad (2.9)$$

In case of series connection between junctions, the junction with lowest J_{SC} limits the short current density of the device. Each individual $J_{SC,i}$ is calculated according to equation 2.3, and the lowest one becomes the J_{SC} of the cell:

$$J_{SC} = Min[J_{SC,1}, J_{SC,2}, \dots, J_{SC,n}] \quad (2.10)$$

With J_{SC} determined, the current density range is now known: $J_{photo} \in [0, J_{SC}]$. Relationship 2.4 can be inverted to output the voltage of the i^{th} junction (V_i), as a function of the photocurrent density J_{photo}:

$$V_i = V_T \cdot \ln\left(\frac{J_{SC} - J_{photo}}{J_{0,i}}\right) \quad (2.11)$$

The voltage across the cell for series connection is given by equation 2.12:

$$V_{\text{cell}} = \sum_i V_{\text{T}} \cdot \ln\left(\frac{J_{\text{SC}} - J_{\text{photo}}}{J_{0,\text{i}}}\right) \quad (2.12)$$

Like in section 2.1.1, the MPP can be determined numerically:

$$\text{MPP} = \text{Max}\left(J_{\text{photo}} \cdot V_{\text{cell}}\right) \quad (2.13)$$

2.1.3. Photoconversion Losses Implementation

As outlined in section 2.1, the S-Q limit calculation is derived under ideal scenarios such as 100% quantum efficiency (QE) (assumption 3) and only radiative recombination (assumption 1). However, in practical situations, additional recombination pathways such as Auger, defect induced recombination or unbalanced doping, that introduce significant losses in both J_{SC} and V_{OC}, also arise. To account for these losses, a term that controls recombination current amplitude and a function that introduces loss in quantum efficiency (QE) are implemented, enabling the simulation of V_{OC} and J_{SC} deficits with traceable physical behaviors.

V_{OC} Deficit

For accounting V_{OC} deficits, an f_{c} term that controls the recombination current density amplitude (J_0) is introduced. This extra recombination should be proportional to the $e^{V/V_{\text{T}}}$ factor, justifying the amplitude control implementation. In this work, this is done in a different but equivalent way to reported literature [75]. Relations 2.14 and 2.15 outline the adaptations to expressions 2.4 and 2.5:

$$J_{\text{photo}} = J_{\text{SC}} - \frac{J_0}{f_{\text{c}}} \cdot e^{\frac{V}{V_{\text{T}}}} \quad (2.14) \qquad V = V_{\text{T}} \cdot \ln\left(f_{\text{c}} \cdot \frac{J_{\text{SC}} - J_{\text{photo}}}{J_0}\right) \quad (2.15)$$

So, if $f_{\text{c}} = 1$ its equivalent to detailed balance limit and if $f_{\text{c}} < 1$ recombination increases with a voltage dependency, affecting open circuit voltage. This factor was found to simulate rather well V_{OC} deficits but did not affect J_{SC} effectively.

J_{SC} Deficit

To account for both absorbance and quantum efficiencies losses, a QE efficiency function is modulated by hyperbolic tangents:

$$QE(E) = \begin{cases} 0 & , E < E_{\text{g}} \\ A \cdot \tanh\left(B \cdot \left(E - E_{\text{g}}\right)\right) & , E \geq E_{\text{g}} \end{cases} \quad (2.16)$$

Where A and B are parameters that may introduce different loss, although $B = 5$ is held fixed throughout this analysis. The factor $A \in [0,1]$ controls the amplitude of $QE(E)$, while B controls "how fast" $QE(E)$ goes from 0 to A (see figure 2.1).

This function is incorporated in the generated charge carrier's calculation, in a way that expression 2.1 becomes:

$$G = \int_{E_g}^{\infty} \phi(E) \cdot QE(E)\, dE \qquad (2.17)$$

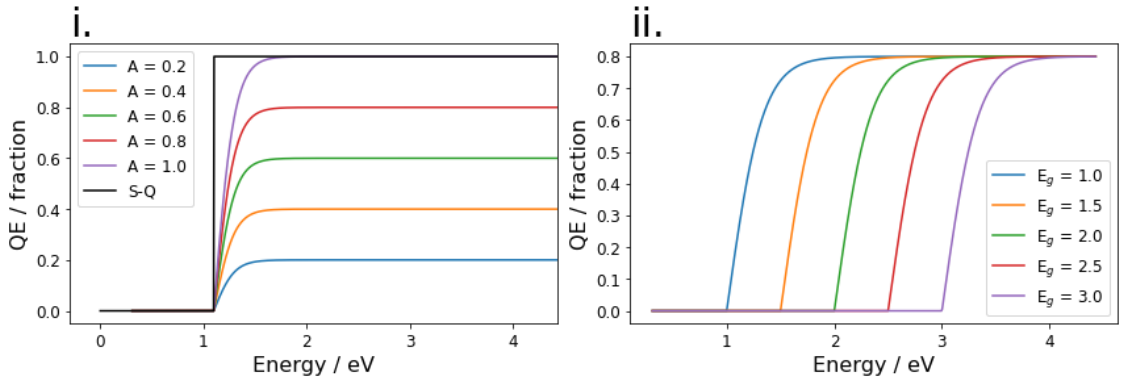


Figure 2.1: **i.** Graphical representation of the QE assumed in S-Q limit vs the simulated profile by expression 2.17, for $A \in [0.2,1]$, $B = 5$ and $E_{gap} = 1.1\ eV$. **ii.** Graphical representation of simulated QE by expression 2.15 as function of bandgap, for $A = 0.8$ and $B = 3$.

The $QE(A,E)$ function represents the fraction of incident photons with energy E that are absorbed and contribute to the generated current density, resembling the behaviour of absorbance spectrums, as illustrated in figure 2.1. With this approach, we were able to successfully introduce J_{SC} deficits.

2.2. Numerical Methods

This section outlines the employed numerical methods for calculation of the S-Q limit, used in the calculation of equations 2.1 and 2.2, as well in the determination of the maximum power point (MPP).

All functions are implemented in python, and the different systems are modelled by imposing adequate mathematical restrictions. The only numerical techniques used are for integration and maximum search. All wavelength dependent variables are converted to energy variables through $E = \frac{hc}{\lambda}$ relation.

2.2.1. Trapezoidal Rule

The trapezoidal rule is employed for numerical integration of the equation 2.1 (G) .The incident photon spectral flux (G) is calculated using the reference spectrum ASTM G173-03, corresponding to 1 Sun Air Mass 1.5, obtained from ENRL data Files [108]. Trapezoidal rule consists in discretizing a continuous function $f(x)$ and its integration domain in N small intervals with width h. If the integration domain is $x \epsilon [a, b]$, h is given by:

$$h = \frac{b-a}{N} \tag{2.18}$$

Then the integration simply becomes the sum of the various trapezoids defined by width h and heights $f(a+kh)$ and $f(a+(k+1)h)$, with $k \epsilon \{0,1,2,..,N-1\}$:

$$I = \int_a^b F(x)dx \longrightarrow \sum_{k=0}^{N-1} h \frac{F(a+k\cdot h) + F(a+(k+1)h)}{2}$$

$$I = \frac{h}{2}\left(f(a) + f(b) + 2\sum_{i=1}^{N-1} f(a+k\cdot h)\right) \tag{2.19}$$

The uncertainty of this method is in the order of magnitude of h [106]. For details in this implementation of the rule, see appendix.

2.2.2. Gauss-Legendre Quadrature

For integrating expression 2.2, Gauss-Legendre quadrature is used. Gauss-Legendre quadrature, a variant of Gaussian quadrature, allows for fast and precise numerical integration by using non-uniform nodes and optimized weights for integrals of the form [106]:

$$I = \int_{-1}^{1} f(x)dx \approx \sum_{i=1}^{n} w_i f(x_i) \tag{2.20}$$

Where x_i are the nodes, w_i are the integration weights of the nodes and n is the number of sampled nodes used for integration. This method allows for exact integration of any polynomial up to order $2n-1$.

First the integration domain is changed from $E \in [E_g, \infty]$, into a finite domain $z \epsilon [-1,1]$, with the following change in variables:

$$E = \frac{2E_g}{1-z} \quad (2.21) \qquad dE = \frac{2E_g}{(1-z)^2}dz \quad (2.22)$$

With a quick inspection it's simple to confirm the variable change outputs the right integration limits:

$$\lim_{z\to -1}\frac{2E_g}{1-z} - = E_g \quad (2.23) \qquad \lim_{z\to 1}\frac{2E_g}{1-z} = \infty \quad (2.24)$$

The new expression for Q_c under thermodynamic equilibrium ($V = 0$):

$$Q_c = \frac{16\pi {E_g}^3}{c^2h^3}\int_{-1}^{1}\frac{1}{\exp\left(\frac{2E_g}{V_T}\frac{1}{1-z}\right)-1}\cdot\frac{dz}{(1-z)^4} \quad (2.25)$$

The later expression is integrated using Gauss-Legendre quadrature for $z\,\epsilon\,[-1,1]$, being a function of E_g and the cells temperature.

2.2.3. Numerical Maximum Search

The numerical method employed for maximum search is unconventional and takes advantage of built-in python functions. The employed methods were chosen because they allow extracting the maximum element of a numeric array, allowing to determine the maximums from the arrays used in graphical representation the efficiencies as a function of bandgap/bandgap pairing.

Single Domain Functions

NumPy allows for identification of the index of the maximum value of a given array by the "np.argmax()" function, which was used to determinate all maximums:

1. The functions domain $[a, b]$ is computed and represented as an array x. This domain is an array with discrete elements, equally spaced by an amount δ. This spacing is user defined in the creation of the domain array: $x = (a, a+\delta, a+2\delta, \dots, b-\delta, b)$;
2. The output function $f(x)$ is computed for all elements in x, and stored in an array $y = f(x)$. By running the instruction "np.argmax(y)", the index "i" of the maximum value in y is outputted.
3. The index of maximum value in y is the same of the element in array x that outputted that value. By running the instruction "$x[i]$", the value of the domain at which $f(x)$ is maximum is known, by an uncertainty of δ: $x_{\max} = x[i] \pm \delta$.

This method enables fast maximum determination, within an user defined uncertainty of δ.

Multidomain functions

1. For multidomain functions the various domains of integration are computed and stored in their own array: $d_1, d_2, \dots, d_n$.
2. The output function is computed for all possible combinations of the elements in the various domains $d_1, d_2, \dots, d_n$: $f(d_{1,i},\ d_{2,j}, \dots,\ d_{n,k})$, and represented in an array $y = f(d_1,\ d_2, \dots,\ d_n)$
3. Then in a similar fashion to the 1D method, the "np.argmax(y)" outputting the index "i" of the maximum argument on the uravelled y array (each vector inside the array is sequentially mapped into a 1-dimensional array). Following this, in the case of 2D "y" arrays, it is possible to retrieve the 2D maximum indexes by the following operation: $d_{1,\max} = \operatorname{int}\left(\frac{i}{\operatorname{length}(d_1)}\right), d_{2,\max} = i - \operatorname{length}(d_1) \cdot d_{1,\max}$.

2.3. Model Implementation and Results

This section explains how the models are implemented and outlines the obtained results, focusing on possible STH efficiencies under different photoconversion losses and device configurations.

2.3.1. Single Junction limit and Loss Factors Implementation

For calculating the S-Q limit of a single p-n junction, equation 2.1 (G) and 2.2 (Q_c) are calculated using the numerical methods described in sections 2.2.1 and 2.2.2, as function of E_g and considering room temperature $T = 300\text{K}$. A study on equation 2.25 integration convergence points was carried, considering the percentual difference between successive integrations $\Delta E = \frac{I_n - I_{n-1}}{I_{n-1}} \times 100$ as criterium, where I_n is the integration value for n sample points. The method demonstrates fast convergence, as outlined in figure 2.2. The study showed that 30 sample points are enough to achieve a good convergence of $\Delta E < 10^{-10}$, for $E_g \in [0.4, 3]$ eV. For this reason, all integrations of equation 2.24 are carried using 30 sample points.

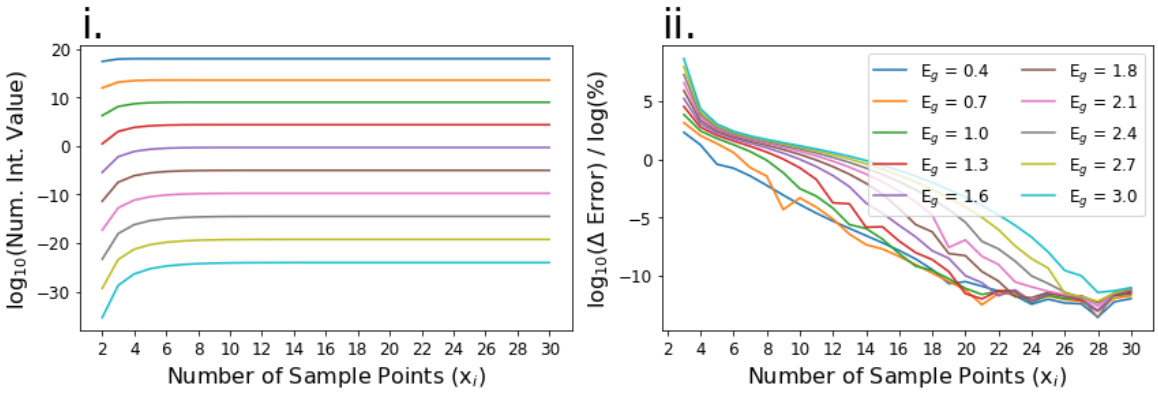


Figure 2.2: **i.** Logarithm value of the numerical integration value, as a function of the sample points. **ii.** Logarithm of percentual error difference between successive integrals for various bandgaps for $E_g \in [0.4,3]$ eV. Formula: $\Delta E = \frac{I_n - I_{n-1}}{I_{n-1}} \times 100$.

After this, equation 2.4 is implemented as a function of J_{SC} and V. Subsequently, open circuit voltage is calculated using relation 2.5, enabling the creation of a numeric array ranging from 0 to V_{OC} in steps of δ:

$$V = [0, \delta, 2\delta, \dots, V_{\mathrm{OC}} - \delta, V_{\mathrm{OC}}] \qquad (2.26)$$

Finally, the maximum power point (MPP) is determined using the described method for maximum search in section 2.2.3 for single domain functions. The loss factors are inserted by considering relations 2.14, 2.15 and 2.17 in the J_{photo}, V_{OC} and G calculation.

V_{OC} Deficit

Open circuit voltage deficit is introduced by the factor f_c as described in section 2.1.3, changing current density and voltage relations, according to equations 2.14 and 2.15.

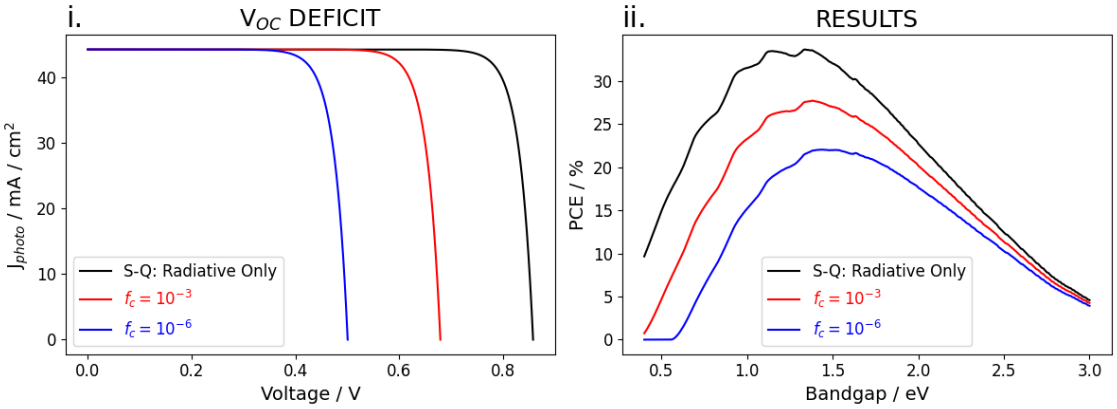


Figure 2.3: **i.** S-Q limit as a function of bandgap for: $f_c = 1$ (only radiative recombination) and $f_c = 10^{-3}, 10^{-6}$ (a thousand and million-fold more recombination than radiative). **ii.** J-V profiles for 1.1 eV Si considering the same f_c factors as in (i).

These results approach the published literature by this method [75]. As we can see, the f_c term simulates rather well V_{oc} deficits but doesn't affect J_{SC} in a significant way, not impacting wider bandgap values as much as lower ones, as figure 2.3 (i) shows. Photoelectrochemical cells usually take advantage of wide bandgap materials for their high operating voltages and STH efficiency strongly depends on J_{photo}. Subsequently. considering only the f_c factor will not affect these important bandgap range as much as the lower ones, promoting an unfair loss implementation.

J_{SC} Deficit

By introducing the $QE(E)$ function in the G term calculation (equation 2.17), it is possible to introduce short circuit current density deficit as well, as illustrated in figure 2.4. As the results show, this approach successfully simulates J_{SC} deficits, also having a more homogeneous impact across the considered bandgap range as well, as it can be visually confirmed by inspection of figures 2.3 (ii) and 2.4 (ii). To the best of our knowledge, this approach is not reported in literature.

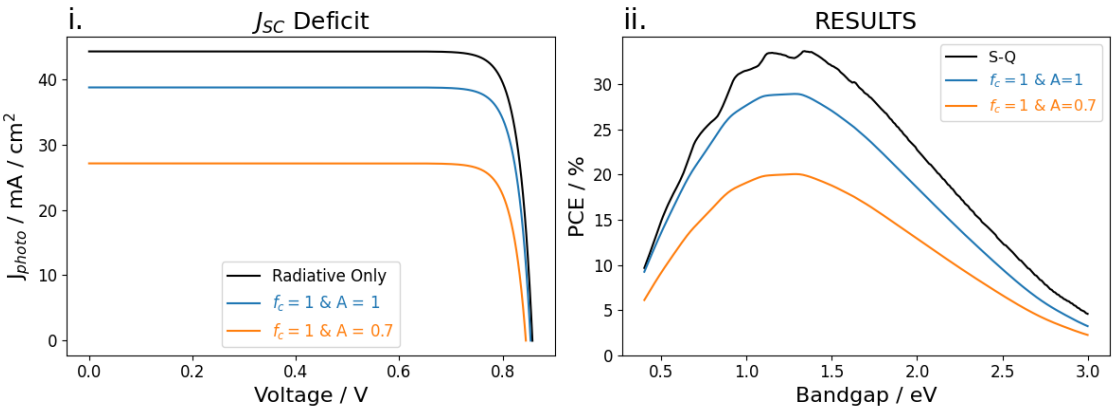


Figure 2.4: **i.** Implemented model with simulated QE losses, for $B = 5$ according to expression 2.13. **ii.** Visualization of the losses impact on J-V behavior for 1.1 eV Si.

The observed decrease in efficiencies (plot ii.), demonstrates how much a small deviation from ideal 100% quantum efficiency can impact the S-Q limit, decreasing maximum of 1.1 eV Si PCE (Percentage of Converted Energy) from 32.9% to 28.7 % considering $f_c = 1$, $A = 1$ and $B = 5$.

Adapted Model

Implementing both the f_c factor and the $QE(E)$ function, both V_{OC} and J_{SC} deficits can be incorporated. Comparing the previous models (figures 2.3 and 2.4) with the adapted model in figure 2.5, the adapted model is more complete, as it allows us to simulate losses in both J_{SC} and V_{OC}. With these adaptations, evaluating the S-Q limit under different photoconversion losses considerations is now possible.

Besides the successful loss implementation, these loss factors can be traceable to real physical behaviors: for instance, the introduced $QE(E)$ function may be thought as the result of absorbance and collection efficiency of the material for photons with energy E, while f_c is a suitable pathway to introduce non-radiative recombination.

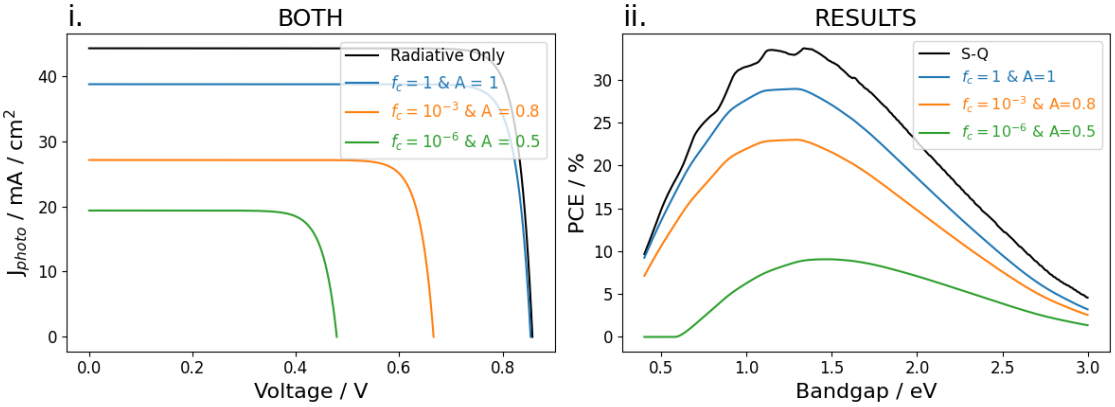


Figure 2.5: **i.** J_{photo}-V characteristics with varying loss factor: $A \in \{1, 0.7, 0.5\}$, $f_c \in \{1, 10^{-3}, 10^{-6}\}$. **ii.** Loss factors impact in energy conversion.

2.3.2. Double Junction S-Q limit for STH conversion

Following the successful implementation of the S-Q limit calculation for a single junction, it is possible to extrapolate the model for a multi-junction system, as described in section 2.1.2. Firstly, the S-Q limit for a 2-junction system connected in series is implemented, following section 2.3.1 reasoning. In relation to the single junction calculation, there are some extra steps:

1. The G_2 factor is calculated according to equation 2.9, with the nuance that the spectral photon flux (G) is simply set to be 0, for photons satisfying: $E \geq E_{g,1}$; instead of changing the integration limits.
2. Both $J_{SC,1}$ and $J_{SC,2}$ are determined, maintaining the lowest one as the device's J_{SC}, as represented in equation 2.10 from section 2.1.2.

3. The voltage of the cell (V_{cell}) is calculated with relation 2.12, and the MPP is determined using the maximum search for single domains described in section 2.2.3.
4. Finally, the maximum search for multi-domain functions is employed to find the maximum PCE as function of $E_{\text{g},1}$ and $E_{\text{g},2}$.

For photoconversion loss incorporation, the expressions 2.14, 2.15 and 2.17 are introduced (section 2.3.1). When f_{c} and A factors are considered, they are the same for both junctions. For solar-to-hydrogen (STH) conversion it is assumed that the cell's photoelectrodes (cathode and anode) have suitable band edges for water splitting, so if the condition:

$$V_{\text{cell}} > V_{\text{act}} \qquad (2.27)$$

Is verified, the reaction should happen. Where V_{act} is the redox potential for water splitting, including activation losses. The equivalent electrochemical circuit for regions satisfying condition 2.27 is illustrated in figure 2.6.

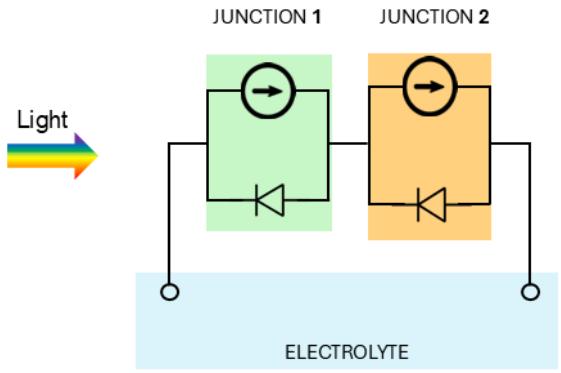


Figure 2.6: Equivalent circuit of a 2-junction tandem PEC.

For STH S-Q limit calculation in unbiased regions, expression 1.8 is used for efficiency. Where the hydrogen flux is obtained by considering the current density at the maximum power point (J_{MPP}):

$$\phi_{\text{H}_2} = \frac{J_{\text{MPP}}}{2qN_{\text{A}}} \qquad (2.28)$$

Another reasoning could be applied, for instance, the current density could be taken at $V_{\text{cell}} = 1.23\ \text{V}$ (or at another reaction redox activation potential), because lower voltages usually lead to higher photocurrents, as it can be quickly confirmed by inspection of figures 2.3, 2.4 and 2.5 (i). However, the MPP is a stable operation point of the cell and

considering the current density at this point promotes a more conservative analysis, as in practice the S-Q limit could be higher than the ones presented.

Results

The traditional S-Q limit calculation, applied to 2-junction system for STH conversion, is presented in figure 2.7. The null STH efficiency zone on the left of both plots is a region where the second junction has a higher bandgap than the first one, having null incident spectral photon flux. The right null zone is related with activation losses.

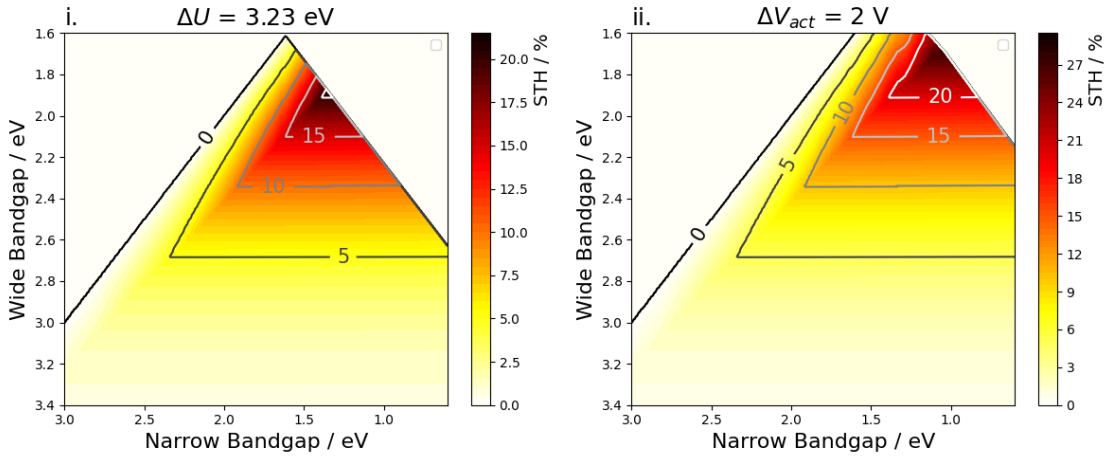


Figure 2.7: **i.** Literature reproduction considering $\Delta U = 3.23\ eV$ [17]. **ii.** S-Q for STH efficiency considering $\Delta V_{\mathrm{act}} = 2V$.

Likewise, the null STH region to the right of both plots is related to activation losses:

i. Plot (i), previously achieved in literature [17], which considers an activation loss of 1 eV on the junctions' bandgaps: $\Delta U = E_{\mathrm{redox}} + 2\ \mathrm{eV}$.
ii. Plot (ii), unlike the previous approach, considers a reaction activation potential of $V_{\mathrm{act}} = 2\ \mathrm{V}$. In this approach, the operating voltage V_{MPP} must obey condition 2.27.

The considered $V_{\mathrm{act}} = 2\ \mathrm{V}$ already contains big activation potentials. However, even with this loss, STH efficiencies as high as 27% are permitted by the S-Q limit. Table 2.1 outlines the maximum STH bandgap pairings for each calculation.

	E_1 / eV	E_2 / eV	STH / %	Source
i. This work	1.33	1.87	21.2	-
Literature	1.34	1.89	21.6	[17]
ii. $\Delta V_{\mathrm{act}} = 2$ V	1.05	1.69	27.4	-

Table 2.1: Results and literature comparison for maximum STH conversion using S-Q limit model.

According to results of calculation (ii), maximum STH efficiencies over 20% are possible by some combinations of $E_{g1} \in [1.6, 1.9]\,\mathrm{eV}$ and $E_{g2} \in [1, 1.5]\,\mathrm{eV}$, which can be observed inside the white contour line in figure 23 (ii).

Hematite as a reported bandgap in the range $[1.9, 2.2]$ and CuO has a reported tuneable bandgap in the range $[1.2, 2]$ eV. Cupric oxide (CuO), being one of the transition metal oxides with reported bandgap below 1.7eV, could serve as a narrow bandgap semiconductor, but also as a wide bandgap material due to its reported tunable bandgap. In this way, both combinations Fe_2O_3-CuO and CuO-Si bandgap pairings are studied, with photoconversion losses incorporation.

Hematite-CuO Pairing

To study Hematite-CuO pairing, STH is calculated for these materials' possible bandgap combinations. Loss factors are varied to evaluate the impact of photoconversion losses in STH efficiency, as represented in figure 2.8.

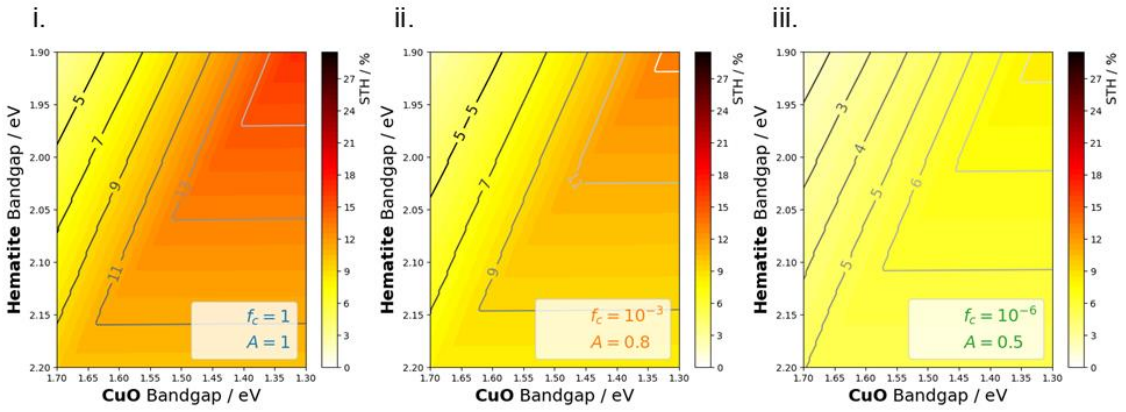


Figure 2.8: STH efficiency simulations for Hematite-CuO bandgap pairing. i. $f_c = 1, A = 1$ & $B = 5$. ii. $f_c = 10^{-3}$, $A = 0.8$ & $B = 5$. iii. $f_c = 10^{-6}, A = 0.5$, $B = 5$.

		Minimum Pairing			Maximum Pairing		
Plot	$[f_c, A]$	E_{g1} / eV	E_{g2} / eV	**STH / %**	E_{g1} / eV	E_{g2} / eV	**STH / %**
i	$[1, 1]$	1.7	1.9	2.8	1.31	1.9	16.7
ii	$[10^{-3}, 0.8]$			2.3			13.4
iii	$[10^{-6}, 0.5]$			1.42			8.4

Table 2.2: Results for the Hematite-CuO pairing. **i.** Approaching S-Q limit conditions; **ii.** x10^3 more recombination with QE plateau at 0.8. **iii.** A million-fold more recombination, with QE plateau at 0.5.

These results show that for the considered bandgap ranges, STH can vary a lot depending on the pairing. The minimum STH pairing is always for 1.7 eV CuO and 2.2

eV Hematite, always below 3% even for low photoconversion losses. On the other hand, the maximum is always for 1.9 eV Hematite and 1.31 eV CuO. Approaching ideal photoconversion conditions, promising STH efficiencies as high as 16.7% should be possible, which can be lowered to around 8.4% with considerable photoconversion losses.

CuO-Si Pairing

Inspecting figure 2.7 (ii), combining CuO-Si might enable enhanced STH efficiency regarding Hematite-CuO combination. Under this scenario, CuO is considered the wide bandgap material and Si the narrow one: Si could be integrated with as a PV Pannel or passivated with an electrocatalyst layer for direct contact with the electrolyte.

Based on results, a 1.75 eV CuO could be a perfect match for 1.1eV Si – having above 10% STH efficiency, even for high photoconversion losses, as figure 2.9 demonstrates, and efficiencies as high as 21% for low photoconversion losses.

Interesting that after introducing $QE(E)$ function, the optimal bandgap of CuO shifts slightly to the right and maintains constant.

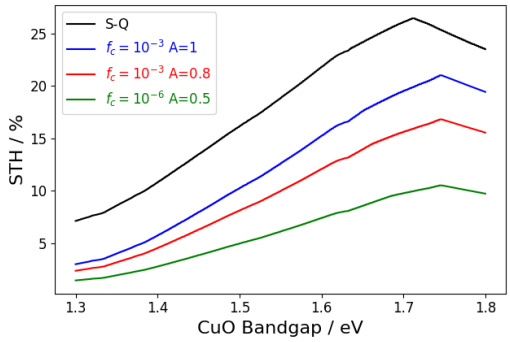


Figure 2.9: Graphical representation of STH as function of wide bandgap value for 1.1 eV Si.

$[f_c, A]$	$E_{g,max,CuO}$ / eV	STH_{min} / %	STH_{max} / %
S-Q	1.71	7.11	26.7
$[10^{-3}, 1]$	1.75	2.97	21
$[10^{-3}, 0.8]$	1.75	2.3	16.8
$[10^{-6}, 0.5]$	1.75	1.4	10.5

Table 2.3: Results for CuO-Si pairing. All minimum STH are for $E_{g,1}$ = 1.3 eV.

This shift in the bandgap that maximizes STH efficiency, is most likely related to the fact the introduced $QE(E)$ function makes the first photons above bandgap contribute less, as can be visually perceived in figure 2.1 (i). These results indicate that based on bandgap, CuO is a material with great interest for incorporation in a tandem PEC cell.

2.3.3. Breaking the S-Q limit for in series 3-junctions Cells

This section comprises a mini study in 3-junction tandem PEC devices using the normal S-Q limit. Firstly, the traditional in series connection of the 3-junctions is evaluated, outputting similar conclusions to those reported in literature [3]. However, by changing the electrical connections there is a gain in relation to 2-junction devices, as shown in this section.

Maximum STH limit for a 3-junction tandem PEC cell

As it is not possible to visualize a $\mathrm{STH}(E_{g1}, E_{g2}, E_{g3})$ function (4-dimensional space, 3 input variables into 1 output), the maximum STH is calculated based on E_{g3} (3rd junction bandgap) variation for fixed domains in E_{g1}, E_{g2}.

In practice, a 3rd junction is included in series in section's 2.3.2 algorithm. Subsequentially, STH efficiency is calculated for $E_{g1} \in [1.4,3]$ and $E_{g2} \in [1.3,2]$ and represented as function of E_{g3}.

Inspecting figure 2.10 (i), the maximum STH efficiency is a 21.21 % plateau for narrow bandgap range of $E_{g3} \in [0.6, 0.8]$ eV, imposing the need for rather low bandgap materials and increasing costs, but with no gain in efficiency. This plateau is related with the limitation on the spectral photon flux of the 2nd junction. Figure 2.10 (i) also details that maximum STH follows the remaining incident photon flux tendency (G_3 factor), as outlined by the blue curve in plot (i).

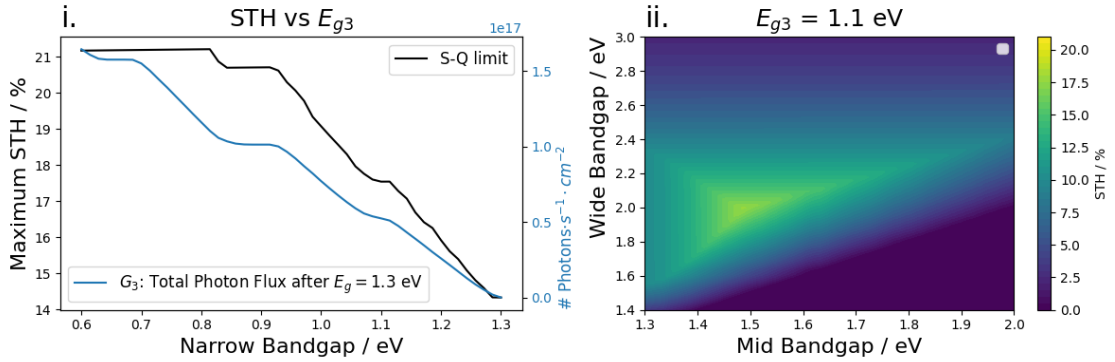


Figure 2.10: **i.** Maximum STH efficiency as a function of the bottom junction bandgap value. **ii.** Maximum STH efficiency for wide and mid bandgap pairings, for a fixed 1.1 eV narrow bandgap.

For a 1.1 eV Si bottom cell (3rd junction), the S-Q limit maximum STH is only ~17.5%. This is because these cells output higher voltages but due to current density limitations, STH decreases. This kind of behaviour has already been reported [3].

Maximum STH for a tandem PEC-PV-EC hybrid system

Here we present a hybridization between a 2-junction tandem PEC cell and a silicon photovoltaic panel, which is an unconventional and unreported design to the best of our knowledge. The S-Q limit for STH efficiency of a 3-junction system in series has no theoretical gain in relation to a 2-junction system. However, by connecting the two first semiconductors in series configuration and 3rd one in parallel, this limit may be broken down. This hybridization is illustrated in figure 2.11.

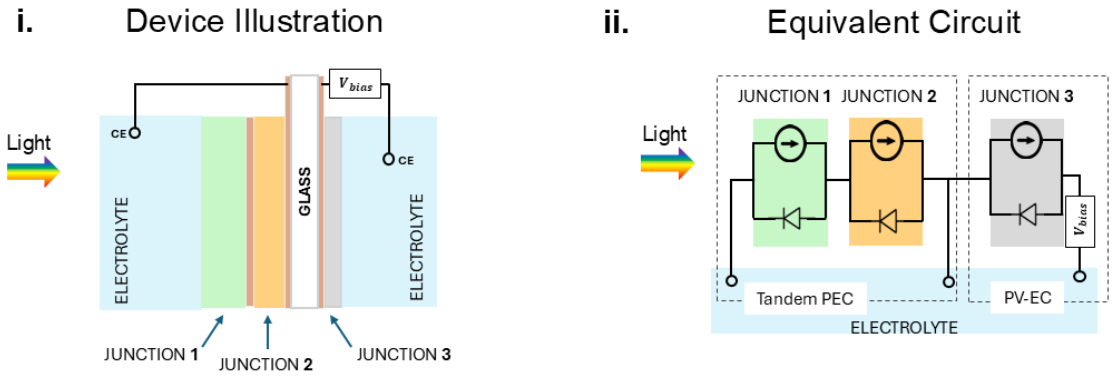


Figure 2.11: **i.** Illustration of hypothetical tandem PEC-PV-EC device. **ii.** Equivalent circuit of the designed hybrid system.

Under this scenario, 3rd junction of silicon (Si) is considered in parallel configuration, which requires a bias.

For biased operation regions, STH efficiency is calculated with equation 1.9. The considered activation voltage for water splitting for the Si cell was $V_{\text{act}} = 1.5\ \text{V}$, as state-of-the-art electrocatalysts can achieve activation overpotentials $\leq 100\ \text{mV}$ [107]. The required bias is then provided by: $V_{\text{bias}} = 1.5 - V_{\text{MPP}}$.

Two quantities were considered in the evaluation of this hybrid system:

$$\text{STH} = \text{STH}_{\text{tandem PEC}} + \text{STH}_{\text{PV-EC}} \qquad (2.29)$$

$$\text{H}_2\ \text{Yield} = \frac{\phi_{\text{H}_2} \cdot \Delta G^0}{\text{Solar}_{\text{c}}} \qquad (2.30)$$

Where STH efficiency is calculated by adding the two subsystems individual efficiencies, according to expression 2.29. As detailed in relation 2.30, H_2 yield rate is calculated by the sum of the two subsystems generated hydrogen fluxes (ϕ_{H_2}), normalized to the incident solar constant (100 mW/cm^{-2}). Figure 2.12 presents the simulation results for this system.

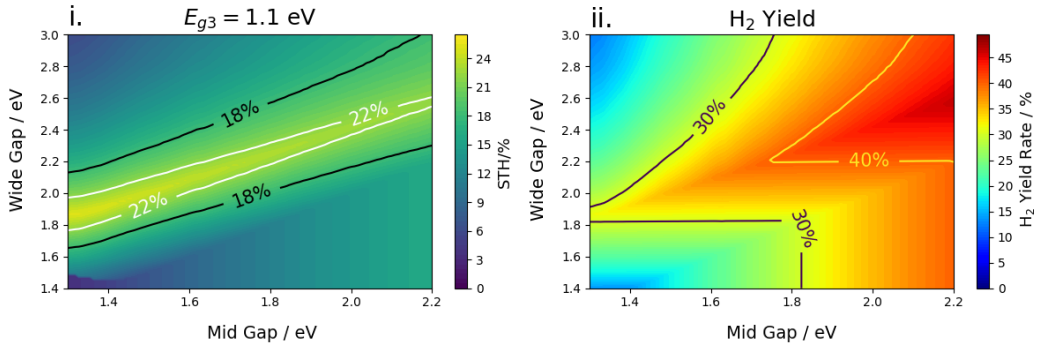


Figure 2.12: **i.** STH efficiency of the system for $E_{g3} = 1.1$ eV. **ii.** H_2 production rate as a function of bandgap pairing for 1.1 eV narrow bandgap: output energy in hydrogen normalized to incident solar energy.

As it is possible to confirm by inspection of figure 2.12 graphics, there are 3 main advantages to this hybridization:

1. The S-Q limit is higher than for full series connection, this is because in parallel the currents add, instead of the voltages. In other words, the 3rd junction does not limit the current density of the system anymore.
2. Unlike in full series connection, there is a broad region for mid and wide bandgap pairings that allow for S-Q limits above 22%, as figure 2.12 shows: transforming the maximum region geometry from a single point (figure 2.10 (ii)), into a straight line (figure 2.12 (i)). Consequentially, the choice in semiconductors pairing is less limited, even enabling good STH efficiencies for combinations like Hematite and WO_3 bandgaps.
3. H_2 yield rate is represented in figure 2.12 (ii). Interestingly, for combinations of wider bandgap materials there is a broad region with over 40% H_2 output in relation to incident solar energy – which may have a significant impact on the price of green H_2 production. This effect is also because of the current density addition property of the parallel configuration, where wide bandgap materials will leave a higher spectral photon flux for the 3rd junction to collect.

This device configuration could allow for utilization of already investigated wider bandgap materials like Hematite, WO_3 and TiO_2 with S-Q limit STH efficiencies above 18% and H_2 yield rates above 40% (normalized to incident solar constant).

2.4. Conclusions

An adapted version of detailed balance limit (S-Q limit) was implemented, enabling the incorporation of losses in photoconversion by consideration of open circuit voltage (V_{OC}) and short circuit current density (J_{SC}) deficits. This model allows for bandgap pairing optimization based on the junctions' bandgaps and photoconversion losses and eventually, can serve as an analysis tool for real scenarios – by allowing to compare tandem PEC cells maximum theoretical efficiencies with experimental data.

With the developed model it is possible to identify Hematite-CuO and CuO-Si as promising materials combinations for STH conversion, based on bandgap and hypothetical photoconversion losses: resulting in almost ~17% and 21% STH efficiencies respectively, under near ideal conditions. These results motivated us to research CuO photocathodes. Although, other factors like the Fermi levels and band bending at semiconductor-electrolyte interface can have significant impacts on real life performances.

The S-Q limit for 3 junction tandem PEC systems revealed interesting results, where by connecting all junctions in series there's a drop in efficiency because of current density limitations and the maximum STH efficiency for $E_{\mathrm{g1}} \in [1.4{,}3]\ \mathrm{eV}$ and $E_{\mathrm{g2}} \in [1.3, 2]\ \mathrm{eV}$ is calculated to be a ~21.21% plateau for $E_{\mathrm{g3}} \in [0.6, 0.8]\ \mathrm{eV}$. The model shows that by connecting the 3rd junction in parallel it is possible to break this limit, increasing the S-Q limit for $E_{\mathrm{g3}} = 1.1\ \mathrm{eV}$ from $\mathrm{STH}_{\mathrm{series}} \approx 17.5\%$ to $\mathrm{STH}_{\mathrm{series+parallel}} \approx 25.2\%$. More interesting than the limit increase, the reshaping of the maximum STH region from a single point to a straight line, enabling a lot of combinations in E_{g1} and E_{g2} that enable maximum STH efficiency. Finally, as the 3rd junction is in parallel and is a low bandgap material, it must work with an external bias, which translates into significantly higher H_2 yielding rates than its bare STH efficiency: enabling above 40% H_2 yielding ratio in relation to the incident solar constant (100 $mWcm^{-2}$), for a broad region of bandgap combinations. As a result, material combinations like WO_3 and TiO_2 could result in STH efficiency above 18%: a clear gain in relation to these bare materials STH efficiency, which is below 6% and 3% respectively.

3. Experimental Methods and Characterization Techniques

This chapter summarizes the materials, synthesis methods and characterization techniques used in the fabrication and analysis of the fabricated photoelectrodes.

3.1. Materials

The fabricated photoelectrodes were deposited onto fluorine-doped tin oxide (FTO) substrates, that exhibit a sheet resistance of 7 Ω/sq (TCO 22-7/LI, SOLARONIX). All chemical reagents were used as received, without further purification. A comprehensive list of the materials employed is provided in Table 3.1

Washing Purposes			
Name	**Chemical Formula**	**Purity / %**	**Supplier**
Acetone	CH_3COCH_3	≥ 99.8	Fisher Scientific
Ethanol	C_2H_6O	≥ 99.8	Fisher Scientific
Laboratory Detergent	-	-	Labkem
Fabrication Purposes			
Copper Sulphate Pentahydrate	$CuSO_4 \cdot 5H_2O$	≥ 98	SIGMA ALDRICH
Ascorbic Acid	$C_6H_8O_6$	≥ 99	SIGMA ALDRICH
Boric Acid	BH_3O_3	≥ 99.8	SIGMA ALDRICH
Sodium Hydroxide	NaOH	≥ 98.6	JGMS

Table 3.1: List of employed reagents and chemicals.

Besides the reagents listed in table 3.1, RO (Reverse Osmosis) water with 18.6 MΩ/cm is used for washing purposes, while UP (Ultra-Pure) 5.8 µS/cm water is used for solution preparation. Both types are obtained with a Direct-Pure UP Ultrapure & RO Lab Water System from Rephile.

3.2. Fabrication Techniques and Synthesis Procedures of the Photoelectrodes

This section outlines the fabrication techniques and synthesis protocols employed in the development of the photoelectrodes. In each section, the procedural steps are presented first, followed by a detailed explanation of the employed techniques in their respective subsections. The substrate preparation, which is a common procedure for all samples, is described in section 3.2.1. The synthesis routes and fabrication techniques for the

CuO photocathodes are aborded in section 3.2.2, while Hematite-CuO tandem heterojunctions related methodologies are detailed in section 3.2.3.

3.2.1. Substrate Preparation

Substrate preparation is held fixed through this thesis development. The FTO substrates, supplied in 10x10 cm sheets, are cut into 1.2x5 cm pieces using a diamond blade and application of pressure.

After cutting, the substrates are cleaned by undergoing 4 consecutive 10 min ultrasonic bath cycles, with the following solvent order: Detergent, Acetone, Ethanol and DI water, as illustrated in figure 3.1. Between consecutive cycles, the substrates were rinsed with DI water. After cleaning, they dry at 80ºC for 30min in a controlled heating chamber.

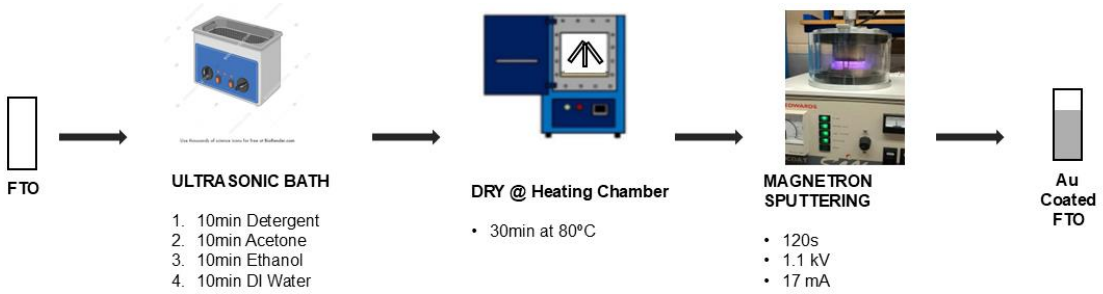


Figure 3.1: Illustration of the substrate preparation procedure.

Finally, a gold (Au) thin film is deposited via magnetron sputtering under an applied voltage of 1.1 kV and a current of approximately 17 mA, for 120s. Prior to deposition, the chamber is purged 5 times (10s pumping vs 3s Ar injection). Subsequently, the system is continuously pumped for 1h until high vacuum is achieved (< 10^{-3} mbar). The purge cycles dilute residual atmospheric contaminants within the chamber by repeated flushing with Ar gas. More details about the magnetron sputtering technique are available in section 3.2.1.1.

3.2.1.1. Magnetron Sputtering

Magnetron sputtering is a physical vapor deposition (PVD) technique, usually employed to deposit metals or ceramics. This technique is used in thin films fabrication, providing a fast, reproductible and efficient pathway to deposit thin film coatings with good adhesion [84,98].

At high enough applied voltages (several thousand volts), the Ar atoms contained in the chamber are ionized and form a plasma. These ions are accelerated by the electric field between the cathode and the anode, as illustrated in figure 3.2 (ii). The accelerated ions

bombard the target material (cathode), releasing both atoms and secondary electrons from the target.

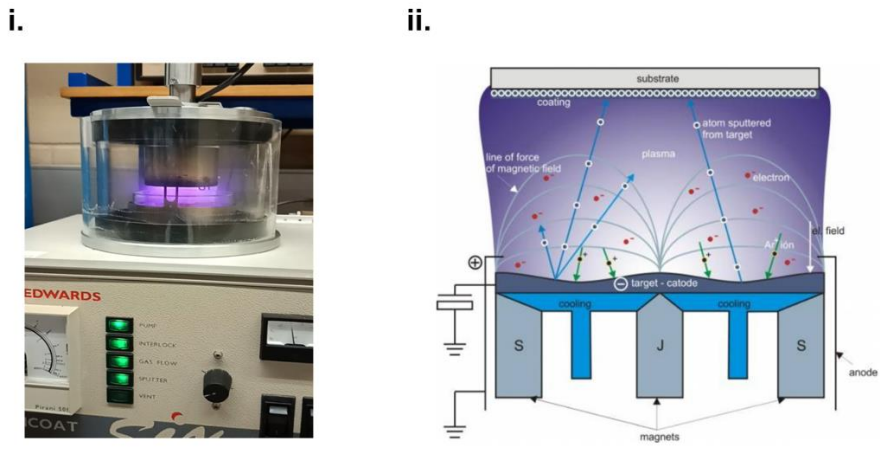


Figure 3.2: **i.** Picture of the utilized magnetron sputtering during deposition. **ii.** Illustration of a magnetron system working principles. Reproduced from [84].

The magnetic field traps the secondary electrons in helicoidal orbits that lead them back to the cathode, where they are either collected or reflected. This magnetic confinement increases the efficiency and deposition rate of the process [85]. The sputtered atoms eventually encounter the substrate and deposit, forming a thin film. For ensuring uniform and homogeneous deposition, high vacuum is very important because it ensures long mean free path of the sputtered atoms, minimizing scattering events with residual gas molecules in the chamber. The utilized magnetron sputter was a BOC Edwards Scancoat Six Sputter Coater, coupled with an Edwards RV3 Rotary Vane Vacuum Pump.

3.2.2. Fabrication Techniques and Synthesis Procedures of the CuO Photocathodes

This section abords the general procedures of the developed CuO photocathodes, alongside the methodologies and techniques utilized throughout the process. Finer details about the synthesis can be found in chapters 4 and 5, while the underlying principles about the employed fabrication techniques may be found in their respective subsections 3.2.2.1 and 3.2.2.2. Two different approaches were taken for the development of the CuO photocathodes:

Route A consists of electrodeposition of copper (Cu), followed by thermal annealing. Prior to deposition, the FTO-Au substrate's edges are covered with Kapton tape to mitigate border effects observed during initial trials. Cu thin films are electrodeposited at ambient temperature, using a 0.2 M copper(II) sulphate pentahydrate, 0.06 M Ascorbic acid (AA) and 0.16 M Boric acid solution, stirred for 25min. This composition is adapted

from a previously reported Fe electrodeposition protocol [87]. Following deposition, the films are annealed in atmospheric air at 550ºC for 2h.

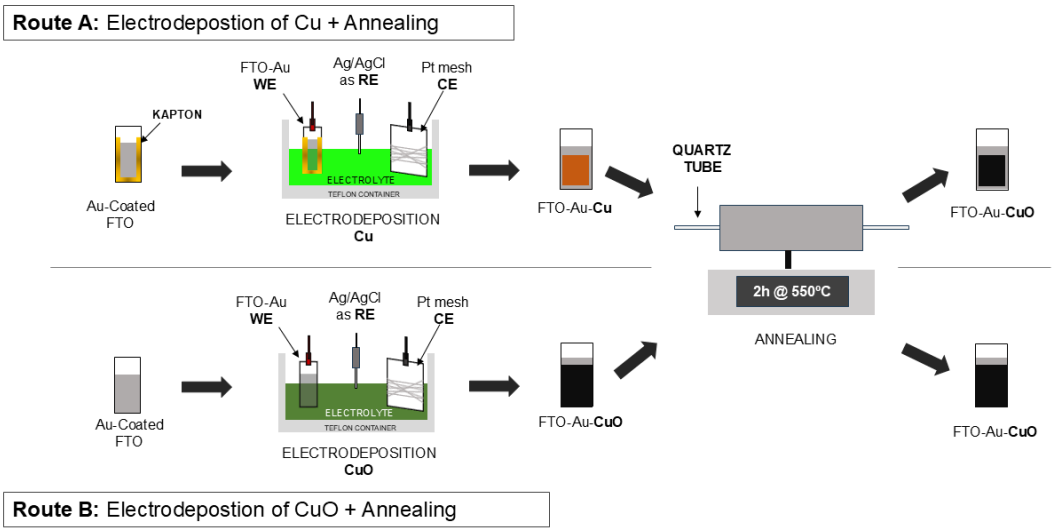


Figure 3.3: Illustration of the developed synthesis routes procedures.

Route B involves the direct electrodeposition of CuO, followed by an annealing as a way of ensuring pure CuO phase. In this case, Kapton is not employed because no border effects were observed during experimental trials. CuO is electrodeposited using the same workstation as in the copper electrodeposition procedure, as illustrated in Figure 3.3. Sodium hydroxide is added to a 0.2 M copper(II) sulphate pentahydrate and 0.06 M ascorbic acid solution until pH 13 is reached. After deposition, the samples were annealed in atmospheric air at 500ºC for 2h, as in “Route A" protocol.

3.2.2.1. Electrodeposition

Electrodeposition (or electrochemical deposition) is a bottom-up micro and nanofabrication technique, that enables the deposition of a chemical species from an ionic electrolyte into a conductive substrate, which acts as an electrode, by application of an external voltage/current [86,98]. This is a highly scalable and cost-effective technique and has several operational modes such as AC or galvanostatic methods, but through the development of this thesis only potentiostatic electrodepositions were employed. A general electrodeposition process may be expressed as:

$$\left(\mathrm{M_xM_y}\right)^{\mathrm{z}} + n\mathrm{xe}^{-} \rightarrow \mathrm{xM}^{0} + \mathrm{yW} \qquad (3.1)$$

Where M is the reduced species, W is a molecule, ion or radical bounded to M forming the complex $\left(\mathrm{M_xM_y}\right)^{\mathrm{z}}$, and n is the number of electrons involved in the reaction [98]. There are also some variations for electrochemical cell’s configurations, some contain 2

electrodes and others 3. In this work, all depositions were conducted using a 3 electrode electrochemical cell, illustrated in figure 3.4. A platinum (Pt) mesh acts as Counter electrode (CE), an Ag/AgCl electrode is used as Reference Electrode (RE) and the prepared substrates act as Working Electrode (WE).

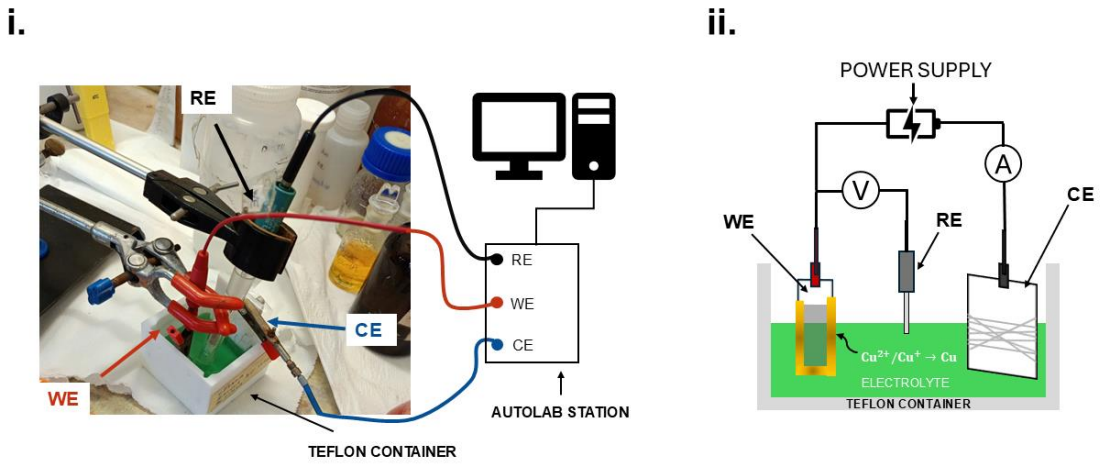


Figure 3.4: **i.** Picture of the electrodeposition working station, with illustration of the connection with the AUTOLAB station and computer. **ii.** Illustration of a 3-electrode electrochemical cell circuit. V – Voltmeter, A- Ammeter.

In potentiostatic mode, the potential difference between the RE and WE is maintained at a fixed value. This applied potential generates an electric field, that in the case of "Route A", attracts copper ions from the electrolyte towards the substrate, where they are further reduced.

Electrodeposition is highly sensitive to the surrounding electrochemical environment. Parameters like electrolyte composition, pH, temperature, applied voltage, substrate characteristics, and many others, can severely influence the electrochemical and optoelectronic properties of the deposited structures [87,98]. For instance, by pH adjustment it was possible to directly electrodeposit CuO using the same precursors as in "Route A", for copper electrodeposition. Additionally, the Au coating on the FTO surface aids in nucleation and promotes film homogeneity [102], certainly having an impact on the resulting crystalline structure as well.

In the conducted depositions, the reagents are weighed rigorously and mixed with water using a magnetic steerer. The different electrodes were connected to an AUTOLAB interface and the deposition $I(t)$ (current vs time) and $Q(t)$ (charge vs time) characteristics were recorded via NOVA 2.1.8 software. The evolution of the deposited charge density over time is given by the following expression:

$$\sigma_{\text{Deposited}}(t) = \int_{t_0}^{t} J(t)dt \quad (3.2)$$

Where t_0 is the initial deposition time, and t is the present time. Relation 3.2 is derived by dividing the recorded $Q(t) = \int_{t_0}^{t} I(t)\,dt$ characteristics, by the sample area "A_{sample}". The area A_{sample} is calculated using ImageJ software. A linear regression is performed to each of the recorded $\sigma_{\text{Deposited}}(t)$, enabling the determination of the deposition rates and calibration of the electrodeposition process. The resulting films thickness d was estimated using Faraday's law of electrolysis [98]:

$$d = \frac{M}{n\rho F}\sigma_{\text{Deposited}}(t_f) \quad (3.3)$$

Where M is the molar mass of the species, F is faraday's constant (96,485 $\text{C}\cdot\text{mol}^{-1}$), ρ is the specific density of the electrodeposited species, and n is the number of electrons involved in the reaction. The final deposited charge density is given by $\sigma_{\text{Deposited}}(t_f) = \frac{Q(t_f)}{A_{\text{sample}}}$.

3.2.2.2. Thermal Annealing

Annealing consists in providing thermal energy to a material. This procedure may induce phase transitions, as well as enhance the crystalline structure of the photoelectrodes [101]. In the synthesis of metal oxide semiconductors, annealing the precursor metals in an oxygen containing environment promotes oxidation and may induce the phase transition from metal to metal-oxide under the right conditions (temperature, oxygen pressure) [65,66,101].

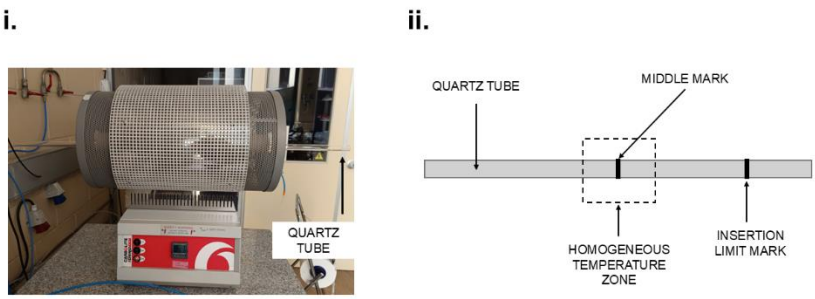


Figure 3.5: **i.** Photograph of the annealing furnace in the heating process. **ii.** Illustration of the quartz tube, with illustration of the homogeneous temperature zone where the samples are placed.

The samples were positioned in a homogeneous temperature zone inside a quartz tube, as illustrated in figure 3.5 (ii). All thermal annealing's were conducted in ambient air 550ºC for 2h, with 10ºC/min heating ramp. The cooling was performed at ambient

temperature with a controlled 8ºC/min cooling ramp, ensuring the cooling ramp is not below this value. During Cu→CuO phase transition, the number of copper atoms is conserved. Consequently, the number of Cu atoms is equal to the number of CuO molecules formed. The later condition can be expressed as follows:

$$\frac{\rho_{\mathrm{CuO}}}{M_{\mathrm{CuO}}} V_{\mathrm{CuO}} = \frac{\rho_{\mathrm{Cu}}}{M_{\mathrm{Cu}}} V_{\mathrm{Cu}} \qquad (3.4)$$

Assuming the geometric area of the films remains approximately constant during the Cu→CuO transition, the CuO thickness d_{CuO} after annealing is given by:

$$d_{\mathrm{CuO}} = \frac{M_{\mathrm{CuO}}}{\rho_{\mathrm{CuO}}} \frac{\rho_{\mathrm{Cu}}}{M_{\mathrm{Cu}}} d_{\mathrm{Cu}} \qquad (3.5)$$

Relationship 3.5 is equivalent to consider direct CuO electrodeposition in Faraday's law, equation 3.3. The proportion between CuO and Cu thickness is then roughly: $\frac{M_{\mathrm{CuO}}}{\rho_{\mathrm{CuO}}} \frac{\rho_{\mathrm{Cu}}}{M_{\mathrm{Cu}}} = 1.77$.

3.2.3. Fabrication Techniques and Synthesis Procedures of the Hematite-CuO tandem heterojunctions

Following the successful development of good CuO photoelectrodes, it's possible to couple hematite (α-F_3O_4) with CuO to form a tandem heterojunction. To obtain the hematite layer, an iron (Fe) layer is deposited through Ion Beam Deposition (IBD), which oxidizes to hematite phase during thermal annealing. Details on the IBD technique and deposition conditions are available in section 3.2.3.1.

For the fabrication of Hematite-CuO heterojunctions, two variations of "Route A" are implemented:

Route A1 initiates with the established protocol in Route A, wherein CuO photocathodes are fabricated by thermal annealing of the electrodeposited Cu thin films. Subsequentially, Fe is deposited onto the CuO photocathode using Ion Beam Deposition (IBD), forming an FTO-Au-CuO-Fe junction. Finally, the junction undergoes a second annealing, as described in section 3.2.2.2, oxidizing the Fe layer into hematite (α-Fe_2O_3), resulting in the final FTO-Au-CuO-α-Fe_2O_3 heterojunction.

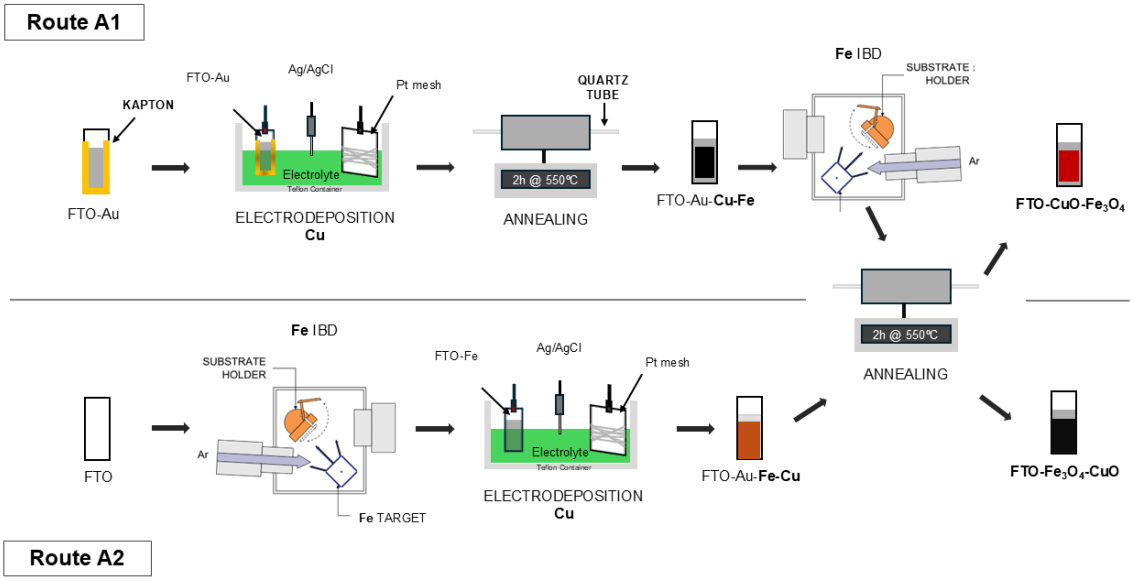


Figure 3.6: Procedure illustration of Route's A1 and A2 for hematite-CuO heterojunction synthesis.

Route A2. The FTO substrate preparation procedure was conducted as described in section 3.2.1, with the exception that no gold coating is applied. Following substrate preparation, iron (Fe) is deposited by IBD forming an FTO-Fe structure. Route A protocol is employed to the FTO-Fe junction after IBD, as illustrated in figure 3.6, resulting in an FTO-α-Fe_3O_4-CuO heterojunction.

3.2.3.1. Ion Beam Deposition (IBD)

Ion beam deposition (IBD) operates by directing a controlled beam of energized ions (Ar beam) onto a material target. The target's atoms become loose after collision, forming a plume of the target material. This plume eventually deposits on the substrate holder, forming a thin film [93]. An IBD chamber is illustrated in figure 3.7 (ii).

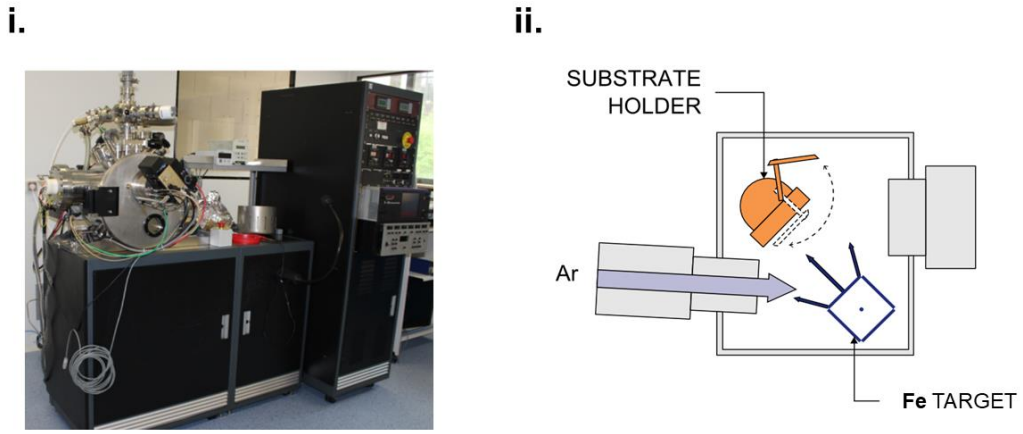


Figure 3.7: **i.** Photograph of IBD system from Commonwealth Scientific at CEMUP clean-room facility. Reproduced fom [95]. **ii.** illustration of the inside chamber of a IBD system and its operating components. Adapted from [93].

To deposit pure metallic thin films, this beam of ions must be of a noble gas like Argon (Ar), guaranteeing no side reactions with the material. The deposition must be conducted at low pressures to ensure long mean free path of the ejected atoms, much like in magnetron sputtering. IBD is renowned for its un-matched batch uniformity and repeatability, that allows controlled deposition of thin films [93]. All Iron depositions were carried using IBD, with table 3.2 parameters, resulting in a deposited iron (Fe) layer with 88.5 nm of thickness.

Ion Beam Deposition Parameters

P_B / Torr	$1.2x10^{-6}$	**V_A / V**	150
V_B / V	1000	**I_A / mA**	2
I_B / mA	11	**V_D / V**	38
P_W / Torr	$1.4x10^{-4}$	**I_D / A**	19
I_C / A	7.4	**V_C / V**	10
Final Iron (Fe) Thickness / nm		88.5	

Table 3.2: Ion Beam deposition parameters.

3.3. Characterization Techniques

The characterization techniques and deposition solutions are presented in this section, accompanied by a brief description of their working mechanisms and underlying physical principles.

3.3.1. Structural Characterizations

The structural properties of the photoelectrodes were investigated via Raman Spectroscopy. Raman spectroscopy works by measuring Raman scattering, which is an inelastic type of optical scattering, resulting from light-matter interaction.

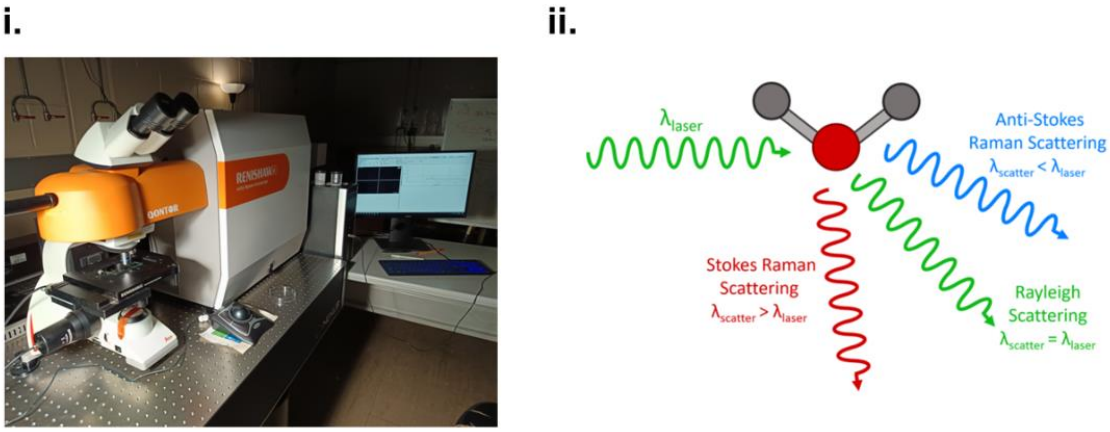


Figure 3.8: **i.** Raman Microscopy Station at IFIMUP. **ii.** Illustration of Raman Scattering (inelastic) and Rayleigh Scattering (elastic) effect on the scattered photon's wavelength – or equivalently: energy. Reproduced from [103]

In this type of scattering, photons interact with molecule/lattice vibrations that result in a shift in the photon's energy. This of course has an impact on the photon's frequency:

$$\omega_{\mathrm{R}} = \omega \pm \omega_{\mathrm{vib}} \quad (3.6)$$

Where ω_R is the frequency of the scattered photon and ω is the frequency of the incident photon, ω_{vib} is the Raman shift associated with the lattice's vibrational modes. This shift can be positive or negative, corresponding to the de-excitation (Anti-Stokes) or excitation (Stokes) of vibrational modes. Raman spectroscopy allows to measure ω_{vib}, thus providing a spectral signature of the crystalline structure of a material. These spectrums contain rich structural information, for instance, a deviation $\Delta\omega_{\mathrm{vib}}$ from the expected ω_{vib} can be related to strain within the lattice [81,82]:

$$\Delta\omega_{\mathrm{vib}} = b\varepsilon_{\mathrm{p}} \quad (3.7)$$

Where b is a constant of the material and ε_{p} is the strain in the parallel direction to the vibration. Negative deviations ($\Delta\omega_{\mathrm{vib}} < 0$) are related with tensile stress and positive deviations ($\Delta\omega_{\mathrm{vib}} > 0$) are related with compressive stress. If the deviations are the same for all modes, then the strain is isotropic [81,82]. Crystallinity is associated with high and sharp Raman shift peaks. In contrast, amorphous/disordered regions provide broader peaks or may exhibit a sloping baseline signal due to breakdown of long-range translational symmetry [83].

The photoelectrodes crystalline structure is accessed using Raman spectroscopy with a RENISHAW inVia Raman microscopy setup at IFIMUP (FCUP), using a monochromatic 532nm excitation laser. The spectral data was acquired by averaging three sets of 10-second acquisitions at each measured spot. Multiple regions of each sample were evaluated, ensuring the acquired spectrum is representative of the sample. The Raman shift peaks are identified using Lorentzian fits to the measured spectrum using ORIGINLab and compared with literature reference spectrums [90,91,92].

3.3.2. Morphological Characterizations

The morphology of the fabricated samples is studied using SEM (FEI Quanta 400FEG Field Emission at CEMUP), operated at an accelerating voltage of 15 keV and magnifications ranging from $\times 10^3$ to $\times 10^5$. The samples are firstly investigated in different zones to ensure the micrographs are representative of the sample's morphology. Elemental composition was accessed with Energy Dispersive X-ray Spectroscopy (EDS). Additionally, atomic contrast imaging was employed to visualize different atomic species. Posterior analysis of the SEM images was carried with ImageJ

software aid, which enables quantitative measurements of morphological features by calibrating spatial dimensions with a known reference scale.

3.3.3. Electrochemical Characterizations

The dynamics between substrate and electrodeposition electrolyte are investigated using cyclic voltammetry. Cyclic voltammetry consists of recording I-V characteristics, while sweeping the potential at a constant rate for a desired electrochemical window. Multiple cycles may be performed with a constant sweeping rate, or with varying sweeping rate between cycles. This technique allows for identification of redox reactions and their reversibility, amongst others [88]. The utilized deposition solutions were studied with cyclic voltammetry for different sweeping rates, using the AUTOLAB workstation controlled via NOVA software, with a 3 electrode electrochemical setup equivalent to the one of figure 3.4.

3.3.4. Optical Characterization

One of the most important properties for solar-to-hydrogen conversion (STH) is the bandgap (E_g), as emphasized in chapter 2. Knowing the material's reflectance provides enough information to estimate the photoelectrodes bandgap using the Kubelka-Munk functions:

$$F(R) = \frac{(1-R)^2}{2R} \quad (3.9)$$

$$|F(R) \cdot h\upsilon|^n \propto (E - E_g) \quad (3.10)$$

With $n = 1/2$ for indirect allowed transitions and $n = 2$ for direct allowed transitions [89]. This functions transition slope may be approximated to a straight light through a linear regression, where the intersection of the fitted function $|F(R) \cdot h\upsilon|^n = m \cdot E + b$ with the lower plateau a fulfils the condition $|F(R) \cdot h\upsilon|^n = a$, allowing to determine bandgap. The uncertainty related to bandgap estimation is calculated via the error propagation formula [79], which is available in the supplementary information.

Optical reflectance of the developed photoelectrodes was measured by UV-VIS-NIR spectroscopy with a SHIMADZU UV-VIS 3600i Plus spectrometer, covering the 200-1200nm spectral range. The samples were placed facing the interior of the integrator sphere, which ensures all light diffusively and specularly reflected light from the sample surface is redirected until it is collected at the detector, as illustrated in figure 3.10 (ii).

3.3.5. Photoelectrochemical Performance

Photoelectrochemical performance is access by J-V measurements using Linear Sweep Voltammetry (LSV), both in dark and under 1 Sun AM 1.5 illumination, with an illumination area of 0.528 cm^2. The measurements are performed in a cappuccino cell in 3 electrode configuration with: Pt wire as CE, Ag/AgCl as RE and the photoelectrodes as WE. The electrolyte used is a pH 13.6 NaOH aqueous solution. J-V characteristics are acquired via LSV (Linear Sweep Voltammetry) with a ZENNIUM (Zahner Elektrik, Germany) workstation controlled via Thales software, with 10mV/s sweep rate. The employed set-up is represented in figure 3.9.

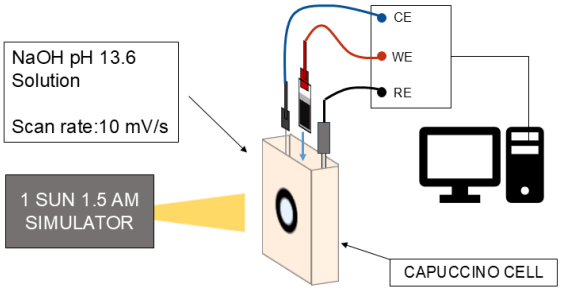


Figure 3.9:: Illustration of the photoelectrochemical characterization station. All PEC characterizations are performed at LEPABE, FEUP.

All solar measurements are performed using front illumination, meaning that light insides in the semiconductor material first, as illustrated in figure 3.9. For the CuO photocathodes, the potential ranges from 0.2 to 0.8 V vs RHE, while for the Hematite-CuO heterojunctions a 0.2 to 1.3 V vs RHE window is considered. The potentials in relation to Ag/AgCl are converted to reversible hydrogen electrode (RHE) scale using Nernst equation:

$$E_{\mathrm{RHE}} = E_{\mathrm{Ag/AgCl}} + 0.059 \cdot \mathrm{pH} + E^{0}_{\mathrm{Ag/AgCl}} \qquad (3.14)$$

Where $E_{\mathrm{Ag/AgCl}}$ is the measured potential and $E^{0}_{\mathrm{Ag/AgCl}} = 0.197\ \mathrm{V\ vs\ RHE}$ is the Ag/AgCl electrode potential under standard conditions.

4. CuO Photocathodes: Electrodeposition of Copper followed by Annealing

4.1. Applied Potential Optimization of Copper Electrodeposition

This subsection outlines the conducted experimental procedures and results for optimization of the deposition potential for copper (Cu) electrodeposition. As described in section 3.2.2.1, electrodeposition is highly sensitive to the surrounding electrochemical environment. Consequently, the applied deposition potential is one of the most important parameters in electrodeposition as it can affect the deposited film phase and properties [84].

4.1.1. Electrolyte Characteristics and Substrate-Electrolyte Electrochemical Dynamics

This section outlines the employed electrolyte characteristics, as well as a cyclic voltammetry study to find a suitable deposition electrochemical window.

Electrolyte characteristics

For electrodeposition of metallic Cu thin films, an electrolyte used in Iron-Cobalt deposition is adapted [84], with the described concentrations for Route A procedure in section 3.2.1. Table 4.1 describes important electrolyte composition characteristics.

Reagent	**Concentration (M)**	**Molar Mass (g/mol)**	**DI WATER**	
$CuSO_4 \cdot 5H_2O$	0.2	249.685	**Volume**	**Conductivity**
$C_6H_8O_6$	0.055	182.08	50 mL	5.8 µS/cm
BH_3O_3	0.16	61.84	**Precursor/Reducing Agent Ratio**	4:1

Table 4.1: Electrolyte composition for copper electrodeposition.

Copper (II) sulphate pentahydrate acts as copper precursor, ascorbic acid as a reducing agent and boric acid as a buffer – aiding in pH adjustment and stabilization. This electrolyte is held fixed throughout this chapter's development.

When dissolving in acidic environment, copper(II) sulphate pentahydrate breaks into copper(II) ions. These Cu^{2+} ions can react with ascorbic acid to form copper-ascorbate complexes. In these complexes Cu(II) valence can change to Cu(I) [80], but also aid in precipitation of Cu(II)/Cu(I) ions into Cu particles [77]:

$$CuSO_4 \cdot 5H_2O \rightarrow Cu^{2+} \quad (4.1)$$

$$2Cu^{2+} + C_6H_8O_6 \rightarrow 2Cu^{+} + C_6H_6O_6 + 2H^{+} \quad (4.2)$$

$$Cu^{2+} + C_6H_8O_6 \rightarrow Cu + C_6H_6O_6 + 2H^{+} \quad (4.3)$$

Room temperature thermal energy is enough to drive the overall reaction 4.3, with reported copper precipitate yields of around 15% for precursor/reducing agent concentration ratios of 1:6 at 25ºC after 24 hours [77] – showcasing the reducing power of ascorbic acid. According to literature, for a 1:3 ratio only ~0.5% copper precipitation yield/hour is expected, and this yield decreases with the precursor/reducing agent ratio [77]. The employed deposition electrolyte has a 4:1 ratio, as detailed in table 4.1, but copper precipitation was still observed during solution steering. Having copper precipitated/precipitation during solution may harm film quality.

Steering the solution introduces extra kinetic energy which may induce extra precipitation. Limiting the steering time to 25 min at 340 rpm minimized precipitation, resulted in no visible copper particles in as prepared solution, at a stable pH of 2.6 ± 0.1.

Cyclic Voltammetry

To further inspect the solution electrochemistry and identify a suitable chemical window for copper deposition, the solution was studied with cyclic voltammetry for the bare FTO-Au substrates. Figure 4.1 (i) shows the CVs for scanning rates ranging from 10 to 160 $\mathrm{mV} \cdot \mathrm{s}^{-1}$. The potential values are converted to RHE using Nernst's equation (equation 3.14).

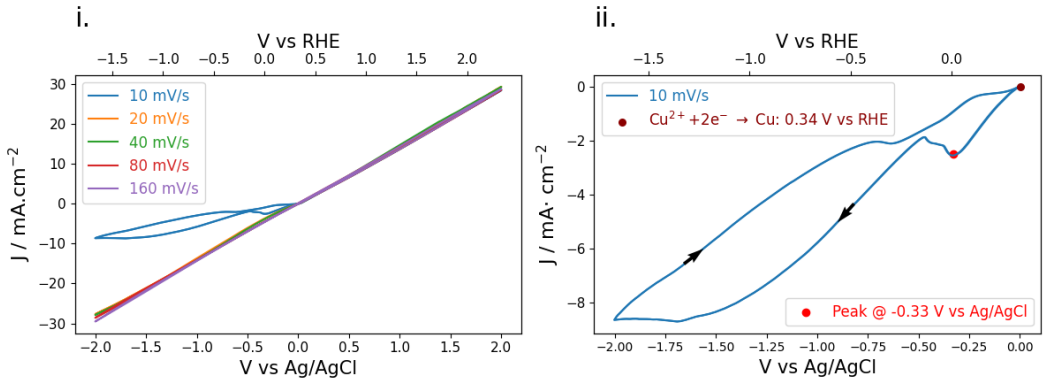


Figure 4.1: Cyclic Voltammetry's (CV) for the represented solution in table 4.1, for the photoelectrodes substrates: FTO-Au. **i.** Varying sweep rate for the same substrate. **ii.** 10 mV/s CV for cathodic current density J.

Figure 4.1 (ii) outlines electrochemical window where copper may deposit. After the first CV, the behavior in the cathodic region is ohmic, as in the anodic side (copper reduction at platinum site). Suggesting that some copper remains in the FTO-Au surface after the first scan, forming an FTO-Au-Cu structure and impacting the overall electrochemical behavior.

The possible cupric ions reduction reactions are listed below [114]:

$$\mathrm{Cu}^{2+} + e^- \rightarrow \mathrm{Cu}^{+} \quad : E_{\mathrm{red}} = 0.15\ \mathrm{V\ vs\ RHE} \qquad (4.4)$$

$$\mathrm{Cu}^{+} + e^- \rightarrow \mathrm{Cu} \quad : E_{\mathrm{red}} = 0.52\ \mathrm{V\ vs\ RHE} \qquad (4.5)$$

$$\mathrm{Cu}^{2+} + 2e^- \rightarrow \mathrm{Cu} \quad : E_{\mathrm{red}} = 0.34\ \mathrm{V\ vs\ RHE} \qquad (4.6)$$

The peak around -0.33 V vs Ag/AgCl (0.017 V vs RHE), is most likely related to Cu(II)→Cu(I) reduction (0.15 V vs RHE, equation 4.1) whose reduction potential becomes more negative by the copper-ascorbate complexes. The cathodic region starts at 0.34 V vs RHE, indicating direct reduction of Cu (II) ions (equation 4.6). With this information, a suitable electrochemical deposition window is $[-1.5, 0.34]$ V vs RHE.

4.1.2. Copper (Cu) Electrodeposition

After assessment of the FTO-Au (substrate)/Electrolyte electrochemical behavior, 5 deposition potentials lying inside the electrochemical window determined in section 4.1 were selected, as presented in figure 4.2 (i). Different samples were deposited at these applied potentials for a fixed deposition time of 5 minutes, as listed in table 4.2.

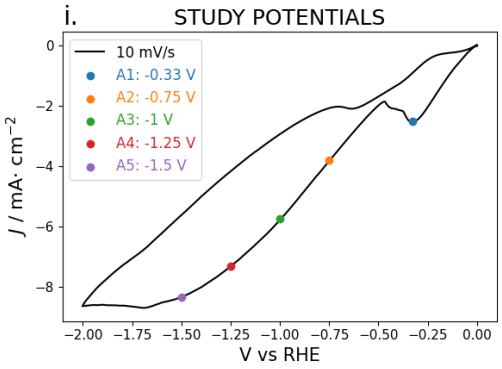


Figure 4.2: Selected deposition potentials for sample fabrication

Sample	V_{Dep} vs Ag/AgCl	Time / min
A1	-0.33	5
A2	-0.75	5
A3	-1.00	5
A4	-1.25	5
A5	-1.50	5
$T_{\mathrm{station}} = 20$°C		

Table 4.2: Batch deposition parameters.

The samples showed quite different electrodeposition characteristics, as figure 4.3 demonstrates, for samples A1, A2 and A3. For samples A4 and A5, there seems to be no explicit difference in the electrodeposition characteristics.

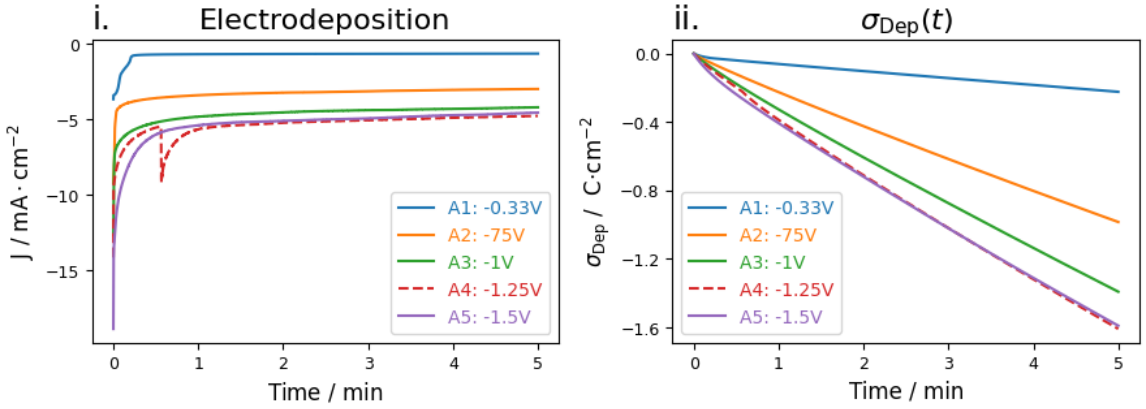


Figure 4.3: **i.** Electrodeposition $J(t)$ characteristics. **ii.** Deposited charge density over time ($\sigma_{\mathrm{Dep}}(t)$).

Charge density versus time ($\sigma_{\mathrm{Dep}}(t)$, equation 3.2), represented in figure 4.3 (ii), shows a clear significant increase in the final deposited charge absolute value with more negative deposition potentials until $V_{\mathrm{Dep}} = -1.5\ \mathrm{V\ vs\ Ag/AgCl}$. This increase in the final deposited charge is related to the higher deposition current densities observed in figure 4.3 (i). These currents increase because of the higher V_{Dep} (deposition voltage) induced electric fields. The fact that the deposition rate for A4 (-1.25 V) and A5 (-1.5 V) samples is very similar means the limiting current has been achieved, where the current is limited by diffusion, which states [119]: $J_L = -nFD\frac{C_0^{\mathrm{Bulk}}}{\delta}$. Where D is the diffusion coefficient of the species, δ is the diffusion layer thickness and C_0^{Bulk} is the bulk concentration. Consequently, applying higher deposition potentials will not substantially increase the current.

Figure 4.4 shows the deposition rates for each of the selected potentials. The rates are obtained through a linear regression to the $\sigma_{\mathrm{Dep}}(t)$ characteristics, for which the fitting parameters are listed in table 4.3.

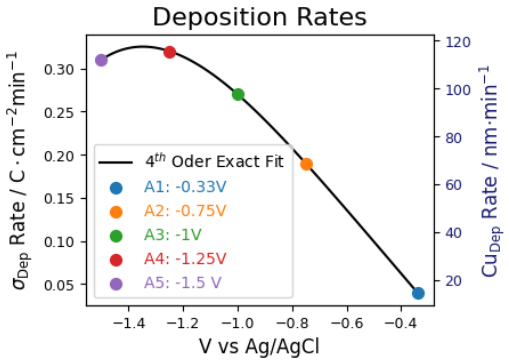


Figure 4.4: Deposition Rates for charge density and Cu.

Sample	Slope	Intercept	R^2
A1	0.04	0.03	0.9994
A2	0.19	0.04	0.9996
A3	0.27	0.06	0.9995
A4	0.32	0.09	0.999
A5	0.31	0.14	0.9991

Table 4.3: Parameters of the various $\sigma_{\mathrm{Dep}}(t)$ regressions.

Table 4.3 parameters enable the calibration of future electrodepositions. The depositions are conducted in an electrochemical window where both Cu(I) and Cu(II) reductions are expected (as detailed in section 4.1.1). However, the assumed number of electrons involved in copper reduction is $n = 2$ because it's the potential where cathodic current begins. Consequently, the Cu deposition rates ($\mathrm{Cu_{Dep}}$) represented in figure 4.3 are calculated using Faraday's law of electrolysis with $n = 2$ (equation 3.3).

4.1.3. Photoelectrochemical Characterization

After Cu electrodeposition, the five samples prepared at different applied potentials were converted into CuO semiconductors by thermal annealing (as described in Section 3.2). This yielded the first group of CuO photocathodes, each obtained at a distinct deposition applied potential. Their photoelectrochemical performance was then evaluated to determine the optimal deposition condition. The fabricated CuO thin films are characterized as described in section 3.3.5. For control, an IBD deposited Cu thin film is annealed in equal conditions and measured for comparison. Figure 4.5 shows the measured photo response, and for visual clarity purposes, samples A1 and A2 are represented in plot (i), and the remaining in plot (ii).

Samples A1 and A2 showed irregular photoelectrochemical behavior. In sample A1 ($-0.33\mathrm{V}$), the dark current density is superior to under illumination conditions for some regions, even showing dark current maximum near Cu(II) reduction potential. Sample A2 ($-0.75\mathrm{V}$) shows an improved photo response, but the dark maximum behavior is also present. This behavior, also observed in the IBD sample, suggests chemical reactions in dark conditions, which are most likely linked to corrosive reactions at the sample-electrolyte interface and related with Cu(II) reduction.

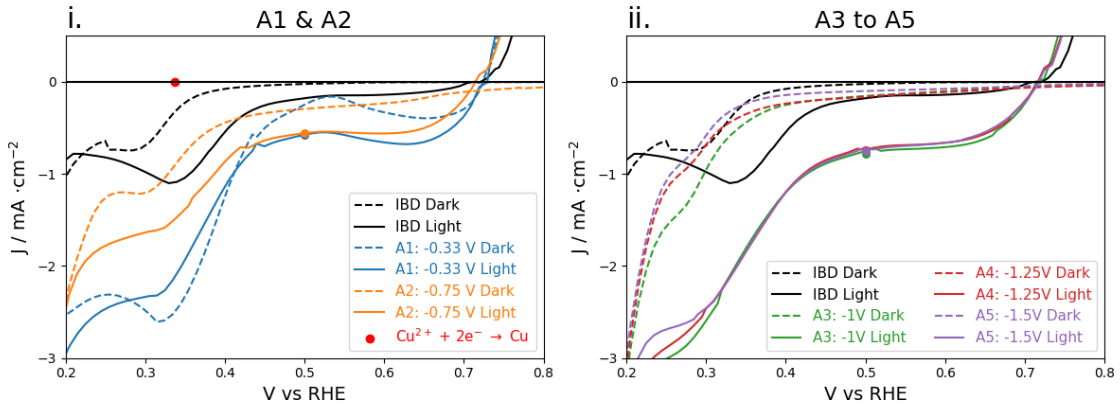


Figure 4.5: Photoelectrochemical performance of the fabricated photoelectrodes. The samples are represented in different plots with IBD reference for ease in the curve's visualization. **i.** A1 and A2 samples photo response. Red point: Cu (II) to Cu potential, equation 4.6. **ii.** A3 to A5 samples photo response.

Unlike samples A1 & A2, the remaining samples show a clearer photo response and don't exhibit an evident dark current maximum around Cu(II) reduction. As observed in figure 4.5, the fabricated CuO photocathodes exhibit photocurrent density in $V \in [0.2, 0.72]$ V vs RHE interval. Subsequently, the potential 0 V vs RHE, where photocurrent is usually measured for comparison in photocathodes, is outside the photo response zone. As such, the photocurrent density (J_{photo}) was taken at 0.5 V vs RHE for all samples, far from Cu(II) reduction potential zone. Table 4.4 outlines the measured onset and photo-current values.

Sample	V_{Dep} vs Ag/AgCl	$\lvert J_{photo} \rvert$ @ 0.5 V vs RHE (mA·cm^{-2})	V_{onset} vs RHE
IBD	-	0.14	0.71
A1	-0.33	0.58	0.729
A2	-0.75	0.56	0.714
A3	-1.00	0.78	0.722
A4	-1.25	0.74	0.724
A5	-1.50	0.75	0.724

Table 4.4: Summary results for the potential study: absolute photo-current density J_{photo} @ 0.5 V and V_{onset} vs RHE.

The sample with best photocurrent was A3, deposited at -1 V vs Ag/AgCl with $J_{\text{photo}} = 0.78\ \text{mA} \cdot \text{cm}^{-2}$ @ 0.5 V vs RHE. Although samples A3 to A5 do not show significantly different photocurrent densities (see figure 4.5 (ii)).

4.1.4. Morphological Characterization

The morphology is investigated with scanning electron microscopy (SEM), as described in section 3.3.2. Figure 4.6 shows SEM micrographs to view the morphologies of samples A1 to A4. Sample A5 was not measured because of its close similarity to A4.

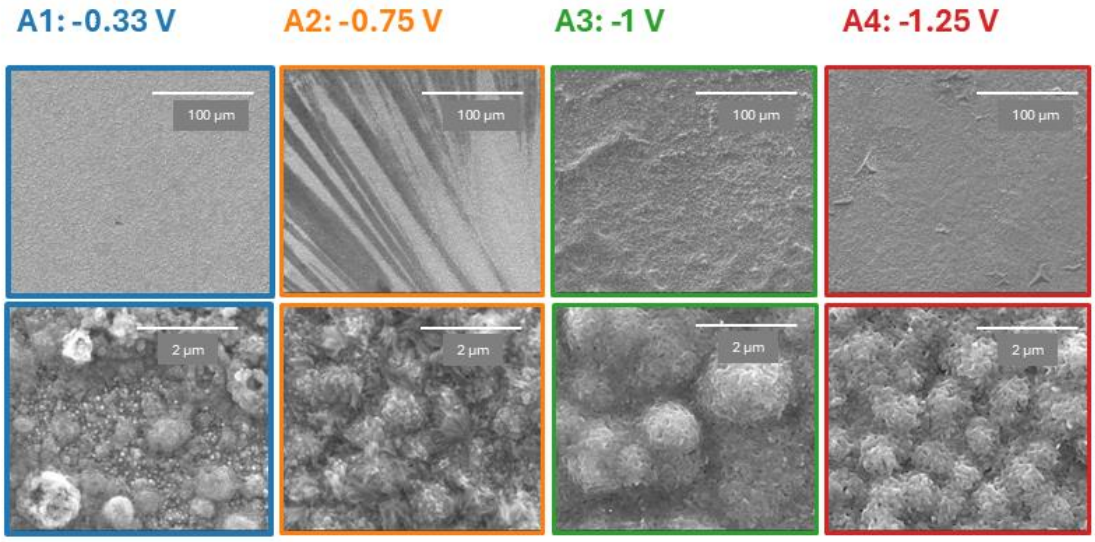


Figure 4.6: SEM micrographs of the CuO photocathodes posterior to photoelectrochemical characterization.

Observing the $100\ \mu m$ scale micrographs in figure 4.6, the samples morphology appears to be very homogeneous. The bright texture observed in sample A2 ($-0.75\ V$) at both scales ($1 \text{ and } 100\ \mu m$) was confirmed to be NaOH electrolyte remains by EDX analysis.

Unlike samples A3 and A4, sample A1 (-0.33 V) seems to be highly corroded, having the TCO exposed in some areas, as this was confirmed by electron backscattering mode (atomic contrast imaging). Both samples A3 (-1.0 V) and A4 (-1.25 V) show a porous morphology, but also a “spiked” grain morphology, suggesting some residual corrosion of these samples as well.

4.1.5. Structural Characterization

The structure of the CuO photocathodes is assessed with Raman spectroscopy, as described in section 3.3.1. These measurements were performed after photoelectrochemical characterization, with the goal to detect any Cu_2O phase formed at the surface during photo-performance. Figure 4.7 contains the measured Raman spectra, where A1 ($-0.33\ V$) is not considered because it was severely damaged after photoelectrochemical measurements.

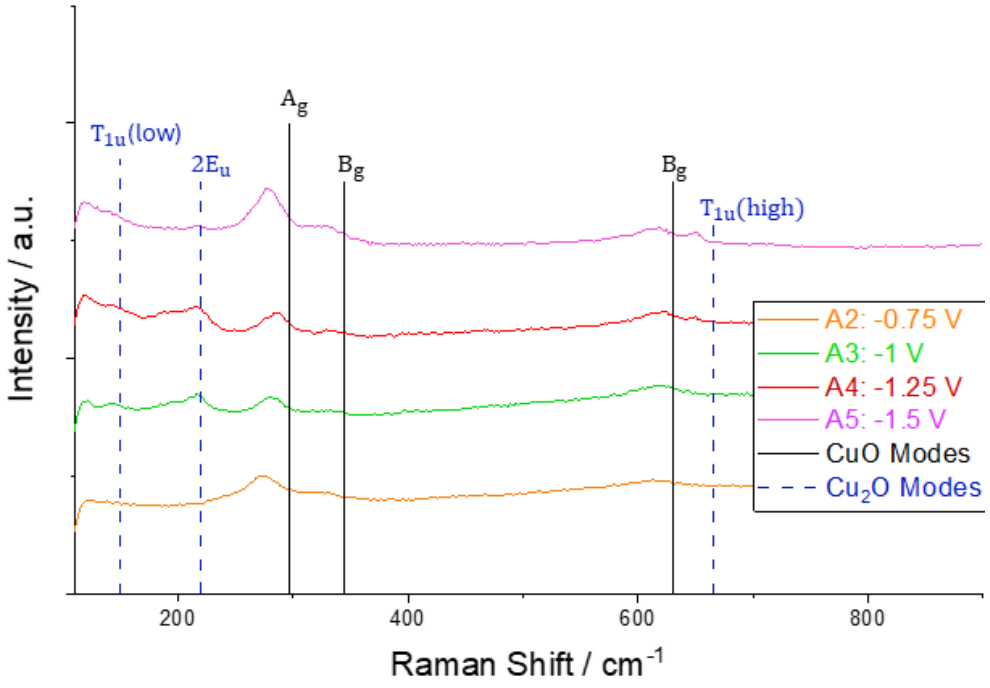


Figure 4.7: Raman spectrum of samples A2 to A5 with Cu_2O and CuO literature Raman shift peaks. CuO modes: [85]; Cu_2O modes: [86].

As observed in figure 4.7, all samples show a clear shift to the left (negative $\Delta\omega_{\mathrm{vib}}$) of the reported Raman shift values for CuO phase, which is associated with tensile stress, as explained in section 3.3.1. This behavior is most likely related to thermal expansion during annealing but also to the Cu→CuO phase transition that corresponds to a 1.77 thickness expansion at a fixed area, as demonstrated in section 3.2.2.2.

Sample A2 ($-0.75\ \mathrm{V}$) shows no clear Cu_2O peak but exhibited bad photoelectrochemical performance as shown in figure 4.5 (i). All Cu_2O modes detected in sample A3 ($-1\ \mathrm{V}$) are also present in both A4 and A5. Unlike A3, A4 ($-1.25\ \mathrm{V}$) and A5 ($-1.5\ \mathrm{V}$) show a noticeable T_{1u} (high) IR defect activated mode. The structural integrity of A3 ($-1\ \mathrm{V}$) in relation to the other samples also suggests $\mathrm{V_{Dep}} = -1.0\ \mathrm{V\ vs\ Ag/AgCl}$ as a suitable deposition potential.

4.2. Optimization of Film Thickness

Photoconversion is a balance between photon absorption and charge collection efficiency: thicker samples absorb more because there's more material to absorb light (Beer-lambert Law of absorption) but thicker samples also mean that the charge carriers must travel longer distances to be collected – increasing the probability of charge recombination before collection. As such, an optimal thickness that maximizes photo performance exists. For accessing optimal film thickness, the deposition time is varied

under the optimized deposition applied potential of $-1\ \mathrm{V\ vs\ Ag/AgCl}$. Section 4.2.1 introduces an implemented variation on the deposition cell geometry that resulted in improved film homogeneity and PEC performance. The remaining sections present this study in a similar fashion to section 4.1.

4.2.1 Electrochemical Cell Geometry

Previously to this chapter experimental execution, a change in the geometry of the electrodeposition cell was conducted. The distance between the reference electrode and working electrode (WE) was changed, as illustrated in figure 4.8.

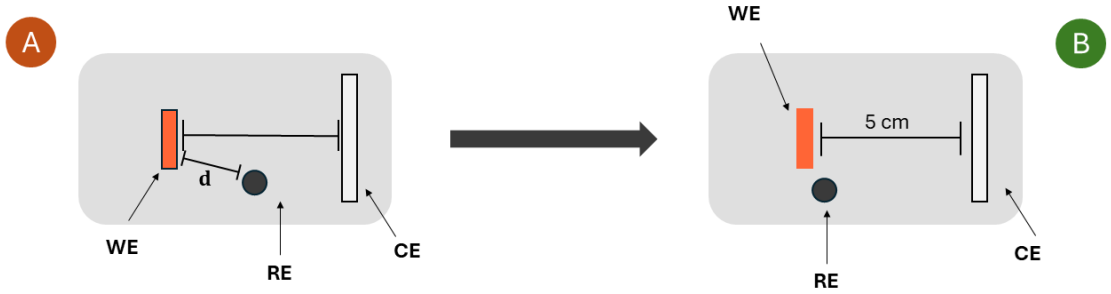


Figure 4.8: **A**: Previous set-up configuration. **B**: Employed set-up configuration in this section.

The RE was placed as near as possible to WE because it is a more stable electrochemical region (well-defined potential, electrochemical reactions), improving potential control and reducing ohmic drop [88]. This variation did not affect the electrodeposition characteristics behavior, although it led to more homogeneous electrodeposited films with more defined grain morphology in the CuO photocathodes.

4.2.2. Copper (Cu) Electrodeposition

Photoconversion is a competitive process between charge carrier generation and recombination, as outlined at the beginning of the chapter. Consequently, an optimal thickness that maximizes photoconversion and STH efficiency exists.

For ideal film ideal thickness assessment, the deposition time varies between 2.5 and 40 min in powers of 2, using the same electrolyte. According to the prior calibration of section 4.1.2 for Cu electrodeposition and the Cu→CuO expansion coefficient (equation 3.5), these deposition times correspond to theoretical CuO thicknesses ranging from ~500 to 7000 nm. Table 4.5 details the deposition conditions and expected CuO theoretical thicknesses.

Sample	Deposition Time / min	Theoretical Cu thickness / nm	Theoretical CuO thickness / nm
B1	2.5	269.7	477.4
B2	5	517.5	915.9
B3	10	1012.92	1792.9
B4	20	2003.82	3546.8
B5	40	3985.6	7054.5
$T_{station} = 20°C$		$V_{Dep} = -1$ V vs Ag/AgCl	

Table 4.5: Batch deposition times and theoretically expected thickness.

The batch deposition characteristics ($J(t)$ and $\sigma_{Dep}(t)$) are presented in figure 4.9, showing very similar electrodeposition characteristics. Noticeably, sample B5 (40 min) seems to deviate from the observed behavior of the remaining samples.

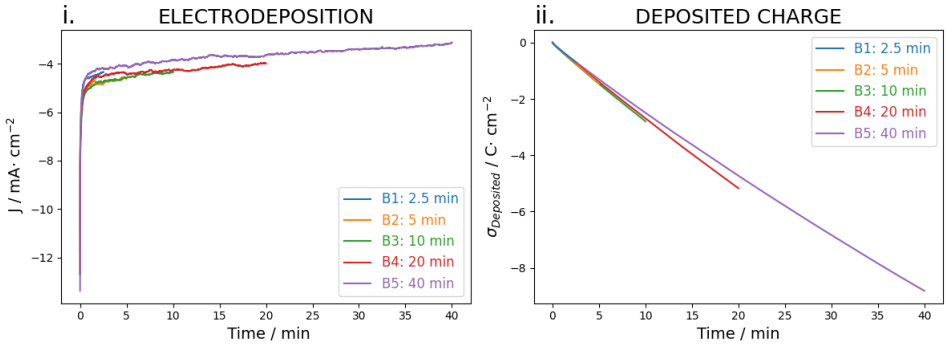


Figure 4.9: Electrodeposition J-t and σ-t characteristics for the deposited Cu thin films.

Further comparison of the final deposited charge density with the deposition calibration shows a perfect fit for samples B1 (2.5 min) to B3 (10 min), as figure 4.10 demonstrates. However, both B4 (20 min) and B5 (40 min) show deviations from the expected final deposited charge density ($\sigma_{\mathrm{Dep}}(t_f)$).

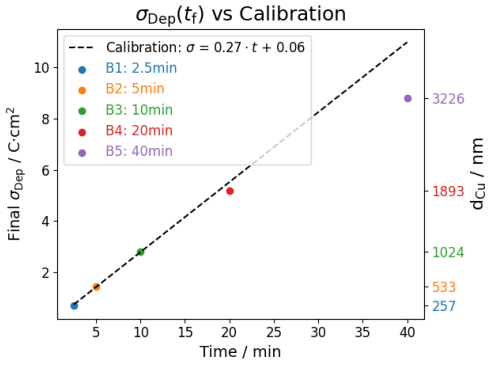


Figure 4.10: Comparison of final deposited charge density with prior calibration from section 4.1.

These deviations from the final expected deposited charge density is attributed to a reduction in precursor concentration in the electrolyte that slowly affects the deposition rate, as its highly visual for sample B5 (40 min) in figure 4.9 (ii) and 4.10. As the samples are deposited using the same electrolytic bath, so sample B5 (40 min) was deposited using a solution with 37.5 min of accumulated deposition time.

The resulting electrodeposited copper films and the obtained CuO photoelectrodes are presented in figure 4.11.

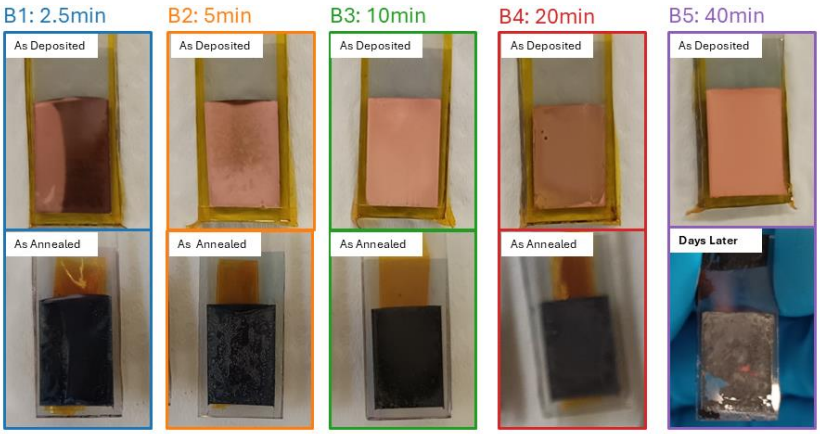


Figure 4.11: As deposited and as annealed photographs of the samples.

All electrodeposited films appear very homogeneous, as do the resulting CuO photocathodes. However, sample B5 (40 min) did not fully oxidize, as copper was visible through the back of the substrate. Additionally, sample B5 (40 min) started to disassemble and consequently it was not taken into photoelectrochemical characterizations.

4.2.3. Photoelectrochemical Characterization

The samples are photoelectrochemically characterized as described in section 3.3.4. Figure 4.12 presents the measured J_{photo}-V characteristics in plot (i) and the absolute generated photocurrent @ $0.5\ \text{V vs RHE}$ in plot (ii). As observed figure 4.12 (ii), the photocurrent density increases from sample B1 (2.5min) to B3 (10 min), further decreasing in sample B4 (20 min). The highest photocurrent density is from sample B3 with $|J_{\text{photo}}| = 1.44\ \text{mA} \cdot \text{cm}^{-2}$ @ $0.5\ \text{V vs RHE}$ and $V_{\text{onset}} = 0.74\ \text{V vs RHE}$, as listed in table 4.6.

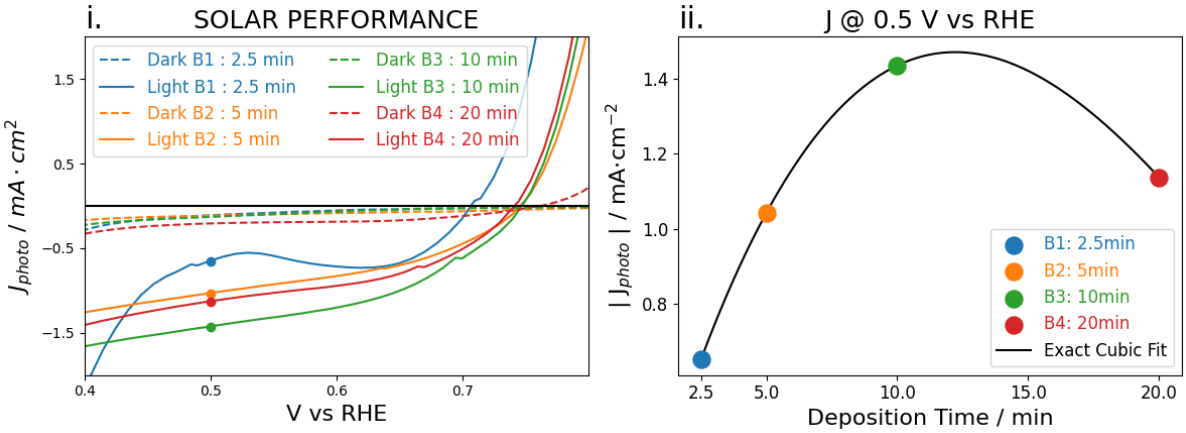


Figure 4.12: Photoelectrochemical results. **i.** J_{photo}-V performance. **ii.** J @ 0.5 V vs RHE as function of sample thickness/deposition time.

Sample	Deposition Time (min)	$\lvert J_{\text{photo}} \rvert$ @ 0.5 V vs RHE	V_{onset} vs RHE
B1	2.5	0.65	0.70
B2	5	1.04	0.74
B3	10	1.44	0.74
B4	20	1.14	0.74

Table 4.6: Photoelectrochemical results of the thickness study sample batch.

The thinner sample B1 shows a similar irregular J_{photo}-V characteristic to the observed in sample A1 (-0.33 V) of section 4.1.3, but without the high dark currents. Sample A1 was even thinner than B1, suggesting it is an effect of thinner samples. Analyzing figure 4.12 (ii), the exact cubic fit suggests the true optimal deposition time is around 12 min. Additionally, the measured photocurrent density for sample B2 (-1 V, 5 min) represents a 33.3% increment in photocurrent in relation to sample A3 (-1 V, 5min), outlining the improvement introduced by employing set-up B from figure 4.8.

The samples state before and after photoelectrochemical characterization is presented in figure 4.13. As it is perceived, sample B1 (2.5 min) shows strong signs of corrosion like A1 (-0.33V), which appears to be traceable to the odd behavior observed in figure 4.12 (i).

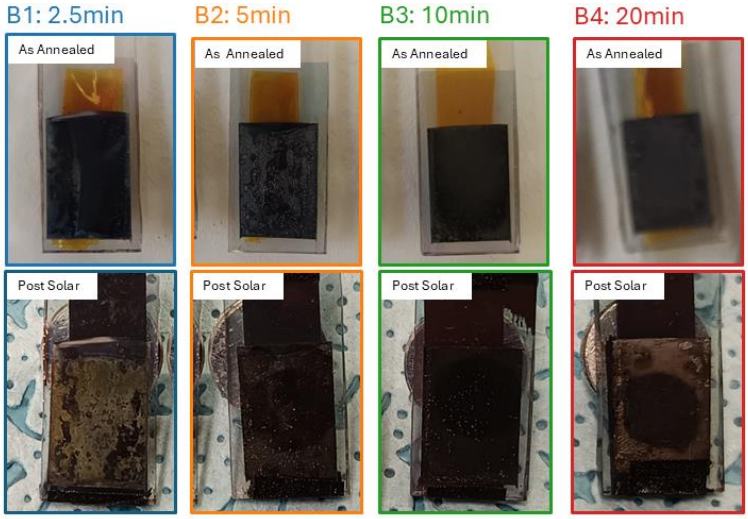


Figure 4.13: As annealed and post solar photographs of samples B1 to B4.

Figure 4.13 also suggests that sample B3 was the least degraded sample, as noticeable "solar marks" are visible in samples B2 and B4. Suggesting sample B3 provides not only the best photocurrent but also the best integrity after PEC characterization.

4.2.4. Morphological Characterization

The samples' morphology is assessed with scanning electron microscopy (SEM), as described in section 3.3.2. SEM images of the samples top view are presented at the 1 and 20 μm scales. In this study, the morphology of the CuO photocathodes is assessed before J_{photo}-V assessment. Analyzing figure 4.14 at the 20 μm scale, samples B1 (2.5 min) to B3 (10 min) morphologies appear highly homogeneous. However, samples B4 (20 min) and B5 (40 min) present different morphologies from the rest, even at the micron scale, where a porous and irregular grain morphology is observed.

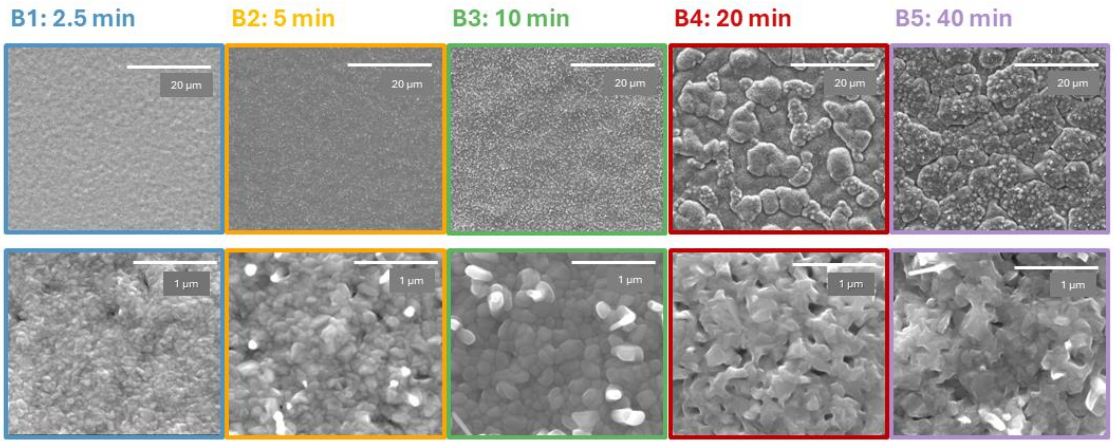


Figure 4.14: SEM micrographs of samples B1-B5 at the 20μm and 1μm range.

Analyzing the micron scale micrographs, samples B1 to B3 show similar grain morphology, with well-defined grain boundaries.

The grain size was measured with ImajeJ as detailed in section 3.3.2, and the measured grain population distributions are presented in figure 4.15. A biased accumulation effect to the left is very visual in samples B1 (i) and B2 (ii), deviating from gaussian behavior.

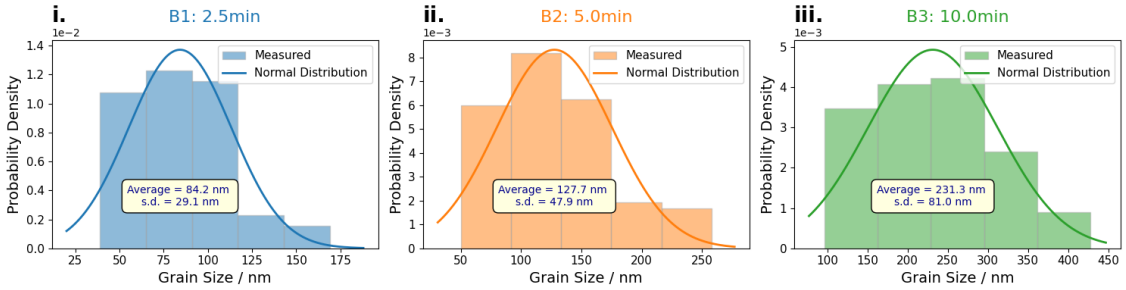


Figure 4.15: Probability density histograms for: i. Sample B1; ii. Sample B2; iii. Sample B3. Fitted normal distributions.

This deviation is related to the SEM resolution, in which distances below 30 nm, at the 1 μm scale, are difficult to visualize.

4.2.5 Structural characterization

Similarly to section 4.1.5, the samples were measured after photoelectrochemical characterizations via Raman spectroscopy. Figure 4.16 (i) contains the Raman spectra, where sample B5 (40 min) acts as a control because it did not undergo PEC characterization.

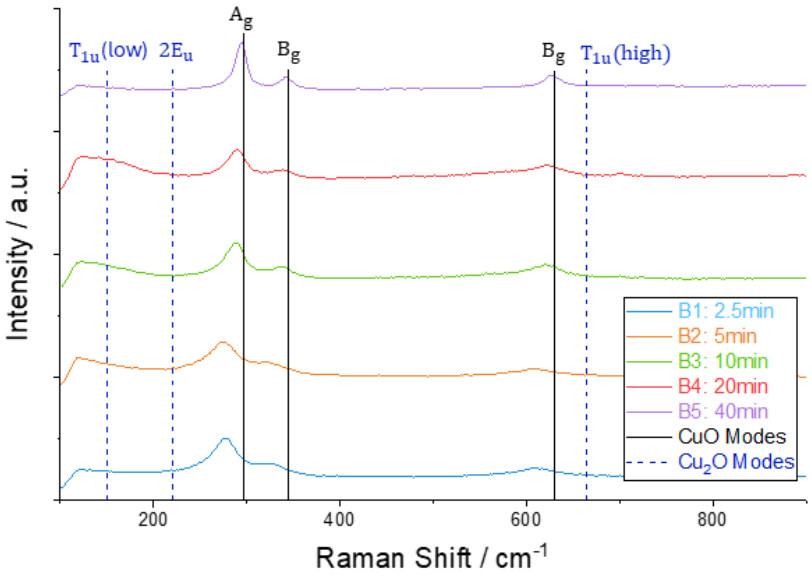


Figure 4.16: Batch Raman Spectra.

After photoelectrochemical characterization, none of the samples show any noticeable Cu_2O modes. However, some amorphous contribution from T_{1u} (low) Cu_2O modes seems to be present for B4 (20 min). The measured spectrum of B3 (10 min) shows a clear improvement in the structural integrity after PEC characterization of the samples in relation to the batch of section 4.1. Figure 4.17 outlines this improvement, attributed to the set-up B from figure 4.8 electrochemical cell geometry improvement, where a higher degree of crystallinity is observed and no Cu_2O mode is detected.

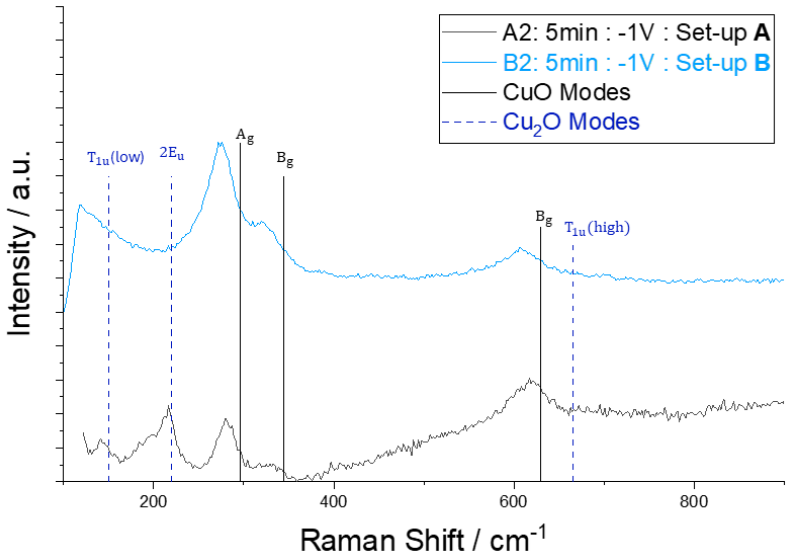


Figure 4.17: Comparison between the structure of the photocathodes after photo-performance characterization, between equivalent samples fabricated in different electrochemical set-ups.

The amorphous region in sample A3 around the B_g mode ($600\ cm^{-1}$), observed in figure 4.17, is also present in figure 4.7 but is not as perceivable because it is more compacted.

As outlined in section 4.1.5, and very visual in figure 4.16, the detected CuO modes present a clear shift to the left from the expected value. Additionally, this deviation seems to decrease with film thickness. As explained in section 3.3.1, deviations from the expected mode values ($\Delta\omega_{vib}$, equation 3.7), are related to strain through a proportion coefficient b [81,82]. For CuO, the b coefficient was not found in literature.

However, by plotting the quantity $\Delta\omega_{vib}$, it is possible to observe a decrease in strain with increasing thickness, as figure 4.18 shows. This inversely proportional relation is also reported in literature for the annealing of VO_2 with different film thicknesses [78].

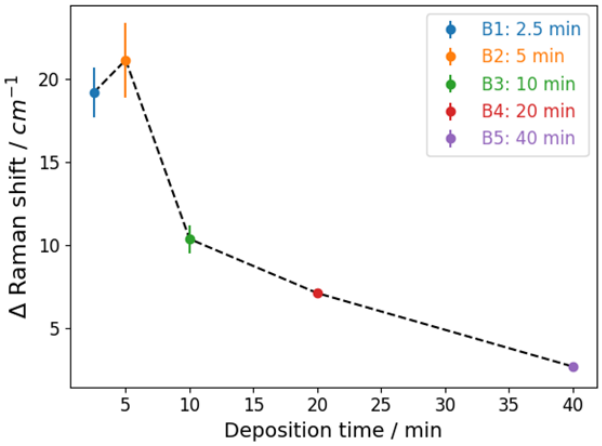


Figure 4.18: Strain as function of thickness, visualized through $|\Delta\omega_{vib}|$ vs deposition time relation.

A plausible explanation for this behavior is that strain is introduced by constriction at the FTO-Au and Cu interface and as result, crystalline planes farther away from this interface are not as constricted. Consequently, in thicker films, there is more un-strained material contributing to signal acquisition.

4.2.6. Optical Characterization

Optical characterization is carried as described in section 3.3.3, after photoelectrochemical characterization. Optical bandgap is determined by the interception of $|F(R) \cdot h\nu|^n$ lower plateau with the fitted regression at the transition slope of the Kubelka-Munk functions Tauc-plot, as illustrated in figure 4.19.

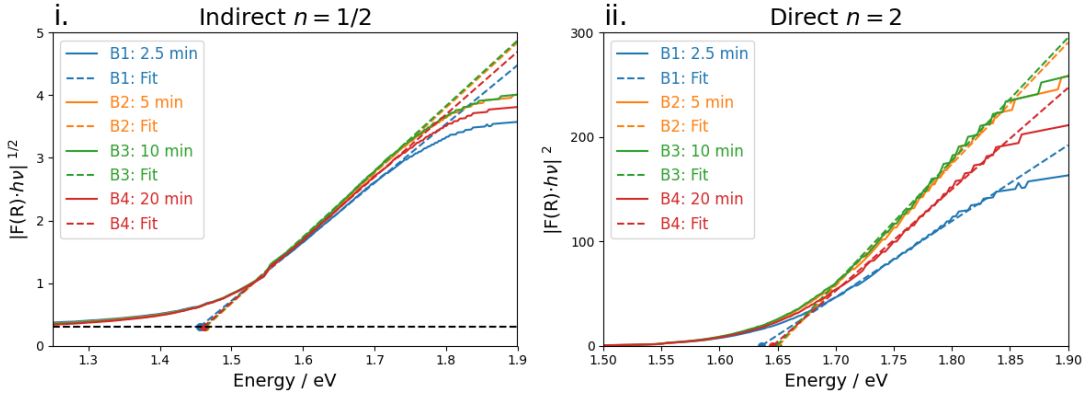


Figure 4.19: Fit visualization on Kubelka-Munk functions transition slope for: **i.** Indirect allowed transitions. **ii.** Direct allowed transitions.

Table 4.7 lists the obtained direct and indirect bandgap values, estimated with the linear regressions represented in figure 4.19.

		Indirect		Direct	
Sample	**Time**	E_g / eV	$\mu(E_g)$ / eV	E_g / eV	$\mu(E_g)$ / eV
B1	2.5	1.455	0.005	1.64	0.02
B2	5	1.464	0.005	1.65	0.02
B3	10	1.463	0.006	1.65	0.02
B4	20	1.461	0.005	1.65	0.02

Table 4.7: Summary of linear regression and bandgap calculation results. Note: E_{gap} uncertainty ($\mu(E_{gap})$) is calculated using error propagation formula considering the linear regression slope and intercept standard deviation.

The calculated indirect bandgaps contain each other's uncertainties except for the B1 (2.5 min) sample, which was severely damaged after photo-performance. All determined direct bandgaps contain themselves in their uncertainties: being equal to 1.65 eV, except for sample B1. These results indicate an indirect bandgap of $E_{\mathrm{g,indirect}}$ =1.46 eV and a direct one of $E_{\mathrm{g,direct}} = 1.65$ eV for the fabricated samples.

4.3. Conclusions

Throughout the development of this chapter, a scalable and inexpensive route for CuO synthesis was developed. The employed cyclic voltammetry study to the electrolyte, allowed to dive deeper into the FTO-Au/electrolyte electrochemical dynamics and to identify a suitable electrochemical window for copper electrodeposition.

The deposition potential and cell geometry were explored, allowing electrodeposition of copper thin films under optimized conditions, resulting in better performing CuO photocathodes with improved structural integrity after photoelectrochemical characterization, as demonstrated in sections 4.1.5 and 4.2.5.

The thickness of the raw CuO photocathodes was optimized to a theoretical CuO thickness $\mathrm{d_{CuO}} \approx 1.7\ \mu\mathrm{m}$, corresponding to an electrodeposition time of $10\ \mathrm{min}$ and photocurrent density of $\mathrm{J_{photo}} = 1.44\ \mathrm{mA \cdot cm^{-2}}$ @ $0.5\ \mathrm{V\ vs\ RHE}$. In literature, CuO photocathodes usually exhibit photocurrent densities bellow 1 mAcm^{-2} @ 0.5 V vs RHE. Although an optimal thickness is found, a 3rd order approximation to the measured data suggests an optimal deposition time of around $12\ \mathrm{min}$.

Although only the indirect CuO bandgap approaches the estimated ideal $E_g = 1.31\ \mathrm{eV}$ determined in section 2.3.2 for a Hematite-CuO pairing, the estimated direct bandgap approaches the ideal $E_g = 1.75\ \mathrm{eV}$ for a CuO-Si pairing.

5. CuO Photocathodes: Electrodeposition of Cupric Oxide (CuO) followed by annealing

This chapter describes Route B elaboration, described in section 3.2.2. This route enabled direct electrodeposition of CuO, avoiding the intermediary step of Cu electrodeposition and releasing the requirement of thermal annealing. This synthesis route consists in changing the electrolyte pH through the removal of boric acid and addition of sodium hydroxide (NaOH) for pH adjustment, leading to knew electrochemistry in the substrate/electrolyte interactions, as demonstrated through section 5.1. Additionally, throughout section 5.2 it is shown that adding steering to the solution led to visually different chemical species in the electrolyte that resulted in remarkably different electrodeposition characteristics, surface morphologies and structural integrities after photoelectrochemical characterization.

5.1. The effect varying pH

As stated in section 4.1, the electrochemical environment is highly dependent on pH. Varying the pH can severely affect the electrolyte conductivity, reactions redox potentials as Nernst equation dictates (equation 3.14) and which material phase is more favored during electrodeposition. Like in physical phase diagrams, a Pourbaix diagram indicates what chemical species are, and phase minimizes free energy and thus is more likely to form as a function of applied potential and pH [117].

Phase Selection with pH variation

The same precursor and reducing agent may be used to deposit different chemical species and phases. According to the Pourbaix diagram for copper, CuO is more stable than Cu for high pH values. Cuprous oxide (Cu_2O) is also favored by neutral to high pH environments but has a very narrow chemical window stability [117]. Although these diagrams don’t include ascorbic acid, citric agents have been reported to aid in copper oxides synthesis [77].

The various stages of the electrolyte as a function of pH during steering are illustrated in figure 5.1.

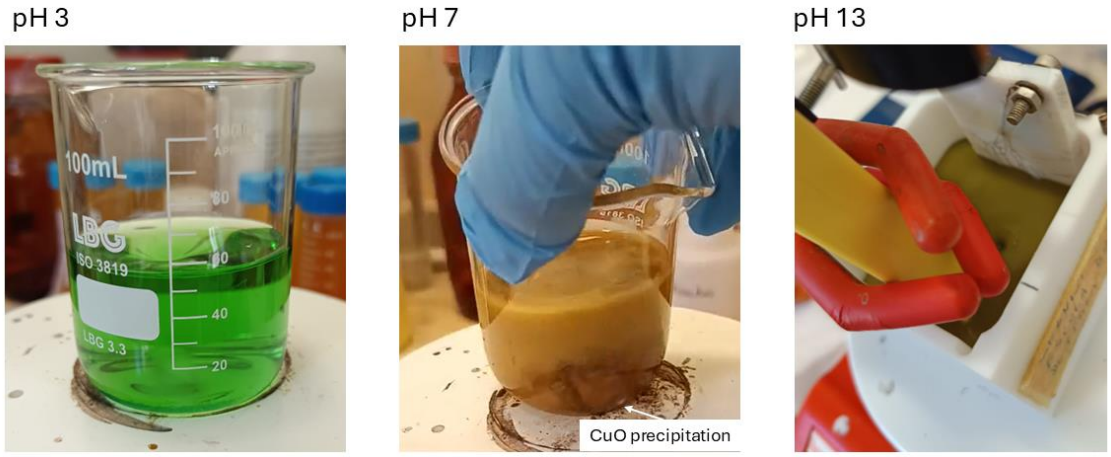


Figure 5.1: Solution photographs of the solution as a function of pH, during steering.

At pH 3 the solution looks very similar to the one employed in chapter's 4. With increasing pH, the solution acquires a lactic aspect, turning yellow at pH 7, then to olive green at pH>10, as shown in figure 5.1. Without steering, the electrolyte eventually loses the lactic aspect and becomes transparent, indicating that a metastable compound is formed with steering.

The black powder observed at pH 7 in figure 5.1, is a reaction between the solution and freshly added NaOH pellets, probably resulting in CuO particles precipitation given the color. This solution alteration may help find the main chemical species in the solution:

- CuOH (hydrated cupric oxide) exhibits a yellow color in aqueous solution [117].
- $Cu(OH)_2$ may also form at high pH 13 [117].

Another interesting observed effect during experimental trials was that by diminishing the precursor/reducing agent ratio the solution exhibits the yellow tone even at pH 13. Suggesting that the predominant compound at pH 7 for the 4:1 ratio is still the predominant compound at pH 13 for a 2:1 ratio. Consequently, the yellow compound seems to be favored by the higher concentrations of ascorbic acid.

Cyclic Voltammetry

To further investigate the electrochemical interactions between the substrate and electrolyte, cyclic voltammetry with fixed 20 mV/s scan rate is employed at different pH, with 400 rpm steering rate. For each CV a bare FTO-Au substrate is used to avoid changing the nucleation substrate between consecutive CVs. Figure 5.2 presents the CV results, for which the HER and Cu(I) reduction potentials are calculated using Nernst equation (see section 3.3.5).

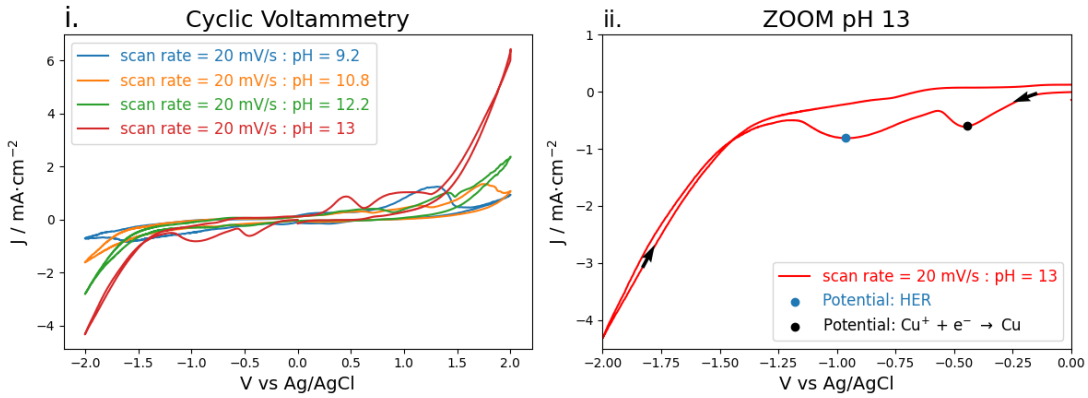


Figure 5.2: **i.** Cyclic Voltammetry with 20 mV/s scan rate as a function of pH, at 400 rpm. **ii.** Zoom in anodic region for pH 13 Cyclic voltammetry.

All cyclic voltammetry's show identic behavior from pH 9.2 to 10.8, predominantly showing capacitive behavior. For the CV at pH 13, which is the closest pH to the photoelectrochemical characterization conditions, two distinct peaks appear around HER and copper (I) reduction potentials in the cathodic region.

Afterwards, an electrodeposition is carried at $-1\mathrm{V\ vs\ Ag/AgCl}$ (HER potential) for different pH values ranging from 9 to 13, during 10min. This deposition time was chosen because in figure 5.2 (ii) CV the current density is only 1 $\mathrm{mAcm^{-2}}$. As presented in figure 5.3, clear CuO deposition is noticed for pH ≥12, with what seems a residual deposited CuO layer for pH values below this threshold.

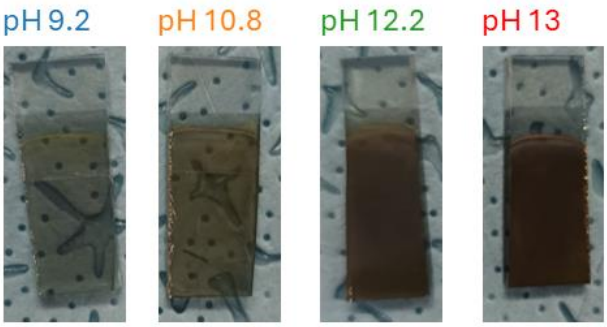


Figure 5.3: After CV samples, showing clear deposition above pH 10.8.

5.2. The Effect of Adding Steering during Electrodeposition

As previously discussed in section 5.1, adding steering to the electrolyte leads to quite different visual textures in the solution. The effect of applying steering to the solution at pH 13 can be visualized in figure 5.4.

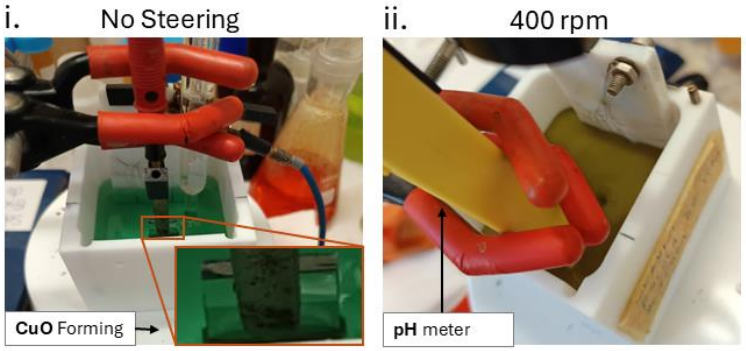


Figure 5.4: Steering Effect on the solution state. i. No steering effect, photograph during deposition. ii. Steering rate: 400 rpm.

This is a clear indicator of a metastable compound formation, which greatly influenced the deposition results Also, employing steering during electrodeposition has been reported to affect surface morphology, being a suitable route to micro and nano-structuring [118].

5.2.1. Direct CuO Electrodeposition

Two samples were electrodeposited at pH 13, with equal deposition time and applied potential, with and without steering during deposition. Sample F2 (No steering) is deposited after F1 (400 rpm), so the initial solution state changes from that of figure 5.4 (ii). During deposition. Figure 5.5 presents the electrodeposition characteristics.

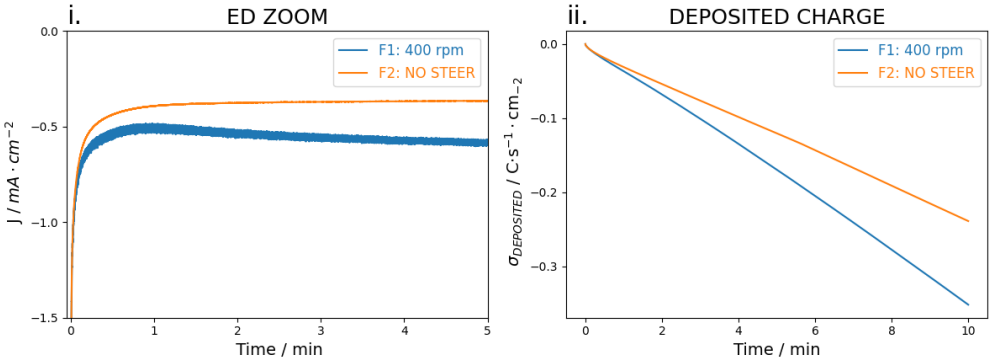


Figure 5.5: **i.** Zoom in $t \in [0,5]$min window for electrodeposition $J(t)$ characteristics. **ii.** $\sigma_{\mathrm{Dep}}(t)$ characteristics for $t \in [0,10]$ min.

Sample	Deposition time / min	Deposition Potential / V vs Ag/AgCl	Steering Rate / rpm
F1	20	-1.5	400
F2	20	-1.5	0
$T_{\mathrm{station}} = 20$℃.			

Table 5.1: Deposition conditions for batch fabrication.

Analyzing figure 5.5 (i), both samples show similar nucleation stages but rather different characteristics afterwards. Sample F2 (No steering) shows typical film deposition $J(t)$ characteristics, with an approximately constant steady state current density after nucleation. On the other hand, sample F1 $(400\ \mathrm{rpm})$ shows a minimum absolute current density value around $t = 54\mathrm{s}$, which then further increases in absolute value. In a potentiostatic deposition, as the electric field is fixed through voltage, for current density to increase the surface area must be increasing as well. Also, by inspection of figure 5.2 (ii) it is immediate to confirm that these samples are deposited in a potential region beyond HER potential which justifies the strong noise observed in sample F1$(400\ \mathrm{rpm})$. Noticeable, this "noise effect" is much weaker in sample F2 (No steering), which has a smooth deposition curve.

5.2.2. Photoelectrochemical characterization

After electrodeposition, both samples go through the annealing process described in section 3.1.4, as a way of ensuring pure CuO phase, as structural characterization is not performed prior to photoelectrochemical characterization. The photoelectrochemical characterization was performed as described in section 3.4.5. Figure 5.6 presents the measured J_{photo}-V characteristics, under dark and simulated sunlight illumination conditions. The samples show very different photoelectrochemical behavior. Sample F2 (No steering) shows irregular photocurrent density, like samples A1 and A2, exhibiting very high dark currents but also regions where dark current even surpasses photocurrent – with similar current density transition around Cu (II) reduction potential.

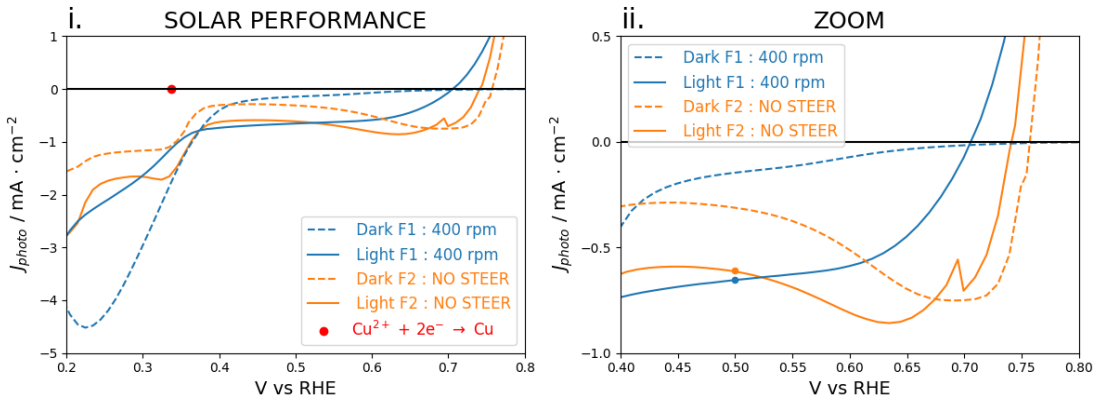


Figure 5.6: i. Photoelectrochemical J-V for $V \in [0.2,0.8]$ V vs RHE. **ii.** More stable chemical window $V \in [0.4,0.8]$ V vs RHE.

Sample F1 (400 rpm) shows typical photocurrent density up until potentials near Cu (II) reduction potential, where after this potential it shows an almost ohmic behavior under illumination and a very high dark current density maximum near 0.2 V vs RHE.

Table 5.2 summarizes the photoelectrochemical results for these samples, showcasing that sample F1 achieved the best photocurrent and lowest onset potential.

Sample	Steering Rate / rpm	$\lvert J_{photo} \rvert$ @ 0.5 V vs RHE / mA·cm^{-2}	V_{onset} / V vs RHE
F1	400	0.654	0.706
F2	0	0.609	0.741

Table 5.2: Summary results for F1 & F2 photo-response results.

Posterior to characterization, the samples integrity shows clear visual differences, as presented in figure 5.7. Sample F1 (400 rpm) seems better preserved than any other developed CuO photocathode.

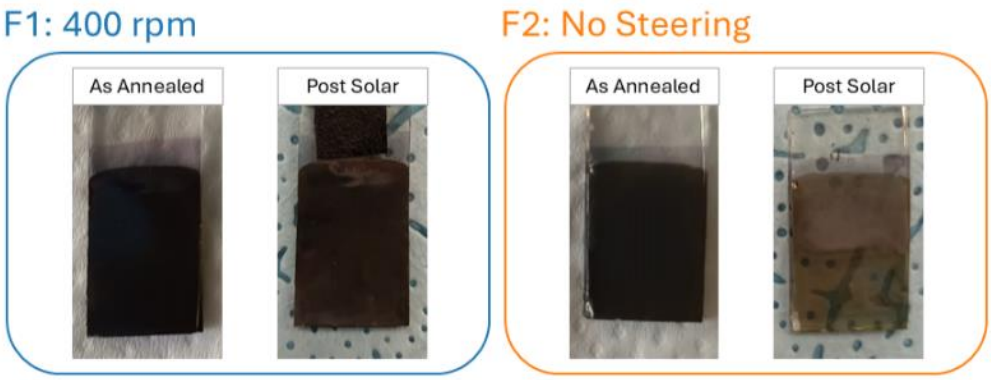


Figure 5.7: Before and after photoelectrochemical characterization photographs of samples F1 and F2.

Unlike F1, sample F2 shows clear degradation in all the areas that contacted the electrolyte. Consequently, besides a superior photo-performance, sample F1 also seems intrinsically more stable than F2.

5.2.3. Morphological Characterization

The morphology of the fabricated samples F1 (400 rpm) and F2 (No steering) is investigated using scanning electron microscopy (SEM), as described in section 3.3.2. Micrographs at $1\ \mu m$ and $100\ \mu m$ scales are presented. Unlike the previous sections, for this sample batch, morphology is assessed both prior and after photoelectrochemical characterization, enabling for evaluation of the photoelectrochemical trial effect on morphology.

Before Photoelectrochemical Characterization

As expected by section 5.2.1 analysis, figures 5.8 and 5.9 demonstrate quite different morphologies for sample F1 and F2. Figure 5.8 presents the micrographs for sample F1, for which two very different morphologies are visualized at the 100 µm scale: Zone 2 with a very continuous film like morphology, and Zone 1 with a porous micro-structure that resembles a coral rift.

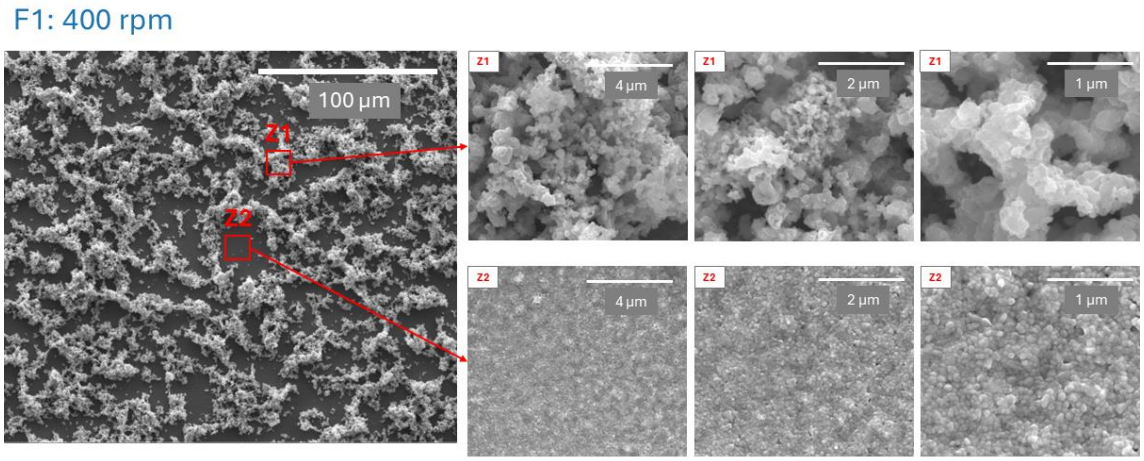


Figure 5.8: SEM micrographs of sample F1.

The observed grain morphology in Zone 2 (Z2) is very similar to those of section 4.2.4, while zone 1 (Z1) shows quite a unique, and highly porous morphology at the micron scale. This porosity inside Z1 may have risen because of hydrogen evolution during deposition. On the other hand, sample F2 shows a very predominant film like morphology as figure 5.9 demonstrates. In Zone 2 at the micron scale, the film is much less regular than that of sample F1. Subsequently, although it also exhibits (in much less proportion) micro-structures that resemble figure 5.8 zone 2 micrographs, it seems less porous than those of sample F1 ($400\ \mathrm{rpm}$). These residual microstructures are most likely related to the initial state of the deposition electrolyte, that was used after F1 electrodeposition.

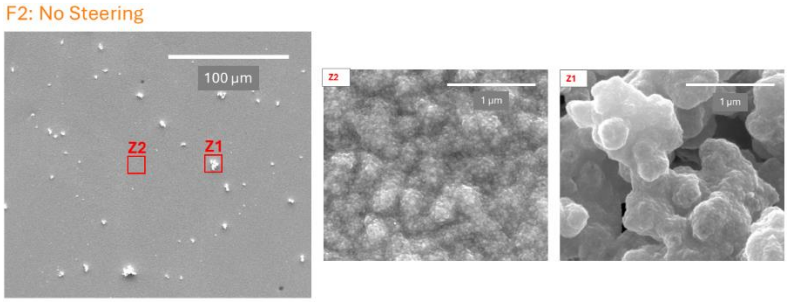


Figure 5.9: SEM micrographs of sample F2 (No Steering).

After Photoelectrochemical Characterization

Figure 5.10 outlines SEM micrographs for both samples, in an annealed and post PEC characterization stages.

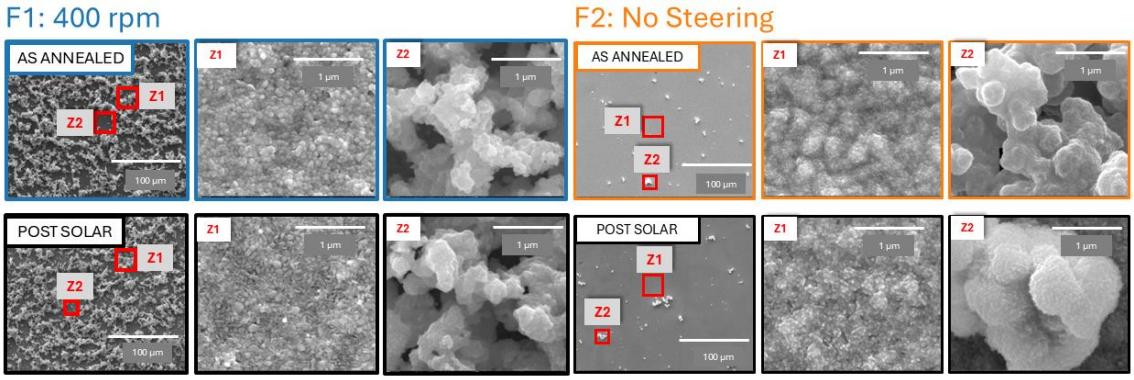


Figure 5.10: As annealed and post solar measurements SEM images of samples F1 and F2. Maro images: x10^3 magnification – 100 µm; Micro images: x10^5 magnification – 1 µm.

As it can be seen from figure 5.10 inspection, the film like morphology of Zone 2 (Z2) shows corrosion in both samples, as the grains appear more “spiked” prior to PEC characterization. The steering induced micro-structure shows no sign of corrosion in sample F1 (400 rpm), while minimal corrosion is observed in sample F2 (No steering).

Figure 5.11 contains EDX spectrums for Zone 1 (film morphology) in plot (i) and for Zone 2 (micro-coral morphology) in plot (ii). The green boxes outline copper (Cu) and oxygen (O) characteristic x-ray energies intensity, while the black box outlines tin (Sn, present in substrate) x-ray energies intensity.

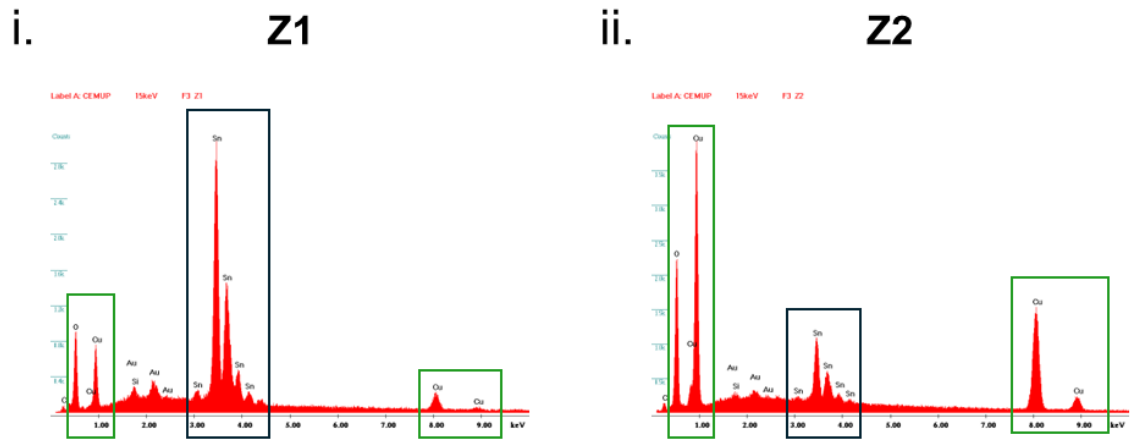


Figure 5.11: EDS spectrum for samples of different zone types. Black box: Sn containing energy peaks; Green box: O and Cu containing energy peaks.

As observed by comparison of plots (i) and (ii), the relative intensity between tin (Sn) and copper/oxygen (Cu/O) x-ray energy peaks is much higher in Z1 than in Z2. Additionally, EDX measurements before photo-performance assessment demonstrates higher Cu/O ratios in relation to tin (Sn) in both zones. The former concludes that the remaining copper/oxygen content in Z2 is much higher than that of Z1, after photoelectrochemical characterization. Consequently, EDX analysis suggests that Z2 (micro-coral like) is intrinsically more stable than Z1 (film like).

The trend in figure 5.11 between the different zones is observed in both samples. As figure 5.10 also demonstrates, corrosion seems much stronger in the film like zone of sample F1 in relation to the steered induced microstructure. Consequently, this enhanced stability of Zone 2 is attributed to the similarity between the electrochemical environment (pH 13, hydrogen evolution) and the photoelectrochemical characterization conditions.

5.2.4. Structural Characterization

Raman spectroscopy is employed for accessing the samples' corrosion state after solar measurements, as described in section 3.3.1 and performed in sections 4.1.5 and 4.2.5. Figure 5.12 presents the measured Raman spectrums for samples F1 (400 rpm) and F2 (No Steering).

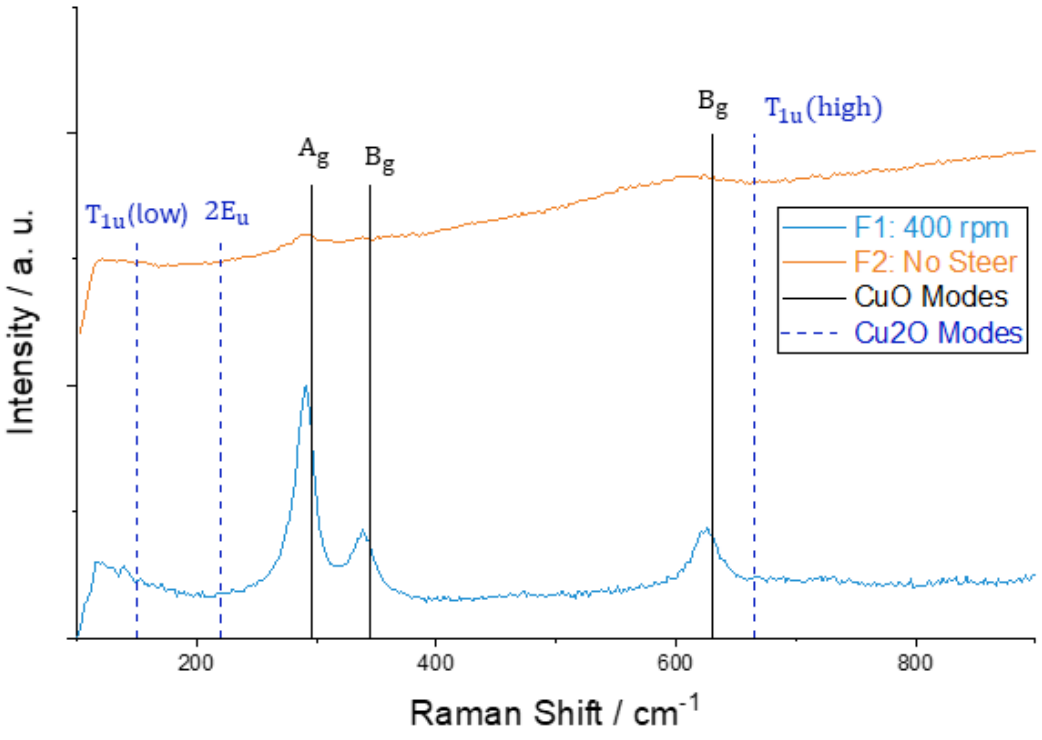


Figure 5.12: Raman spectrums for F samples. **i.** Post solar measurements F1 and F2 spectrums; **ii.** As annealed and post solar spectrum of F2 sample.

Sample F1 (400 rpm, blue) spectrum presents very sharp, defined peaks, even after the photoelectrochemical measurements. Not only it presents the best structural integrity after PEC characterization, as it demonstrates much smaller deviations ($\Delta\omega_{\mathrm{vib}}$) from the expected Raman shift peak value (ω_{vib}) than the fabricated photocathodes by Route A (electrodeposition of copper followed by annealing). As such, these samples are less strained than the ones from chapter 4. Consequently, much of the induced strain in chapter 4 samples must be related to copper thermal expansion and Cu→CuO phase transition. Unlike F1, sample F2 (No steering, orange spectrum) is very amorphous and barely presents any CuO after photoelectrochemical measurements.

5.2.5. Optical Characterization

The samples are characterized as described in section 3.3.3, and bandgap is determined using Tauc-plots of the Kubelka-Munk functions. Figure 5.13 presents the calculated Kubelka-Munk functions and the carried fits to the transition slope, while table 5.3 lists the calculated bandgap values, as in section 4.2.6.

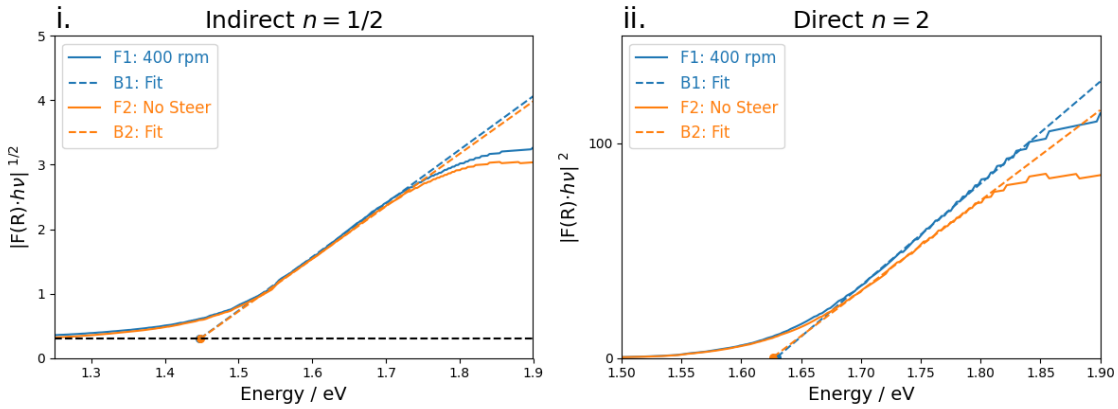


Figure 5.13: Tauc plots using Kubelka-Munk functions for indirect ($n = 1/2$) and direct ($n = 2$) transitions.

		Indirect Bandgap		Direct Bandgap	
Sample	**Steering / rpm**	E_g / eV	$\mu(E_g)$ / eV	E_g / eV	$\mu(E_g)$ / eV
F1	400	1.447	0.005	1.63	0.01
F2	0	1.448	0.005	1.63	0.01

Table 5.3: Fit results summary and respective calculated indirect and direct bandgaps.

Both films exhibit a direct bandgap of 1.63 eV and an indirect one of 1.45 eV, for which the difference observed for the indirect bandgap values is absorbed in their uncertainties.

Comparing these bandgap values and respective uncertainties with that of chapter 4, it is not possible to say the samples have different bandgaps because there's not enough statistical evidence sustaining that conclusion. As such, both syntheses are considered to result in similar bandgap value. Table 5.4 presents the average of all determined direct and indirect bandgap values and their uncertainty, taken to be their standard deviation.

	E_{gap} / eV	$\mu(E_{gap})$ / eV
Indirect Bandgap	1.456	0.007
Direct Bandgap	1.64	0.01

Table 5.4: Estimated bandgaps and uncertainties considering all samples from chapter 4 and 5.

5.3. Conclusions

Utilizing the same precursor and reducing agents of chapter 4, it was possible to induce direct cupric oxide (CuO) electrodeposition with a variation in pH. Additionally, by adding steering during electrodeposition, a metastable compound forms that enabled the direct deposition of CuO during hydrogen evolution. This steering effect was also correlated with a change in electrodeposition characteristics ($J(t)$), enabling micro-structuration during deposition that resulted in a very porous morphology.

The resulting CuO photocathode with steering during deposition achieved a photocurrent density of 0.65 $mAcm^{-2}$ @ 0.5 V vs RHE, with enhanced structural integrity in relation to any of the previously fabricated CuO photocathodes. This enhanced stability is attributed to the similarity between the deposition electrochemical environment and the photoelectrochemical characterization environment (high pH with H_2 evolution). Additionally, this photocathode structure showed minimal strain in relation to chapter 4 photocathodes, attributed to the different initial annealing phases (Copper (chap. 4) vs CuO (chap. 5) as initial phase). Furthermore, the enhanced stability for this photocathode suggests that the induced morphology during electrodeposition is a very promising route for stabilizing these photocathodes surfaces during PEC operation.

The estimated bandgaps for these synthesis approaches show no significant deviation from the determined in chapter 4. For bandgap tuning assessment, investigation on the deposition electrolyte precursor/reducing agent ratios and annealing conditions should be performed.

6. Hematite-CuO Tandem Heterojunctions

Following the successful development of synthesis routes for CuO photocathodes fabrication, it was possible to incorporate CuO photocathodes by "Route A" and Hematite to form a tandem heterojunction, as detailed in section 3.2.3. The formed heterojunctions have a different structure to that of a tandem PEC cell, resulting in different energy diagrams. Nonetheless, coupling the two materials may still improved performance. The copper electrodeposition on the FTO-Au and FTO-Fe substrates is analyzed in section 6.1. Additionally, the photo-response of the fabricated junctions is presented in section 6.2, comparing the performance to an equivalent bare-hematite photoanode. Finally, the morphology and structural integrity of the samples is discussed through sections 6.3 and 6.4.

6.1. Copper (Cu) Electrodeposition

The electrodepositions of copper for the junction's fabrication are conducted as in chapter 4, using the optimized deposition potential and cell geometry but a deposition time of 5 minutes is employed at $T_{\text{station}} = 20℃$. Figure 6.1 presents the electrodeposition characteristics. Copper electrodeposition on the FTO-Au substrate is conducted first and undergoes annealing. Afterwards, iron is deposited via IBD on top of J1: FTO and J2: FTO-Au-CuO, enabling posterior electrodeposition of copper in J1: FTO-Fe.

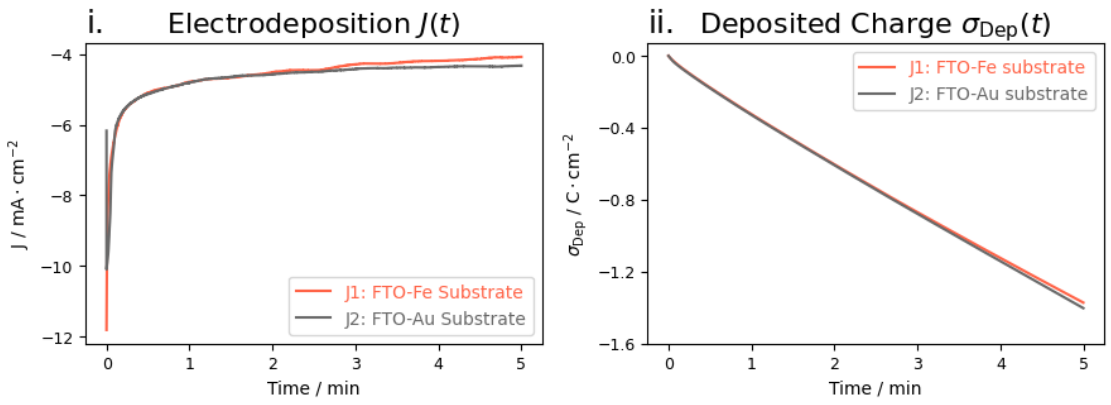


Figure 6.1: **i.** Electrodepositions $J(t)$ characteristics for both substrates. **ii.** Deposited charge density $\sigma_{\text{Detp}}(t)$ characteristics.

The deposition charge density characteristics are almost the same, as illustrated in figure 6.1 (ii). Although in copper electrodeposition (plot (i)), the quasi-plateau of J1: FTO-Fe is not as stable as in J2: FTO-Au deposition (plot (i)). However, the nucleation substrate is different, and this might result in different grain morphologies and crystalline orientations

of the copper films. Subsequently, the resulting junctions undergo annealing (as in section 3.2.2.2), resulting in the following heterojunction configurations:

- J1: FTO-α-Fe_2O_3-CuO
- J2: FTO-Au-CuO- α-Fe_2O_3

Figure 6.2 demonstrates the fabricated structures before and after annealing, for the different configurations.

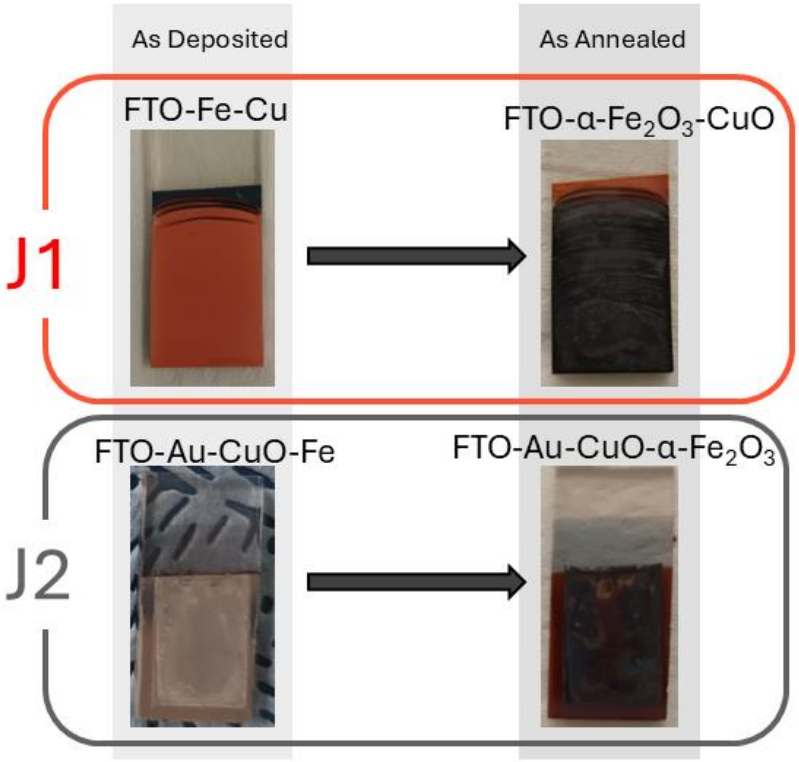


Figure 6.2: Pictures of the fabricated samples before and after annealing.

6.2. Photoelectrochemical Characterization

Photocurrent density-voltage (J_{photo}-V) under dark and simulated sunlight illumination of the fabricated heterojunctions are presented in figure 6.3 (i) and (ii). Both junctions are measured under front illumination conditions, as described in section 3.3.5.

As thoroughly explained throughout section 1.2.1 and chapter 2, light incision should pass through the semiconductors in decreasing bandgap order. In case of J1 (FTO-α-Fe_2O_3-CuO), the front-illumination condition imposes light to pass firstly on CuO and later hematite (α-Fe_2O_3), which is bad device configuration regarding photoconversion and justifies the clear difference between J1 and J2 photocurrent densities.

As figure 6.3 demonstrates, these heterojunctions can be made to act as either a photocathode or photoanode depending on the applied bias.

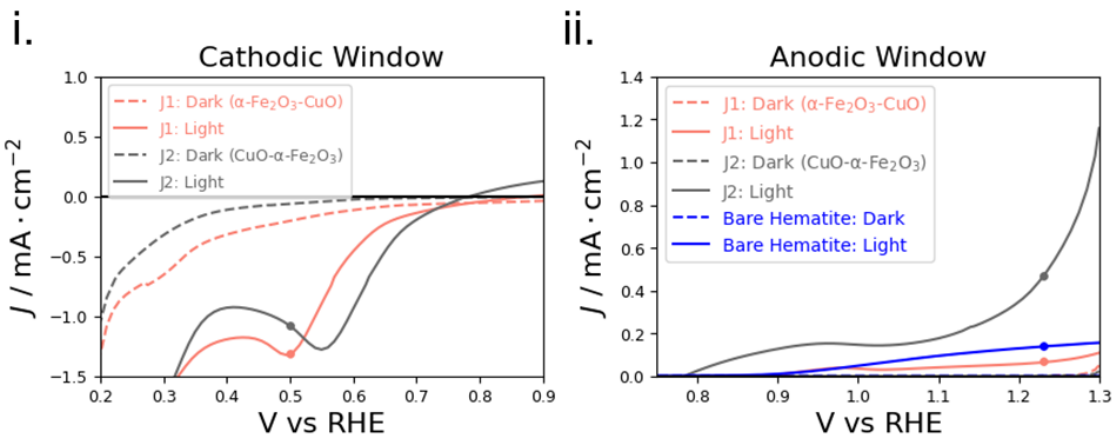


Figure 6.3: **i.** Cathodic electrochemical window for the fabricated heterojunctions. **ii.** Anodic electrochemical window of the fabricated junctions.

Table 6.1 lists the measured photo current density at both anodic and cathodic sites, as well as onset values.

Sample	Configuration	J @ 0.5 V vs RHE	J @ 1.23 V vs RHE	V_{onset} vs RHE
J1	FTO-α-Fe_2O_3-CuO	-1.31	-0.068	0.9
J2	FTO-Au-CuO-α-Fe_2O_3	-1.08	-0.47	0.785
Bare Hematite	FTO-Fe_2O_3	-	-0.141	0.9

Table 6.1: Summary results for the heterojunctions photoelectrochemical characterization.

Photoanode Electrochemical Window

For applied bias above each heterojunction V_{onset}, both J1 and J2 act as photoanodes. Remarkably, even with CuO absorbing most photons above hematite's bandgap in J1, the junction was still capable of achieving around 50% of the photocurrent density to that of bare hematite, plot (ii). Regarding J2 (FTO-Au-CuO-α-Fe_2O_3), with a correct configuration for light absorption it was possible to obtain around 330% increase of J @ 1.23 V vs RHE for this junction with a shift in the onset potential from 0.9 to 0.785 V vs RHE, in relation to the bare hematite configuration.

Photocathode Electrochemical Window

For applied bias below each heterojunction V_{onset}, both J1 and J2 act as photocathodes. Unlike the photoanode region, the current density under illumination in this electrochemical window shows photocurrent maximum near Cu(I) reduction potential.

This behavior was also observed for the thinner CuO photocathodes of chapter 4. Additionally, the dark cathodic currents are also observed, starting before Cu(I) reduction potential. This behavior is attributed to the introduction of hematite, as it was not observed for equivalent bare CuO photocathodes of chapter 4. One of hematite's limitations is the low carrier diffusion lengths, as outlined in section 1.2.3. Consequently, although the measured cathodic $J_{\text{photo}}@\ 0.5\ \text{V vs RHE}$ is higher than the bare CuO photocathodes, it is most likely related with photo corrosion.

Figure 6.4 shows the visual integrity of the samples after photoelectrochemical characterization. Sample J2 segregated from the substrate after washing.

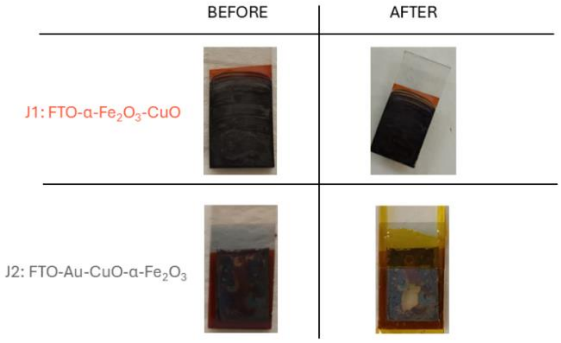


Figure 6.4: Sample photographs after photoelectrochemical characterization.

6.3. Morphological Characterization

The morphology is inspected after photoelectrochemical characterization via scanning electron microscopy. Figure 6.5 contains micrographs for J1 and J2 macro and micron scales. Additionally, sample B2 (5 min) micrographs from section 4.2.4 are also presented for comparison.

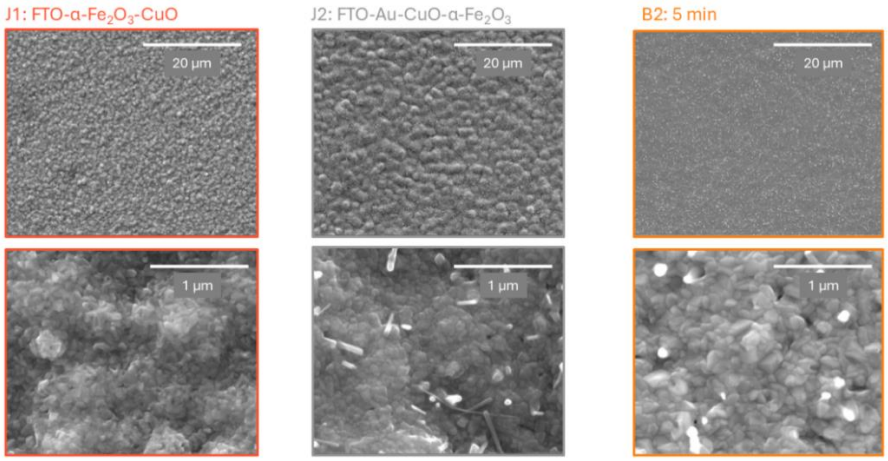


Figure 6.5: SEM micrographs of the fabricated heterojunctions, after photoelectrochemical characterization. Micrographs for sample B2 (5min) from section 4.2 are included for CuO morphology comparison.

As illustrated in figure 6.4 (section 6.2), the center of J2 junction segregated from the junction. As such, SEM images were acquired the remains in the center, represented in sample J2 (FTO-Au-CuO-α-Fe_2O_3) micrographs. Attending to the $20\,\mu m$ scale, it is possible to visualize some corrosion in sample J2.

Surprisingly, the grain morphology observed in sample B2 is preserved in both samples J1 (FTO-α-Fe_2O_3-CuO) and J2 (FTO-Au-CuO-α-Fe_2O_3) after photoelectrochemical characterization, although some deformation is observed. Analyzing sample J1 micrograph, this is a remarkable improvement in relation to raw depositions conditions, where all micrographs from section 4.1.4 present what seems to be a strongly corroded morphology at the micron scale.

6.4. Structural Characterization

The structural integrity of the heterojunctions is assessed via Raman spectroscopy, like in previous chapters. Subsequentially, the acquired Raman spectra for the different acquisition zones are represented in figure 6.5.

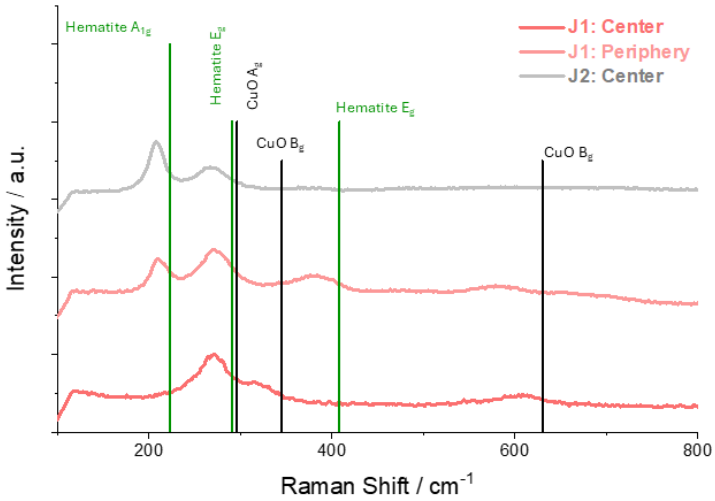


Figure 6.6: Acquired Raman spectrums of samples J1 and J2, at different regions for layer composition assessment.

In the case of J1 (FTO-α-Fe_2O_3-CuO) the acquired spectrum at the samples' center does not show any clear hematite mode, but the acquisition at the samples top periphery enabled detection of typical hematite modes. Regarding J2 (FTO-Au-CuO-α-Fe_2O_3), the typical hematite Raman modes are detected, but in this case, there is no exposed CuO at the periphery so it was not detected.

Comparing the measured hematite modes in samples J1 and J2, sample J2 does not show the higher E_g mode.

6.5. Conclusions

The incorporation of Fe_2O_3 and CuO into a heterojunction revealed promising results, even without a ohmic insulator between the semiconductors. The fabricated junctions were able to behave as both a photocathode and a photoanode, although the photocathodic response shows photocurrent maximum that is probably related with photo-corrosion of the CuO layer.

Although sample J2 (FTO-Au-CuO-α-Fe_2O_3) segregated after photoelectrochemical characterization, it was the best performing sample, resulting in a x3.33 increase in photocurrent density (0.47 $mAcm^{-2}$ @ 1.23 V vs RHE) and a lowering in the onset potential of 115 mV vs RHE, in relation to bare hematite (0.141 $mAcm^{-2}$ @ 1.23 V vs RHE).

Remarkably, sample J1 (FTO-Fe_2O_3-CuO) achieved similar photocurrent densities to the bare hematite sample, even with an unsuitable configuration for light incision. This means that sample J1 was able to achieve similar performance to that of bare hematite, even with much less incident radiation on the hematite layer (which limits photoconversion), showcasing the potential of this configuration.

Like the CuO photocathodes developed in chapter 4, the resulting structure after photoelectrochemical characterization does not show any Cu_2O phase. Additionally, the CuO grain of J1 (FTO-Fe_2O_3-CuO) shows no sign of corrosion, showing similar morphology to equivalent CuO photocathodes of chapter 4.

7. Conclusions and Future Work

This work focused on developing photoelectrodes for photoelectrochemical tandem cells, with the goal of combining a photoanode (n-type) and a photocathode (p-type) metal-oxide based semiconductors.

Numerical modelling for solar-to-hydrogen conversion was carried, for which according to results, the maximizing efficiencies indicate that the reported bandgap range of CuO offers promising advantages for incorporation in a photoelectrochemical tandem device if paired with a hematite photoanode (up to ~16.7%) or a silicon solar cell (up to ~21%) under near ideal conditions, with still considerable efficiencies even when high photoconversion losses are present. In addition, the implemented algorithm for solar-to-hydrogen efficiency allowed to simulate an unreported hybrid 3-junction tandem PEC-PV-EC system that by a parallel electrical connection implementation, re-shaped the maximum solar-to-hydrogen efficiency region from a single point into a straight line (more than 1 bandgap combination outputs the maximum efficiency), broadening the possible bandgap combinations. This broadening was found to enable S-Q limit efficiencies above 18% for the pairing of wide bandgap materials like WO_3 or TiO_2, with a resulting hydrogen yield above 40% in relation to the incident solar constant (100 $mWcm^{-2}$).

Following the simulation results motivation, two synthesis protocols were designed to obtain CuO photocathodes based on the electrodeposition technique. In the first approach (Route A), the CuO photocathodes were obtained by direct electrodeposition of Cu and subsequent thermal annealing, inducing the metal (Cu) to metal-oxide (CuO) phase transition. This process optimization was accurately performed by exploring electrodeposition parameters like deposition voltage, cell geometry and deposition time (CuO film thickness). Two groups of samples were fabricated and studied by varying: (1) the electrodeposition applied voltage from -0.33 V to -1.5 V vs Ag/AgCl, and (2) electrodeposition times from 2.5 min to 40 min. By combining morphology, structural and optical characterization with the evaluation of photocurrent density output, the best solar-performing photocathodes were clearly identified under photoelectrochemical testing with simulated sunlight. The improvement in the electrodeposition cell geometry led to photocurrent density of 1.04 $mAcm^{-2}$ @ 0.5V vs RHE, leading to a 33.3% improvement in equivalent samples, in relation to raw deposition conditions (0.78 $mAcm^{-2}$ @ 0.5 V vs RHE). No evident Cu_2O traces were identified after photoelectrochemical performance studies. Furthermore, the highest photocurrent density was obtained for a 10 min

electrodeposition time at –1 V vs Ag/AgCl applied voltage, reaching 1.44 mA·cm⁻² @ 0.5 V vs. RHE with 0.74 V vs RHE V_{onset}.

For the second synthesis protocol (Route B), we were able to directly electrodeposit the oxide-CuO via a pH variation (fixing the reagents and electrolyte composition of the first approach). During this method's development it was found that incorporating steering during the electrodeposition led to a different solution state, ultimately leading to highly porous micro-coral-like morphology. Although the resulting photocathodes with this method resulted in lower photocurrent densities (0.65 $mAcm^{-2}$ @ 0.5 V vs RHE), they have led to a high degree of crystallinity and structural integrity after photoelectrochemical characterization, when compared with the photocathodes obtained by the first approach (Route A). This improvement was attributed to the close similarity between the electrochemical deposition environment and the photoelectrochemical characterization environment (high pH with H_2 evolution), as well to the enhanced surface area of the photocathodes obtained by this method.

Finally, the successful development of suitable CuO photocathode fabrication enabled the incorporation of this material into hematite-CuO heterojunctions, resulting in promising prototypes of tandem PEC cells by pairing n-type and p-type photoelectrodes, thereby reproducing the numerical simulation environment. Although the fabricated junctions do not follow the exact architecture of a tandem photoelectrochemical cell presented in the introduction, the implementation of CuO led to a ~330% photocurrent density improvement (0.47 $mAcm^{-2}$ @ 1.23 V vs RHE) compared to that of bare hematite (0.141 $mAcm^{-2}$ @ 1.23 V vs RHE), as well to a lowering in the onset of 115 mV vs RHE: resulting in both a superior photoconversion and a lowering in the activation overpotential for OER.

Accordingly, this work demonstrates promising results for CuO photocathodes fabrication as well as this material implementation into hematite-CuO heterojunction photoelectrodes.

7.1 Future Work

The development CuO photocathodes (p-type) was conducted with FTO (n-type) as a TCO contact. The junction of these two oxides leads to a depletion field that favours hole transport into the electrolyte and redirecting electrons to the counter electrode, which opposes the natural flow of charge induced by the semiconductor/electrolyte built-in field, and is behind the strong anodic photo-response observed throughout chapters 4 and 5. Because of this, a p-typte TCO like NiO should act as TCO contact, favouring hole

extraction to the counter-electrode. After this study, typical enhancement techniques like doping, passivating and co-catalyst deposition should be performed.

Subsequently, “Route B” presented in chapter 5 was just the beginning, as no optimizations were conducted besides the demonstrated work. The relationship between the electrochemical environment and resulting morphology and properties should be deeply studied, as this work suggests that is a highly promising route for achieving long-term stability for these photocathodes. This route could and should be tested as a functionalization of the “Route A” CuO photocathodes surface.

Regarding the hematite-CuO heterojunctions, an intermediary ohmic layer should be placed between the hematite and CuO to act as both recombination layer and an insulator, so the built-in electric field at the electrolyte/semiconductor interface is not opposed by the electric field generated between the n and p semiconductors. Additionally, the FTO-α-Fe_2O_3-CuO junction should be studied under back illumination conditions to enhance light absorption.

8. References

1. IEA (2025), Global Energy Review 2025, IEA, Paris https://www.iea.org/reports/global-energy-review-2025, Licence: CC BY 4.0.
2. U.S. Department of Energy, “Hydrogen and Fuel Cell Technologies Office”.
3. Roel Van de Krol, Michael Gratzel, “Photoelectrochemical Hydrogen Production”, Springer (2012).
4. Julia Marcinkowska, “European union and green hydrogen overview” (2025).
5. Caroline Willich, “Hydrogen as an Energy Carrier—An Overview over Technology, Status, and Challenges in Germany”, J (2024), 7(4) 546-570.
6. THE, “Hydrogen Storage: Challenges, Solutions, Advanced Method”, The Hydrogen Energy (2025).
7. Muhammad Aziz, “Liquid Hydrogen: A Review on Liquefaction, Storage, Transportation, and Safety”, Energies (2021), 14(18) 5917.
8. SGS INSPIRE team, “Methanol: Properties and Uses”, INSPIRE (2020).
9. Wojciech Tutak & Arkadiusz Jamrozik, “Analysis of the Application of Ammonia as a Fuel for a Compression-Ignition Engine”, Energies (2025), 18(12), 3217.
10. UFine, “What Is the Energy Density of a Lithium-Ion Battery?”, UFine Blog (2024).
11. Monika Dulian & Gregor Erbarch, “Renewable and low-carbon hydrogen State of play and outlook”, European Parliament Research Service (2025).
12. Ulf Bossel & Baldur Eliasson, “Energy and the Hydrogen Economy”, U.S. Department of Energy AFDC (2003).
13. M. Gratzel, Nature 414(6861) p.338-344 (2001)
14. Paula Quitério, J. Phys. Chem. C p.12865-13508 (2020)
15. Sofia Gonçalves, Applied Materials and Interfaces, p.64389-65740 (2024)
16. A. Apolinário, Journal of Materials Chemistry A, p.9067-9078 (2014)
17. Mathieu S. Prévot, Kevin Sivula*, Phys. Chem. C p.17879–17893 (2013)
18. Yubin Chen, Xiaoyang Feng, Ya Liu, Xiangjiu Guan, Clemens Burda*****, Liejin Guo***,** ACS Energy Letters 5(3), 844-866 (2020)
19. International Renewable Energy Agency. “Hydrogen.” *IRENA*, www.irena.org/Energy-Transition/Technology/Hydrogen.
20. Erbach, Gregor, and Sara Svensson. “EU Rules for Renewable Hydrogen: Delegated Regulations on a Methodology for Renewable Fuels of Non-Biological Origin”. European Parliamentary Research Service, (2023).
21. Hydrogen Production Pathways | Department of Energy

22. M.H. Sawal, A.A. Jalil, N.F. Khusnun, N.S. Hassan, M.B. Bahari, “A review of recent modification strategies of TiO2-based photoanodes for efficient photoelectrochemical water splitting performance" Vol. 467, (2023)
23. João Azevedo, “Solar Photoelectrochemical Energy Storage: Materials and Devices”, (2016)
24. Nguyen Hoang Lam, Nguyen Tam Nguyen Truong, Kwang-Soon Ahn, Younjung Jo, Seung Beom Kang, Nguyen Huu Hieu, Shoyebmohamad F. Shaikh, Chang-Duk Kim, Moonyong Lee, Jae Hak Jung, “CuO photocathode enhancement through ultra-thin carbon coating layer for photoelectrochemical water splitting”, FlatChem, Volume 23, (2024)
25. Linh Trinh, Krzysztof Bienkowski, Aleksandra Parzuch, Piotr Wróbel, Grzegorz Kaproń, Marcin Pisarek, Renata Solarska,“Hofmann-type MOF-derived CuNiOx photocathode for effective PEC H2 production”, International Journal of Hydrogen Energy, Volume 87, 2024, Pages 1171-1179,
26. Jianming Li, Xu Jin, Rengui Li, Yue Zhao, Xiaoqi Wang, Xiaodan Liu, Hang Jiao, “Copper oxide nanowires for efficient photoelectrochemical water splitting”, Applied Catalysis B: Environmental, Volume 240, 2019, Pages 1-8, ISSN 0926-3373
27. Gawlińska-Nęcek K, Socha RP, Starowicz Z, Major Ł, Panek P. Ambient Stability of Sodium-Doped Copper Oxide Obtained through Thermal Oxidation. *Materials*. 2024; 17(19):4823. https://doi.org/10.3390/ma17194823
28. João Freitas, “Nanostructured Oxide, “Semiconductors for Photoelectrochemical Cells”, (2022)
29. C. Hu, *Modern Semiconductor Devices for Integrated Circuits*, Upper Saddle River, NJ: Prentice Hall, 2010.
30. Kumar, M., Meena, B., Subramanyam, P. *et al.* Recent trends in photoelectrochemical water splitting: the role of cocatalysts. *NPG Asia Mater* **14**, 88 (2022). https://doi.org/10.1038/s41427-022-00436-x
31. Pengliang Chen, Bokai Kang, Pengcheng Liu, Xingxing Cheng, Shiming Zhong, Xuetao Wang, Baizeng Fang, “Passivation strategies for enhanced photoelectrochemical water splitting”, Journal of Power Sources, Volume 628, (2025)
32. Meena B, Kumar M, Kumar A, Sinha GN, Nagumothu R, Subramanyam P, Suryakala D, Subrahmanyam C. Integrated p-n Junctions for Efficient Solar Water Splitting upon TiO_2/CdS/$BiSbS_3$ Ternary Hybrids for Improved Hydrogen Evolution and Mechanistic Insights. *Catalysts*. 2022
33. Paracchino, Adriana & Brauer, Jan & Moser, Jacques-E & Thimsen, Elijah & Graetzel, Michael. (2012). Synthesis and Characterization of High-Photoactivity

Electrodeposited Cu2O Solar Absorber by Photoelectrochemistry and Ultrafast Spectroscopy. Journal of Physical Chemistry C. 116. 7341-7350. 10.1021/jp301176y.

34. Zhang H, Liu J, Xu T, Ji W, Zong X. Recent Advances on Small Band Gap Semiconductor Materials (≤2.1 eV) for Solar Water Splitting. *Catalysts*. 2023
35. Zainab Najaf, Dang Le Tri Nguyen, Sang Youn Chae, Oh-Shim Joo, Anwar Ul Haq Ali Shah, Dai-Viet N. Vo, Van-Huy Nguyen, Quyet Van Le, Gul Rahman, Recent trends in development of hematite (α-Fe2O3) as an efficient photoanode for enhancement of photoelectrochemical hydrogen production by solar water splitting, International Journal of Hydrogen Energy, Volume 46, Issue 45, 2021, Pages 23334-23357
36. BiVO4-Based Photoelectrochemical Water Splitting - Yi - 2025 - ChemElectroChem - Wiley Online Library
37. Liu C, Zhang C, Yin G, Zhang T, Wang W, Ou G, Jin H, Chen Z. A Three-Dimensional Branched TiO_2 Photoanode with an Ultrathin Al_2O_3 Passivation Layer and a NiOOH Cocatalyst toward Photoelectrochemical Water Oxidation. ACS Appl Mater Interfaces. 2021 Mar 24;13(11):13301-13310. doi: 10.1021/acsami.1c00948. Epub 2021 Mar 16. PMID: 33723983.
38. Zhongyong Jiang, Huimin Geng, Xiaoyan Cai, Liang Mao, Yulong Zhao, Xiuquan Gu, Preparation of CuBi2O4 photocathodes for overall water splitting under visible light irradiation, Materials Science in Semiconductor Processing, Volume 134, 2021, 105989, ISSN 1369-8001
39. Tsege, E.L., Cho, S.K., Tufa, L.T. *et al.* Scalable and inexpensive strategy to fabricate CuO/ZnO nanowire heterojunction for efficient photoinduced water splitting. *J Mater Sci* **53**, 2725–2734 (2018).
40. R. SiavashMoakhar, S. M. Hosseini-Hosseinabad, S. Masudy-Panah, A. Seza, M. Jalali, H. Fallah-Arani, F. Dabir, S. Gholipour, Y. Abdi, M. Bagheri-Hariri, N. Riahi-Noori, Y.-F. Lim, A. Hagfeldt, M. Saliba, Photoelectrochemical Water-Splitting Using CuO-Based Electrodes for Hydrogen Production: A Review. *Adv. Mater.* 2021, 33, 2007285
41. Huasen Lu, Shixu Song, Qisen Jia, Guangbo Liu, Luhua Jiang, Advances in Cu2O-based Photocathodes for Photoelectrochemical Water Splitting, Acta Physico-Chimica Sinica, Volume 40, Issue 2, 2024, 2304035
42. Lim, Jaekeun, et al. “All-Perovskite Tandem Solar Cells: From Fundamentals to Technological Progress.” *Energy & Environmental Science*, vol. 17, 2024, pp. 4390–4425

43. Byrnes, Steve. *The Shockley–Queisser Limit*. 2012
44. Richard E. Rocheleau, Eric L. Miller, Photoelectrochemical production of hydrogen: Engineering loss analysis, International Journal of Hydrogen Energy, Volume 22, Issue 8
45. Sun, F., Zhang, C., Li, D., You, F., Liang, C. and Wang, Y. (2025), Tabulated Values of the Shockley–Queisser Limit for Tandem Solar Cells. Phys. Status Solidi A, 222: 2400524
46. Sam Keene, Rohini Bala Chandran and Shane Ardo,Calculations of theoretical efficiencies for electrochemically-mediated tandem solar water splitting as a function of bandgap energies and redox shuttle potential, Energy Environ. Sci., 2019, 12, 261-27
47. Green, M. A. (2003). *Third Generation Photovoltaics: Advanced Solar Energy*. Springer Series in Photonics, Vol. 12. Springer Spektrum
48. Sharir-Smith, J. (2024). *The Shockley-Queisser Limit and Tandem Solar Cells*. Stanford University. Retrieved from
49. *J. Mater. Chem. A*, 2021,9, 14085-14092
50. Zichen Gong, Bin Liu, Peng Zhang, Shujie Wang, Shaokun Jiang, Tuo Wang, and Jinlong Gong, *ACS Materials Letters* **2021** *3* (7), 939-946
51. Chakthranont, Pongkarn (55356746900); Hellstern, Thomas R. (55022863000); McEnaney, Joshua M. (56338424200); Jaramillo, Thomas F. (6603398169), 55356746900; 55022863000; 56338424200; 6603398169, Design and Fabrication of a Precious Metal-Free Tandem Core–Shell p+n Si/W-Doped BiVO4 Photoanode for Unassisted Water Splitting, (2017) Advanced Energy Materials, 7 (22)
52. Dingwang Huang, Kang Wang, Le Yu, Thi Hiep Nguyen, Shigeru Ikeda, and Feng Jiang, *ACS Energy Letters* **2018** *3* (8), 1875-1881
53. Shuaipeng Wang, Kang Wan, Jiayue Feng, Yilong Yang, Songcan Wang, BiVO4 photoanodes with enhanced photoelectrochemical performance: Preparation, modification and emerging applications, Journal of Materials Science & Technology, Volume 217, 2025, Pages 182-220
54. Liu B., Feng S., Yang L., Li C., Luo Z., Wang T., Gong J., AUTHOR FULL NAMES: Liu, Bin; Feng, Shijia; Yang, Lifei; Li, Chengcheng ; Luo, Zhibin; Wang, Tuo ;Gong, Jinlong, Bifacial passivation of: N -silicon metal-insulator-semiconductor photoelectrodes for efficient oxygen and hydrogen evolution reactions (2020) Energy and Environmental Science, 13 (1), pp. 221 - 228
55. Energy Environ. Sci., 2021,14, 1480-1489

56. Fareza A.R., Nugroho F.A.A., Abdi F.F., Fauzia V., AUTHOR FULL NAMES: Fareza, Ananta R. (57224195480); Nugroho, Ferry Anggoro Ardy (56641546600); Abdi, Fatwa F. (55204686600); Fauzia, Vivi (36570282000), 57224195480; 56641546600; 55204686600; 36570282000, Nanoscale metal oxides-2D materials heterostructures for photoelectrochemical water splitting—a review, (2022) Journal of Materials Chemistry A, 10 (16), pp. 8656 - 8686, Cited 95 times.
57. H. Cai, W. Zhao, G. Xiao, Y. Hu, X. Wu, H. Ni, S. Ikeda, Y. Ng, J. Tao, L. Zhao, F. Jiang, Process Accumulated 8% Efficient Cu_2ZnSnS_4-$BiVO_4$ Tandem Cell for Solar Hydrogen Evolution with the Dynamic Balance of Solar Energy Storage and Conversion. *Adv. Sci.* 2023, 10, 2205726.
58. Yubin Chen, Xiaoyang Feng, Ya Liu, Xiangjiu Guan, Clemens Burda, and Liejin Guo, *ACS Energy Letters* **2020** *5* (3), 844-866
59. Yanhong Lyu, Yang Zhou, Jianyun Zheng, Unbiased photoelectrochemical tandem configuration for water splitting, Journal of Power Sources, Volume 641, 2025, 236917,
60. Himanshi Goel, Riya Nagpal, Kumar Rakesh Ranjan, Vivek Mishra, Recent challenges and scope in tandem cells for unassisted overall water splitting, Next Materials, Volume 8, 2025, 100560,
61. Calos, N. J. Forrester, J. S. Schaffer, G. B., Journal of Solid State Chemistry, **122** (1996)
62. Swanson, H E Tatge, E, National Bureau of Standards (U.S.), Circular, **359** (1953)
63. Stefanie E. Bogenrieder, Julian Beßner, Albert K. Engstfeld, and Timo Jacob, *The Journal of Physical Chemistry C* **2024** *128* (23), 9693-9704
64. Kirfel, A. Eichhorn, K., Acta Crystallographica, Section A, **46** (1990)
65. Sumita Choudhary, J. V. N. Sarma, Surojit Pande, Soraya Ababou-Girard, Pascal Turban, Bruno Lepine, Subhashis Gangopadhyay; Oxidation mechanism of thin Cu films: A gateway towards the formation of single oxide phase. *AIP Advances* 1 May 2018; 8 (5): 055114
66. Shang, Shengyan & Kunwar, Anil & Wang, Yanfeng & Yao, Jinye & Ma, Haitao & Wang, Yunpeng. (2018). Influence of Cu nanoparticles on Cu 6 Sn 5 growth behavior at the interface of Sn/Cu solder joints. 10.1109/ICEPT.2018.8480619.
67. Sayyed, S. G., Shaikh, A. V., Shinde, U. P., Hiremath, P., & Naik, N. (2023). *Copper oxide-based high-performance symmetric flexible supercapacitor: potentiodynamic deposition*. *Journal of Materials Science: Materials in Electronics, 34*, Article 1361.
68. R. SiavashMoakhar, S. M. Hosseini-Hosseinabad, S. Masudy-Panah, A. Seza, M. Jalali, H. Fallah-Arani, F. Dabir, S. Gholipour, Y. Abdi, M. Bagheri-Hariri, N. Riahi-

Noori, Y.-F. Lim, A. Hagfeldt, M. Saliba, Photoelectrochemical Water-Splitting Using CuO-Based Electrodes for Hydrogen Production: A Review. *Adv. Mater.* 2021, 33, 2007285

69. Takumi Ikenoue *et al* 2019 *Appl. Phys. Express* **12** 055509
70. Ravichandiran, C. & Sakthivelu, A. & Davidprabu, R. & Valanarasu, S. & Adaikalam, Kathalingam & Ganesh, V. & Shkir, Mohd & C.J., Sreelatha & Alfaify, Sa. (2018). Effect of deposition temperature on key optoelectronic properties of electrodeposited cuprous oxide thin films. Optical and Quantum Electronics. 50. 10.1007/s11082-018-1531-z.
71. Michael Nolan, Simon D. Elliott, Tuning the electronic structure of the transparent conducting oxide Cu2O, Thin Solid Films, Volume 516, Issue 7, 2008, Pages 1468-1472
72. Kumar, M., & Rathi, R. (2015). *Synthesis and characterization of CuO nanoparticles for optoelectronic applications*. International Journal of Nanotechnology and Nanoscience, 6(1)
73. Ahmad, F. (2016). *First principle calculation of electronic, optical properties and photocatalytic potential of CuO surfaces*
74. Byrnes, Steve. “The Shockley–Queisser Limit”. 16 Oct. 2012
75. Rühle, S. (2016). “Tabulated values of the Shockley–Queisser limit for single junction solar cells.” Solar Energy, 130, 139–147.
76. “Radiative Efficiency Limit: The SQ Limit Explained.” *Ossila*, accessed in 2025.
77. Ramos, A. R., Tapia, A. K. G., Piñol, C. M. N., Lantican, N. B., del Mundo, M. L. F., Manalo, R. D., & Herrera, M. U. (2019). Effects of reaction temperatures and reactant concentrations on the antimicrobial characteristics of copper precipitates synthesized using L-ascorbic acid as reducing agent. *Journal of Science: Advanced Materials and Devices, 4*(1), 66–71
78. Thery, V., Boulle, A., Crunteanu, A., Orlianges, J. C., Beaumont, A., Mayet, R., Mennai, A., Cosset, F., Bessaudou, A., & Fabert, M. (2016). Role of thermal strain in the metal-insulator and structural phase transition of epitaxial VO_2 films. *Physical Review B, 93*(18), 184106.
79. University of Washington. (n.d.). *Propagation of Errors—Basic Rules*.
80. Ünaleroğlu, C., Mert, Y., & Zümreoğlu-Karan, B. (2001). Synthesis and characterization of copper ascorbate. *Synthesis and Reactivity in Inorganic and Metal-Organic Chemistry*, *31*(9), 1531–1543.
81. HORIBA Scientific. (n.d.). *Specty Workbench: Stress, Strain and Raman Spectroscopy*. Retrieved from

82. Ries, M., & Heisinger, F. (2024). *Using Raman spectroscopy to determine the strain in semiconductor samples* [Application note]. Thermo Fisher Scientific.
83. Tuschel, D. (2017). *Why are the Raman spectra of crystalline and amorphous solids different?* Spectroscopy, 32(3), 26–33
84. An Overview of Magnetron Sputtering | Stanford Advanced Materials
85. Magnetron sputtering - ScienceDirect
86. Saidin, N. U., Ying, K. K., & Khuan, N. I. (n.d.). *Electrodeposition: Principles, Applications and Methods*. Industrial Technology Division, Malaysian Nuclear Agency.
87. Gonçalves, S., Andrade, V., Sousa, C. T., Araújo, J. P., Belo, J. H., & Apolinário, A. (2023). Tunable iron–cobalt thin films grown by electrodeposition. *Magnetochemistry*, 9(7), 161
88. Elgrishi, N., Rountree, K. J., McCarthy, B. D., Rountree, E. S., Eisenhart, T. T., & Dempsey, J. L. (2018). A practical beginner's guide to cyclic voltammetry. *Journal of Chemical Education*, 95(2), 197–206.
89. Patrycja Makuła, Michał Pacia, and Wojciech Macyk. How to correctly determine the band gap energy of modified semiconductor photocatalysts based on uv–vis spectra.The Journal of Physical Chemistry Letters, 9(23):6814–6817, 2018.
90. Deng, Y., Handoko, A. D., Du, Y., Xi, S., & Yeo, B. S. (2016). In situ Raman spectroscopy of copper and copper oxide surfaces during electrochemical oxygen evolution reaction: Identification of CuIII oxides as catalytically active species. *ACS Catalysis*, 6(4), 2473–2481.
91. Zoolfakar, A. S., Abdul Rani, R., Morfa, A. J., O'Mullane, A. P., & Kalantar-zadeh, K. (2014). Nanostructured copper oxide semiconductors: A perspective on materials, synthesis methods and applications. *Journal of Materials Chemistry C*, 2(27), 5247–5270
92. Valvo, M., Thyr, J., & Edvinsson, T. (2023). Defect-induced Raman scattering in Cu_2O nanostructures and their photocatalytic performance. *ChemElectroChem*, 10(22), e202300376.
93. Oxford Instruments. (2025). *Ion Beam Deposition (IBD)*.
94. Mokobi, F. (2024). *Scanning Electron Microscope (SEM): Principle, Parts, Uses*. Microbe Notes.
95. CEMUP – Centro de Materiais da Universidade do Porto. (n.d.). *Materials Centre of the University of Porto*.
96. Thermo Fisher Scientific. (2025). *Electrons in SEM*.

97. Nanakoudis, A. (2019). *EDX analysis with SEM: How does it work?* Thermo Fisher Scientific.
98. Gonçalves, S. M. (2021). *Customization of thermal expansion in nanowires* [Master's thesis, Faculdade de Ciências da Universidade do Porto]. Repositório Aberto da Universidade do Porto.
99. Trinity College Dublin. (2023, January 12). *Integrating Sphere – Civil Structural & Environmental Engineering*.
100. Couto, J. R. (2025). *Flexible photoanodes based on hematite nanoparticles paste for solar water splitting* [Master's thesis, University of Porto]. Repositório Aberto da Universidade do Porto.
101. Freitas, J. P. F. (2022). *Nanostructured oxide semiconductors for photoelectrochemical cells* [Master's thesis, University of Porto, Faculty of Sciences].
102. Dias, P., Schreier, M., Tilley, S. D., Luo, J., Azevedo, J., Andrade, L., Bi, D., Hagfeldt, A., Mendes, A., Grätzel, M., & Mayer, M. T. (2015). *Transparent cuprous oxide photocathode enabling a stacked tandem cell for unbiased water splitting*. Advanced Energy Materials, 5(24), 1501537.
103. Yuce, A. (2023, July 29). *A novel technique for Raman spectroscopy of live proteins*. Astrafizik.
104. Crystallography Open Database. (n.d.). *Open-access collection of crystal structures*. Retrieved September 24, 2025, from http://crystallography.net/cod/
105. PlasmaSolaris Ltd. (2020, April 22). *Shockley–Queisser Limit: Theoretical efficiency of single-junction solar cells*.
106. Newman, M. E. J. (2012). *Computational physics*. CreateSpace Independent Publishing Platform.
107. Sarfraz, B., Bashir, I., & Rauf, A. (2023). CuS/NiFe-LDH/NF as a bifunctional electrocatalyst for hydrogen evolution (HER) and oxygen evolution reactions (OER). *Fuel, 337*, 127253.
108. National Renewable Energy Laboratory. (2025). *Reference Air Mass 1.5 Spectra*. U.S. Department of Energy.
109. United Nations. (n.d.). *1.5°C: What it means and why it matters*. United Nations Climate Action.
110. Our World in Data. (2025). *Annual temperature anomalies relative to the pre-industrial period*
111. Nanoscale Horiz.,2016,1,243-267

112. Edvinsson, T. (2018). Optical quantum confinement and photocatalytic properties in two-, one- and zero-dimensional nanostructures. *Royal Society Open Science*, *5*(9), 180387

113. Ahmad, F., Agusta, M. K., & Dipojono, H. K. (2016). Electronic and optical properties of CuO based on DFT+U and GW approximation. *Journal of Physics: Conference Series*, *739*(1), 012040.

114. LibreTexts. (n.d.). *Chemistry LibreTexts*.

115. Li, J., Jin, X., Li, R., Zhao, Y., Wang, X., Liu, X., & Jiao, H. (2019). Copper oxide nanowires for efficient photoelectrochemical water splitting. *Applied Catalysis B: Environmental, 240*, 1–8.

116. Trinh, L., Bienkowski, K., Parzuch, A., Wróbel, P., Kaproń, G., Pisarek, M., & Solarska, R. (2024). Hofmann-type MOF-derived CuNiOx photocathode for effective PEC H_2 production. *International Journal of Hydrogen Energy, 87*, 1171–1179.

117. Pourbaix, M. (1974). *Atlas of electrochemical equilibria in aqueous solutions* (p. 196). Pergamon Press

118. Lee, J. M., & Ko, J. S. (2017). Formation of microstructure by copper-cuprous co-electrodeposition using stirring and boric acid addition. *International Journal of Precision Engineering and Manufacturing, 18*(6), 871–877.Attachments [if applicable]

119. Corn, R. (2019). *Fick's Laws of Diffusion and Electrochemistry*. Chem 243 Lecture Notes, University of California, Irvine. Retrieved from https://www.chem.uci.edu/~unicorn/243/papers/FicksLaws2019.pdf

A – Supplementary Information of Chapter 2

Trapezoidal Rule

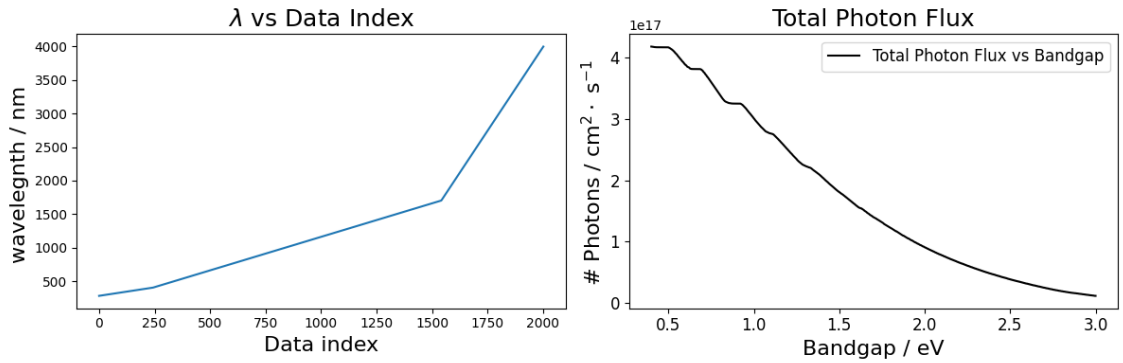
Trapezoidal rule can be elegantly implemented in python with NumPy module. The 1 Sun AM 1.5 is acquired from [] and is already discrete, so 4 new arrays are created with this data:

- Arrays E_1, f_1: containing the values for $E, f(E)$ from the 1st element up until the penultimate position, included.
- Arrays E_2, f_2: containing the values for $E, f(E)$ from the 2nd element up until the last.

By calculating "$E_2 - E_1$", we get the distance between successive photon energies of the spectrum: we get an array with the widths h of each trapezoidal – which in this case is very relevant, because the distance between successive wavelengths in 1 Sun AM 1.5 series is not homogeneous, its different for UV, VIS and IR radiation. And now, f_1 is the left height of the various trapezoids and f_2 is the right height. The rule is implemented by calculating the operation:

$$I \approx \sum \frac{(E_2 - E_1) \cdot (f_1 + f_2)}{2}$$

Wich can be quickly done by the operation "np.sum($\frac{A \cdot B}{2}$)", where $A = (E_2 - E_1)$ and $B = (f_1 + f_2)$. For finding $Solar_c$, all spectrum is integrated. To find G, the spectrum is integrated between the respective limits, according to eq. 7.



Wavelength vs data index, the different wavelength slopes indicate different distances between successive wavelengths. Right: Total photon flux passing through the junction as a function of E_{gap}. Comparison literature: [].

Solar constant

Model	Calculated / W	Official / W	Source
This work	1000.37	1000	-
Literature	1003.02		[43]

Summary results for trapezoidal function and comparison with literature calculations.

```
def trapezio(x, y, egap):

    arg = np.where(x >= egap)[0]
    xx = x[arg]
    yy = y[arg]

    w = xx[1:] - xx[:-1]  # E2-E1

    fx = yy[1:] + yy[:-1]  # f1 + f2

    return np.sum(w * fx) / 2
```

Trapezoidal integration implemented code.

Gauss Legendre Quadrature

The weights and sample points are obtained through NumPy module through "polynomial.legendre.leggauss()" function. Firstly, a $dQ_c(z, E_g, T)$ function that calculates the integrand of eq _ is implemented. Then, a Gauss-Legendre function $Gauss_L(dfunc, E_g, T, N)$ that calls the function dQ_c if $dfunc = dQ_c$ and integrates it using approximation of eq. __ for $z \epsilon [-1,1]$ for a given E_g at temperature T, using N sample points is implemented. For evaluating the number of sample points need, this integration is performed for various E_g values varying the number of sample points N and evaluating the convergence rates by the formula $\Delta E = \frac{I_n - I_{n-1}}{I_{n-1}} \times 100$, where I_n is the numerical integral value with n sample points.

```
def dQc(z,Eg,T):

    C = 16*pi / (c**2 * h**3)
    dz = (1-z)**-4
    v = VT(T)

    return C *dz* Eg**3 / (np.exp(2*Eg/(v*(1-z)))-1)
```

Integrand function implementation.

```
def Gauss_L(dfunc,Eg,T,N):
    xi,wi = np.polynomial.legendre.leggauss(N)

    return np.sum( wi * dfunc(xi,Eg,T))
```

Gauss-Legendre quadrature implementation.

Single absorber functions and S-Q limit implementation

```
def VT(T):
    return k*T

def J(G,Qc,V,T,fc):
    v = VT(T)
    return q*(G-Qc*np.exp(V/v)/fc)

def V_oc(G,Qc,T,fc):

    v = VT(T)
    return v*np.log(fc*G/Qc)
```

Implement functions to calculate $J_{photo} - V$ relations.

```
def S_Q(Egap,T,N,ev,p_flux,delta,fc):
    n = len(Egap)
    sq = np.zeros(n,dtype=float)
    v = VT(T)

    for i in np.arange(n):
        Eg = Egap[i]

        G = trapezio(ev,p_flux,Eg)
        Qc = Gauss_L(dQc,Eg,T,N)

        Voc = V_oc(G,Qc,T,fc)

        v_range = np.arange(0,Voc +delta,delta)
        Js = J(G,Qc,v_range,T,fc)*10**-1                    # mA/cm^2

        power = Js*v_range
        if np.size(power)==0:
            power = np.zeros(1)

        arg = np.argmax(power)

        mpowr = power[arg]

        sq[i] = mpowr
    return sq
```

S-Q limit calculation implementation.

Model	PCE@1.1eV	J_{SC} @ 1.1 eV	V_{OC} @1.1 eV	Max PCE	$E_{gap,max}$	Source
This work	32.9%	44.2282	0.857751	33.7%	1.34	-
Literature	32.8%	44.2239	0.857749	33.7%	1.34	[74][76]

Results comparison with literature.

```
def QE(x,Eg,A,b):
    ab = A * np.tanh(b*(x-Eg))
    ab = np.where(x<Eg,0,ab)
    return ab
```

Quantum Efficiency function implementation.

```
def S_Q2(Egap,T,N,ev,p_flux,delta,fc,A,b):
    n = len(Egap)
    sq = np.zeros(n,dtype=float)
    v = VT(T)

    for i in np.arange(n):
        Eg = Egap[i]
        ap = QE(ev,Eg,A,b)
        p = ap*p_flux
        G = trapezio(ev,p,Eg)
        Qc = Gauss_L(dQc,Eg,T,N)

        Voc = V_oc(G,Qc,T,fc)

        v_range = np.arange(0,Voc +delta,delta)
        Js = J(G,Qc,v_range,T,fc)*10**-1                # mA/cm^2

        power = Js*v_range

        if np.size(power)==0:
            power = np.zeros(1)

        arg = np.argmax(power)

        mpowr = power[arg]

        sq[i] = mpowr
    return sq
```

Adapted model implementation in python for single junction devices.

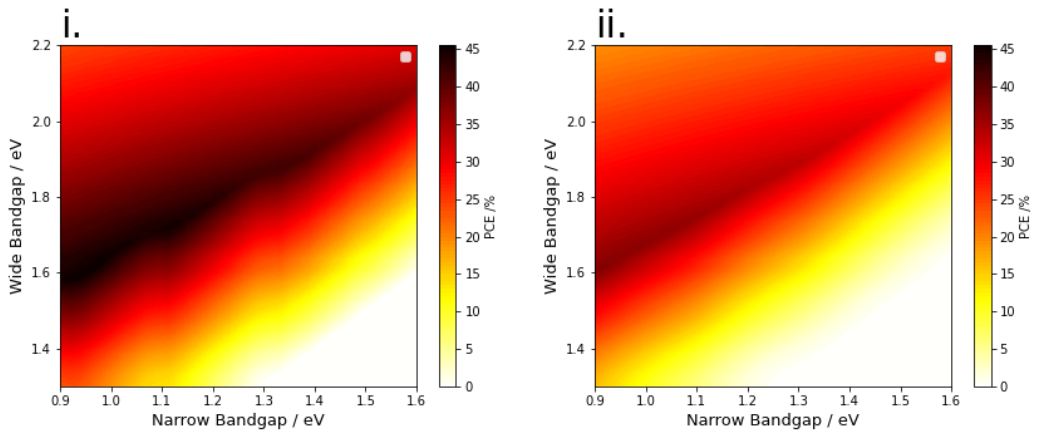
Tandem Cells Implementation

For modelling 2T tandem cells, firstly two arrays containing the bandgap values of each of the junctions are created: E_{g1}, E_{g2}, with a user defined distance δ between successive elements. Two meshgrid arrays are created from E_{g1} and E_{g2}, that contain all possible combinations of both junctions' bandgaps. Then, the same method for calculation of the

S-Q limit described in section 2.3.1 is employed for each semiconductor, with the following nuances:

1. G_1 and G_2 are given calculated using eq. 2.8 and 2.10 using trapezoidal rule, but by simply making $\phi(E) = 0$ for $E > E_{g1}$. In case of 3 junctions' cell, the same reasoning is applied making spectral photon flux 0 for $E > E_{g2}$.
2. Both $J_{SC,1}$ and $J_{SC,2}$ are calculated, and the minimum $J_{SC,min}$ is retained. After this, an array J_{photo} like in eq. 2.11 is created – With the allowed current densities for the system. The same reasoning for 2T 3 junction cells.
3. After step 2, each cell voltage relation is calculated using relations 2.12 and 2.13. The converted power is given by: $Power = J_{photo} \cdot [V_1(J_{photo}) + V_2(J_{photo})]$. Including the $V_3(J_{photo})$ as well in the case o 2T multijunction.
4. After knowing the power distribution for a given bandgap pairing, the MPP is determined using the method described in section 2.2.3. The calculation is performed for a given interval of bandgaps for each junction, for each maximum energy conversion is determined by the method described in section 2.2.3.

Results for 2 junction photovoltaic cell in series:



S-Q limit for a 2T tandem cell. ii. S-Q limit considering $A = 1$, $B = 5$, $f_c = 10^{-2}$ with the adjusted model.

Maximum PCE drops from 45.54% to 37.82% considering different losses factors $A = 1$, $B = 5$, $f_c = 10^{-2}$, but the bandgap pairing doesn't change much. Uncertainty on bandgap is of order $\sim 10^{-2}$.

	$E_{g,1}$ / eV	$E_{g,2}$ / eV	Max PCE / %
i.	1.59 ± 0.01	0.94 ± 0.01	45.54
ii.	1.61 ± 0.01	0.91 ± 0.01	37.82

Bandgap pairings and respective maximum PCE obtained from the implemented model.

```python
def PECl_2T(ev,s_flux,e1,e2,T,N,fc,A,B,delta):
    Eg1,Eg2 = np.meshgrid(e1,e2)
    n1,n2 = len(e1), len(e2)
    PCE = np.zeros((n2,n1))
    JJ = np.zeros((n2,n1))
    VV = np.zeros((n2,n1))
    f1 = s_flux

    for i in np.arange(n2):
        for j in np.arange(n1):

            e1 = Eg1[i,j]
            e2 = Eg2[i,j]

            p2 = np.where(ev <= e1,f1,0)*QE(ev,e2,A,B)

            G1 = trapezio(ev,f1*QE(ev,e1,A,B),e1)
            G2 = trapezio(ev,p2,e2)
            Qc1 = Gauss_L(dQc,e1,T,N)
            Qc2 = Gauss_L(dQc,e2,T,N)

            Js1 = J(G1,Qc1,0,T,fc)
            Js2 = J(G2,Qc2,0,T,fc)

            Jsc = np.min((Js1,Js2))

            Js = np.arange(0,Jsc,delta)
            V1 = volt(Jsc,Js,Qc1)
            V2 = volt(Jsc,Js,Qc2)

            Power = (V1+V2) * Js


            if np.any(Power):
                mpp = np.argmax(Power)

                JJ[i,j] = Js[mpp]
                VV[i,j] = V1[mpp] + V2[mpp]

                PCE[i,j] = Power[mpp] / 10


            else:

                PCE[i,j] = 0
    return Eg1,Eg2,PCE,JJ,VV
```

2 junctions in series adapted model implementation. For S-Q the QE function simply isn't called and $f_c = 1$.

Function "PECl_2T()" outputs JJ and VV at MPP, STH is calculated posteriorly.

```
Gibs = 237.2     # J/mol
Na = 6.023*10**23

phi = J / (2*q*Na)                              # H2 molecules / s.m^2

STH = phi * Gibs * 100                            # x 100 / 1 kW.m^-2

STH1 = np.where(E1+E2>=3.23,STH,0)
STH2 = np.where(V>=2,STH,0)
```

Unbiased STH calculation for both losses consideration in figure 2.7.

```
STH3 = ( Jss / (2*q*Na) ) * Gibs * 100

STH5 = ( JS / (2*q*Na) ) * Gibs * 100

STH4 = ( J_S / (2*q*Na) ) * Gibs * 100

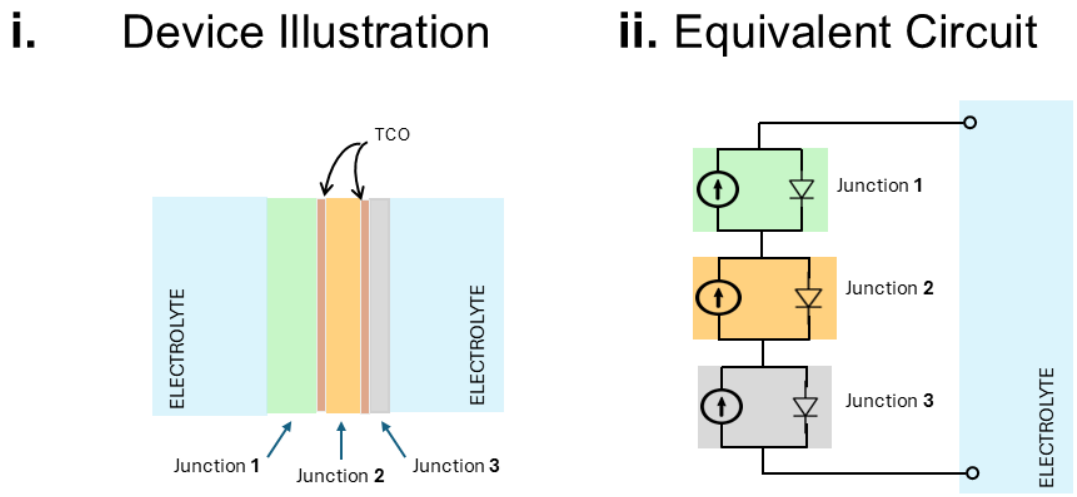
STH1 = np.where(V1 >=2, STH1, J1*10**-1*(1.23-(2-V1)))

STH2 = np.where(V2 >=2, STH2, J2*10**-1*(1.23-(2-V2)))

STH3 = np.where(Vss>=2, STH3, J3 *(1.23-(2-V3)))
```

STH implementation for both biased and unbiased regions of figure 2.8.

3 junctions' devices



Device configuration and equivalent circuit for results in figure 2.10.

```
def PEC_3T(ev,s_flux,e1,e2,e3,T,N,delta):

    Eg1,Eg2 = np.meshgrid(e1,e2)
    n1,n2 = len(e1), len(e2)
    PCE = np.zeros((n2,n1))
    JJ = np.zeros((n2,n1))
    VV = np.zeros((n2,n1))
    f1 = s_flux

    for i in np.arange(n2):
        for j in np.arange(n1):

            e1 = Eg1[i,j]
            e2 = Eg2[i,j]

            p2 = np.where(ev <= e1,f1,0)          #incident spectr
            p3 = np.where(ev <= e2,f1,0)

            G1 = trapezio(ev,f1,e1)
            G2 = trapezio(ev,p2,e2)
            G3 = trapezio(ev,p3,e3)

            Qc1 = Gauss_L(dQc,e1,T,N)
            Qc2 = Gauss_L(dQc,e2,T,N)
            Qc3 = Gauss_L(dQc,e3,T,N)

            Js1 = G1 - Qc1
            Js2 = G2 - Qc2
            Js3 = G3 - Qc3

            Jsc = q * np.min((Js1,Js2,Js3))

            Js = np.arange(0,Jsc,delta)

            V1 = volt(Jsc,Js,Qc1)
            V2 = volt(Jsc,Js,Qc2)
            V3 = volt(Jsc,Js,Qc3)

            Power = (V1+V2+V3) * Js


            if np.any(Power):
                mpp = np.argmax(Power)

                JJ[i,j] = Js[mpp]

    return Eg1,Eg2,JJ
```

Implemented code for 3 junctions in series STH calculation, relative to figure 2.10.

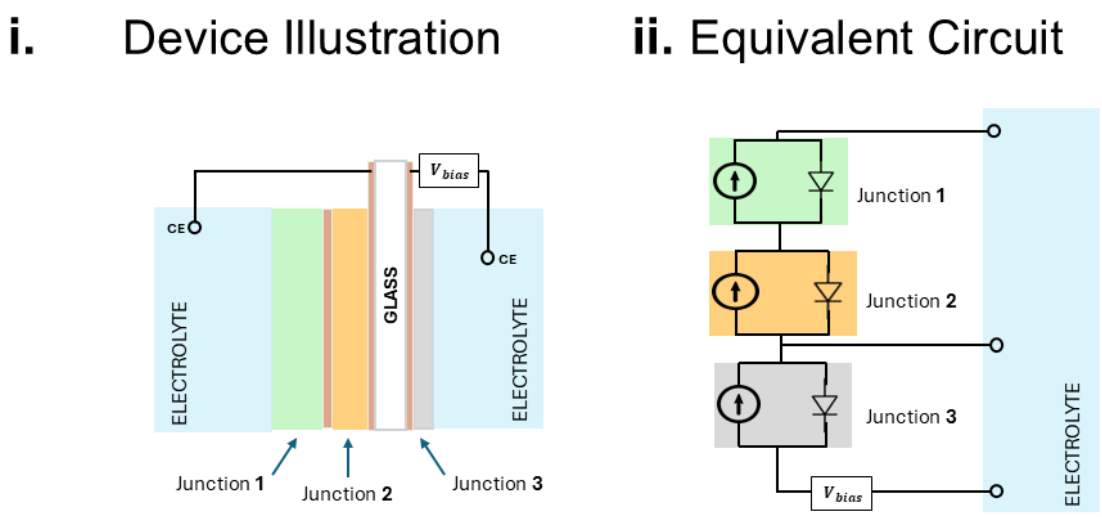
```
Gibs = 237.2
Na = 6.022*10**23
e3 = np.linspace(0.6,1.3,50)
Smax = np.zeros(50)
r2 = np.linspace(1.3,2,100)
r1 = np.linspace(1.4,3,100)
const = Gibs * 100 / (2*q*Na)

for i in np.arange(50): Smax[i] =
np.max(const*PEC_3T(ev,p_flux,r1,r2,e3[i],T,20,10**-3))

re_flux = np.zeros((n))
xe = np.where(ev<=1.3,ev,0)
p = np.where(ev<=1.3,p_flux,0)

  for i in range(n): re_flux[i] = trapezio(xe,p,e3[i])
```

Code for max STH(E_{g3}) calculation of figure 2.10.



Equivalent device and circuit for calculations results presented in figure 2.11.

```
def PEC_3TJ(ev,s_flux,e1,e2,e3,T,N,delta):

    Eg1,Eg2 = np.meshgrid(e1,e2)
    n1,n2 = len(e1), len(e2)
    JJ = np.zeros((n2,n1))
    JJ3 = np.zeros((n2,n1))
    VV = np.zeros((n2,n1))
    VV3 = np.zeros((n2,n1))
    f1 = s_flux
```

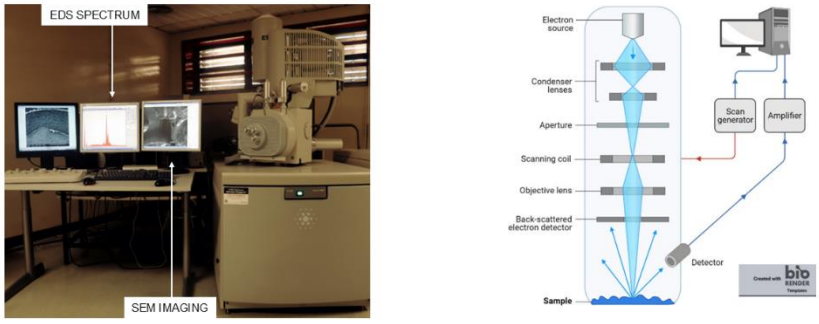
```
10
11      for i in np.arange(n2):
12          for j in np.arange(n1):
13
14              e1 = Eg1[i,j]
15              e2 = Eg2[i,j]
16
17              p2 = np.where(ev <= e1,f1,0)          #incident sp
18              p3 = np.where(ev <= e2,f1,0)
19
20              G1 = trapezio(ev,f1,e1)
21              G2 = trapezio(ev,p2,e2)
22              G3 = trapezio(ev,p3,e3)
23              Qc1 = Gauss_L(dQc,e1,T,N)
24              Qc2 = Gauss_L(dQc,e2,T,N)
25              Qc3 = Gauss_L(dQc,e3,T,N)
26
27              Js1 = G1 - Qc1
28              Js2 = G2 - Qc2
29              Js3 = q*(G3 - Qc3)
30
31              Jsc = q * np.min((Js1,Js2))
32
33              Js = np.arange(0,Jsc,delta)
34              J3 = np.arange(0,Js3,delta)
35
36              V1 = volt(Jsc,Js,Qc1)
37              V2 = volt(Jsc,Js,Qc2)
38              V3 = volt(Js3,J3,Qc3)
39
40              Power = (V1+V2) * Js
41              power2 = V3 * J3
42
43
44              if np.any(Power):
45                  mpp = np.argmax(Power)
46                  JJ[i,j] = Js[mpp]
47                  VV[i,j] = V1[mpp] + V2[mpp]
48
49
50              if np.any(power2):
51                  mpp2 = np.argmax(power2)
52                  JJ3[i,j] = J3[mpp2]
53                  VV3[i,j] = V3[mpp2]
54
55      return Eg1,Eg2,JJ,JJ3,VV,VV3
```

Implemented model for figure 2.11 calculations.

B – Supplementary Information of Chapter 3

Scanning Electron Microscopy.

i. ii.



i. SEM station at CEMUP. Adapted from [95]. Ii. SEM working principals and principal components. Adapated from [94].

A scanning electron microscope system uses a focused electron beam, controlled with electromagnetic lenses that scans the sample surface. Upon interaction, the beam induces emission of secondary electrons, backscattered electrons and diffracted backscattered electrons. Secondary and backscattered electrons are collected by a detector and are used to produce high resolution images: higher surfaces emit more secondary electrons that reach the detector, appearing brighter [96]. Backscattered electrons intensity is roughly proportional to the atomic number, allowing for atomic contrast imaging [96]. Also, when inner shell electrons are removed from the atoms, outer-shell electrons fill the state – emitting characteristic x-ray energy which can be measured and used to identify the atomic species present [97].

As the image is formed by detection of emitted electrons by the sample, high vacuum is required to ensure long mean free path of the electrons.

UV-VIS-NIR

$$E_g = \frac{a-b}{m} \qquad (3.11)$$

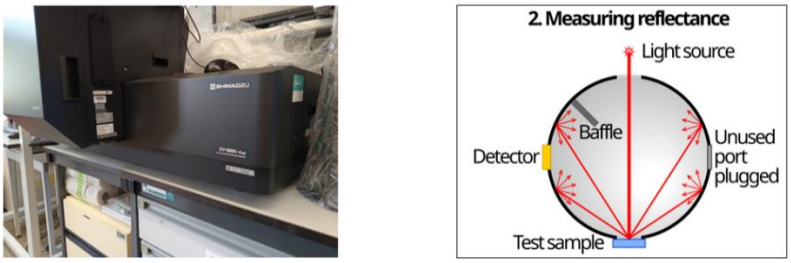
Bandgap uncertainty is calculated by error propagation formula [79], applied to expression 3.11:

$$\mu(E(m,b)) = \sqrt{\left(\frac{dE}{db}s_b\right)^2 + \left(\frac{dE}{dm}s_m\right)^2} \qquad (3.12)$$

$$\mu(E_g) = \sqrt{\left(\frac{s_b}{m}\right)^2 + \left(\frac{a-b}{m^2}s_m\right)^2} \qquad (3.13)$$

Where s_i is the uncertainty of variable i, considered to be the standard deviation for the linear regression's intercept and slope coefficients.

i. ii.



i. Photograph of the used UV-VIS-NIR system. ii. Illustration of integrating sphere working mechanism under: 1 – Transmittance measurements; 2 – Reflectance measurements. Adapted from [99].